Dusty Gust Fronts and Their Contributions to Long-Lived Convection in West Africa

by

Michael McGraw-Herdeg

S.B., Massachusetts Institute of Technology (2009)

Submitted to the Department of Electrical Engineering and Computer Science
in partial fulfillment of the requirements for the degree of

Master of Engineering in Electrical Engineering and Computer Science

at the

MASSACHUSETTS INSTITUTE OF TECHNOLOGY

June 2010

Author . . . .
Department of Electrical Engineering and Computer Science
May 21, 2010

Certified by . . . .
Earle R. Williams
Principal Research Engineer
Thesis Supervisor

Accepted by . . . .
Dr. Christopher J. Terman
Chairman, Department Committee on Graduate Theses

Dusty Gust Fronts and Their Contributions to Long-Lived Convection in West Africa

by

Michael McGraw-Herdeg

Submitted to the Department of Electrical Engineering and Computer Science
on May 21, 2010, in partial fulfillment of the
requirements for the degree of
Master of Engineering in Electrical Engineering and Computer Science

Abstract

To model and predict the behavior of West African storms and mesoscale convective systems (MCSs), we must understand the life cycle of gust fronts, which invariably accompany thunderstorms and often initiate them.

In this thesis, I track 40 gust fronts observed during summer 2006 by the MIT radar in Niamey, Niger and characterized with ground station measurements. A novel technique is developed using satellite infrared observations to track these fronts' propagation over a much longer distance than the <80 km enabled by radar; gust fronts are shown to propagate over >1000 km (mean 750 km) and up to 24 hours, much further than has been previously demonstrated for large numbers of gust fronts.

These gust fronts are often embedded in mesoscale convective systems (MCSs). It is shown how MCSs can be tracked in satellite imagery and lightning locations from a VLF intercontinental radio network are analyzed to yield valuable information about the long-range propagation of MCSs, including the most common kind of West African MCS — the westward-moving squall line. An automated method is developed to quantify lightning within an MCS (using a Lagrangian method to follow the storm).

Continuous "stripes" of lightning activity, caused by squall lines, emerge in lightning Hovmollers over West Africa and are substantially longer than the typical wavelength of an an African Easterly Wave (AEW). These stripes are used to study the relationships among MCS development, extent, and propagation distance: MCSs with greater squall line lengths propagate greater distances on average, but no evidence is found to show that larger, deeper systems propagate any faster than smaller systems, contrary to results in the literature. Evidence is shown that in many cases continuity within a lightning stripe is mediated by gust fronts. MCSs were found to propagate distances greater than an AEW wavelength, but only in the absence of an AEW; it is shown that AEWs were absent for many key weeks in summer 2006.

Thesis Supervisor: Earle R. Williams
Title: Principal Research Engineer

Acknowledgments

My advisor, Earle Williams, has greatly supported every stage of this research, and I am grateful for his experience, scientific insight, and thoughtful support.

I thank the Climate Dynamics Program at the National Science Foundation (J. Fein, Grant #ATM 0734806) for supporting this work and my graduate studies.

The work of Carlos Morales (University of Sao Paulo, Sao Paulo, Brazil), Vassiliki Kotroni (National Observatory of Athens, Athens, Greece), and Manos Anagnostou (University of Connecticut, Storrs, Conn.) in integrating VLF networks to produce lightning stroke measurements, and Ramesh Kakar at NASA in supporting the ZEUS/STARNET network during the NAMMA, was essential to this paper and is greatly appreciated.

Diana Bou Karam and Daniel Rosenfeld (Hebrew University, Israel) encouraged the use of SEVIRI satellite data in the examination of dusty gust fronts.

Chris Thorncroft and Matthew Janiga (State University of New York at Albany) were valuable collaborators on the synoptic/AEW aspects of this study.

Discussions on these topics with Arlene Laing (UCAR/COMET, Boulder, CO) are greatly appreciated.

Valuable assistance in the collection and organization of data was provided by MIT radar observers A. Ali, F. Angelis, M. Dafalla, E. Freud, K. Gaptia, E. Hicks, T. Lebel, N. Nathou, C. Pontikis, T. Rickenbach, B. Russell, A. Williams, and G. Williams. Mark Miller provided important advice on the use of ARM data.

On a personal note, I thank Marissa Vogt for her constant support throughout the course of my research. All my friends have helped greatly: among them, I thank Tiffany Dohzen, who encouraged my M.Eng studies; Austin Chu, for his excellent advice; Nicholas Semenkovich, who freely offered LaTeX experience; and John Hawkinson and David Templeton, who gave technical assistance in presenting data.

I am deeply grateful to my family for their support and encouragement, and I would like in particular to acknowledge the wisdom and kindness of my grandfather, Robert E. McGraw, who passed away in December 2009.

Contents

List of Figures

List of Tables

Chapter 1

Introduction

To model and predict the behavior of West African storms and mesoscale convective systems (MCSs), we must understand the life cycle of gust fronts, which often accompany storms or initiate them. We began with observations of 40 gust fronts from the MIT radar at Niamey, Niger, bolstered by observations by the ground staff operating the radar. We characterized those gust fronts using ARM Mobile Facility measurements, then we developed additional long-range context using SEVIRI geostationary satellite infrared imagery on 30 of those gust fronts. To enhance our understanding of the long-term effect of gust fronts, we tracked isolated MCSs and squall lines using lightning strike measurements from the ZEUS and STARNET VLF lightning networks. We contribute a way to measure front propagation throughout July–September 2006, showing gust fronts that travel more than 1000 km, and we explore a surprising level of organization in lightning activity, including "stripes" of organized convection-associated lightning which last for up to 5 days, much longer than the typical duration of an MCS. We then explain how gust fronts could help mediate this organized convection.

1.1 Gust fronts

Gust fronts are also called outflow boundaries because they are are pools of cold air separated by a thin interface from their warmer surroundings and originating from the evaporation of precipitation in dry air. They can occur at the storm scale or as mesoscale events, and they can travel for 24 hours or more and for hundreds of kilometers (and, our observations show, more than a thousand km). They create low-level wind shear (*Fujita*, 1986) which explains their importance to aviation. When gust fronts with strong low-level wind shear interact with other boundaries, they can create new convection (*Wilson and Schreiber*, 1986). Gust fronts appear in satellite imagery as arcs of low cloud and on radar as a thin line representing detritus and insects in the rising air.

1.2 Haboobs

In West Africa, gust fronts which loft dust are called haboobs (from the Arabic verb *habūb*, which means *blowing furiously*) and make a formidable impression on ground observers as a fast-moving, tall wall of sand and fine dust often thick enough to blot out the sun. A dusty gust front at Niamey, Niger is shown in Figure 1-1.

Sutton (1925) characterized haboobs in the Sudan, where he observed haboobs with height of 1000 m or more and occurring commonly from May to October and noted that their passing was associated with a temperature drop. The haboobs he observed generally appeared to be small, strong, sand storms. Further study (*Sutton*, 1931) found that some, but not all haboobs were associated with precipitation — a more common event later in the rainy season than earlier — and about a third were associated with thunder or lightning, with the frequency of occurrence again increasing in later months. *Sutton* (1931) observed a diurnal cycle in haboobs seen at Khartoum, with a peak from 1800–2000 local time and a quiet period from 0400–1200 local time. In Section 5.1 we report observations that generally agree with *Sutton* except in one important way: he saw haboobs as purely local events with extent perhaps tens of kilometers, while we show evidence of dusty gust fronts whose extent is so large that it cannot be fully detected with ground-based radar.

The significant effect of haboobs on aviation makes it important to be able to predict where they will appear and where they will go. An unexpected haboob disrupted

Figure 1-1: This photograph of a dusty gust front in Niamey, Niger was taken by Brian Russell. The photo shows a typical dusty gust front structure: a layer of dust, topped by a white section of cumulus cloud that results from lifting in the gust front updraft over the top of the dust layer.

the rescue of Iranian hostages in 1980 (*Wilkerson*, 1991), and the microbursts that create haboobs have been blamed for serious civil aviation accidents (*Fujita*, 1986) because their strong vertical wind shear is difficult to forecast.

In West Africa, isolated storms occur frequently throughout the summer. As a thunderstorm enters the mature stage, a downdraft develops, ultimately creating a microburst or downburst (*Fujita*, 1986) containing rain which, in the arid desert, evaporates before it hits the ground (*Wilkerson*, 1991). Evaporative cooling makes the downburst a gust of dry, cold air which entrains dust on the desert surface, creating a thin dusty gust front characterized by strong internal winds. The circumstances which create isolated thunderstorms frequently follow diurnal cycles (*Janiga et al.*, 2009), which explains *Sutton*'s observations of a diurnal cycle in gust fronts at Khartoum and likewise matches our observations (Figure 5-2).

1.3 MCSs and squall lines

The circumstances that give rise to a single thunderstorm may also create a group of cells of strong, cold convective activity surrounded by cells of cells of moderate strength, which are initiated, propagate, and dissipate in an organized fashion collectively called a mesoscale convective system (MCS) (*Machado et al.*, 1998). The distinction between an MCS and a single large thunderstorm or "supercell" is often not clear in practice, especially when observations are made with low-resolution satellite images.

A particular kind of MCS common to West Africa is the squall line, an organized line of thunderstorms. These systems are characterized by a leading edge of convective cells typically hundreds of kilometers long but sometimes more than 1000 km long (*Rowell and Milford*, 1993). Anvil cloud extends behind this leading convection; the and is associated with additional, weaker rainfall that is called trailing stratiform precipitation. Squall lines are considered the most important convective systems in West Africa because they influence the movement of the monsoon front during the June-September rainy season and can themselves initiate new squall lines (*Peters*

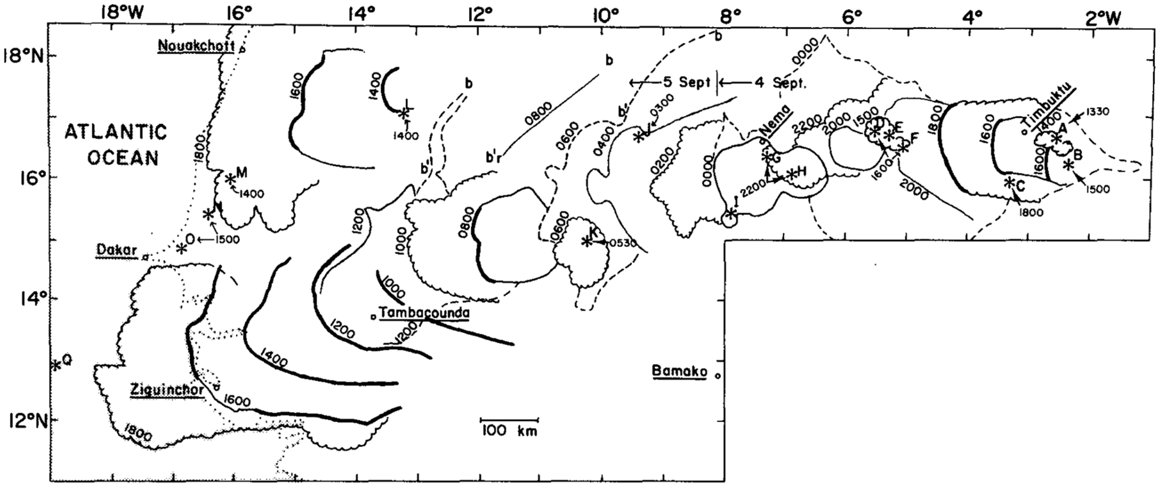

FIG. 1. The advance of the squall-line disturbance on 4 and 5 September 1974 from its origins to the Atlantic. Asterisks mark the points of origin of squall line elements A–Q, with the hour of origin indicated. Alternating scalloped and thin lines are the leading edge of the anvil cloud at 2 h intervals. Thick solid curves mark the position of the arc front on the visible pictures. Dashed lines outline the anvil every 6 h. The arcs emanating to the west of point K are the principal squall line whose evolution is depicted in Fig. 5. Line b–b′ is a long-lived but dormant arc of middle cloud.

Figure 1-2: This image, Figure 1 from *Fortune* (1980), shows the track of a single continuous system composed of multiple squall lines over 48 hours in September 1974. Compare with our Figure 4-1, which also shows the progression of fronts for a large, synoptic-scale system of squall lines.

and Tetzlaff, 1988) and because they contribute much of the total seasonal rainfall. Squall line generation is often influenced by the African Easterly Wave, especially at the West African coast (longitude 15W) and in the Sahel region (*Fink and Reiner*, 2003).

Fortune (*Fortune*, 1980) observed a single system composed of individual squall lines which themselves only propagated for 6-12 hours; however, he tracked a coherent "family" of these squall lines and other convection which propagated from 4–5 September 1974, moving for 48 hours over 2000 km as a series of curved squall line fronts (see Figure 1-2 for his graph of the squall line system's evolution).

In *Fortune* (1980), a squall line system represents a mesoscale or synoptic-scale perturbation in the mid-level wind field. Many MCSs exist which cannot be explained using the simple squall line model but include additional forms of convection; these MCSs can propagate for long distances and initiate new convection, so they are meteorologically significant. Within a squall line, the heavy rainfall of the leading edge is preceded by a well-marked gust fronts (*Chong et al.*, 1987). These gust fronts, like those generated from isolated thunderstorms, loft dust and create haboobs.

At the Niamey radar site, we observe gust fronts generated along squall lines and traveling within squall line systems as they travel for hundreds or thousands of kilometers. Most of the gust fronts we observed using satellite infrared imagery are associated with squall lines: although isolated thunderstorms outnumber squall lines in West African weather, squall lines travel further and are more likely to cross the Niamey site. Diurnal influence and local geography play lesser roles when squall lines cross our observation site because the squall lines last longer.

1.4 African Easterly waves

Long-lived seasonal perturbations in the mid-level wind field or in potential vorticity are the result of tropical waves, called African Easterly waves (*Reed et al.*, 1977). They can contribute to mesoscale convective activity and are also thought to originate from localized forcing (*Thorncroft et al.*, 2008). The strongest AEWs, associated with outgoing longwave radiation (OLR) signals that indicate deep convection (*Kiladis et al.*, 2006), have phase speed about 11.5 m/s east of 0 E and slow down to about 8.5 m/s as they head west over the Atlantic Ocean; they had wavelengths of 3000–3600 km, based on OLR measurements. Synoptic analysis of two main AEW tracks over West Africa at 5 N and 15 N found waves with period 3–5 days and 6–9 days and characterized the 6–9 day waves as more active in August–September than June–July, with mean wavelength 3000 km north of the African Easterly Jet (AEJ) and 5000 km south of the AEJ, and with mean phase speed 8 m/s north of the AEJ and 12 m/s south of the AEJ (*Diedhiou et al.*, 1999). The typical AEW with period 3–5 days is characterized with wavelength 2000–4000 km and phase speed 6–8 m/s (*Hsieh and Cook*, 2005); within the single season August–September 1985, the 3–5 day period waves had wavelength 2500 km and phase speed 8 m/s (*Reed et al.*, 1988).

There is not always an African Easterly wave over the continent, nor need there be only one — the troughs of multiple waves may be visible across the continent simultaneously. In 2006, organized wave behavior was particularly notable in late

August and throughout September (*Janiga*, 2010).

When squall lines are observed in the presence of an AEW, they typically form west of the trough (*Peters and Tetzlaff*, 1988) where northerly flow contributes vertical wind shear; when there is only a single wave on the continent and no trough to form west of, they may also develop in a secondary preferred region of development east of the ridge (*Schrage et al.*, 2006), where southerly flow introduces moist air in moisture-scarce regions. The largest contribution of the AEW to MCSs may be to their formation: Peters and Tetzlaff observed a mean squall line speed of 16 m/s, faster than wind speeds inside the African Easterly Jet[1], and remarked that these squall lines must be passing through the AEW, a comment shared by (*Fortune*, 1980) in a system which propagated about twice as fast as the AEW. We present an alternate theory in Section 5.8: long-lived squall line systems may be suppressed by an AEW, but they are nevertheless common occurrences in West Africa because of the frequent absence of a strong AEW obstructing squall line redevelopment. *Bou Karam et al.* (2010) showed another unusual situation where a squall line reaches the synoptic scale, and can even intensify an AEW, in a 3-6 August 2006 case where a thousand-kilometer arc of dust pushed across the continent and organized new convection along the front (*Bou Karam et al.*, 2010).

1.5 Thesis structure

Chapter 2 describes the instruments used to measure the propagation and physical properties associated with gust fronts and MCSs.

Chapter 3 is a conceptual review of the literature behind how gust fronts are thought to form, propagate, and assist new convection; how the aerosol in dusty gust fronts affects the weather; how MCSs propagate; how how AEWs interact with MCSs.

Chapter 4 explains the techniques used to turn the raw data described in Chapter 2 into processed values. We discuss how we generated gust front speed, propagation

---

[1] In "dry" and "realistic" simulations, the AEJ had maximum wind speed of 15 m/s in the west coast of Africa; in "wet" simulations, the AEJ had maximum zonal wind speed of 9 m/s(*Hsieh and Cook*, 2005).

distance, and duration, as measured by radar and satellite imagery; we show how to generate Hovmoller diagrams that depict the long-term movement of features identified in lightning strike data; and we describe the Lagrangian method used to quantify how much lightning is associated with an event.

Chapter 5 presents the key results of the thesis. It includes a tabulation of all observed gust fronts and a discussion of their diurnal and geographic frequency; an observational test of gust front speed and temperature drop that validates the density-current model; evidence for the conceptual model of gust front initiation in the form of Lagrangian lightning counts that show a way for us to quantify a storm's convective strength; and a large mean extent for satellite-observed gust fronts of 750 km. Finally, we discuss an intriguing phenomenon that appears in a diagram showing long-term lightning behavior: long, continuous "stripes" of convection as long as an African Easterly wavelength and twice as fast.

Chapter 6 concludes with a discussion of our contributions to the study of gust fronts and MCSs.

Chapter 2

Apparatus

This chapter discusses the devices used to measure the propagation and physical properties associated with gust fronts and mesoscale convective systems (MCSs). These apparatus include radar, satellite infrared sensors, surface meteorology instruments, and specially equipped radio receivers.

2.1 MIT Doppler Radar

A C-band ($\lambda = 5.30$ cm) Doppler radar used by the MIT Weather Radar Laboratory (*Russell et al.*, 2010) was operated from 5 July–27 September 2006 with lowest elevation angle 0.7 degrees and maximum recorded range 250 km in Niamey, Niger (13.4915 N, 2.1698 E, 224 m altitude) (*Chong*, 2009). See photographs of the installation, Figures 2-1 and 2-2.

Russell et al. (2010) gives a concise but thorough history of the device, dubbed the MIT WR-73 weather radar, which has seen wide use since its acquisition in the 1970s for use by the MIT Weather Radar Laboratory and operated aboard the R/V *Gilliss* during the Global Atlantic Tropical Experiment (GATE) (*Geotis*, 1978).

It has since traveled the globe; among the locations *Russell et al.* mentions are Borneo for the International Winter Monsoon Experiment (WMONEX) (*Houze Jr et al.*, 1981), North Carolina for the Genesis of Atlantic Lows Experiment (GALE) (*Engholm et al.*, 1990), Darwin, Australia for the Down Under Doppler and Electric-

Figure 2-1: The MIT radar installation at Niamey. Photograph taken 16 September 2006 by Brian Russell.

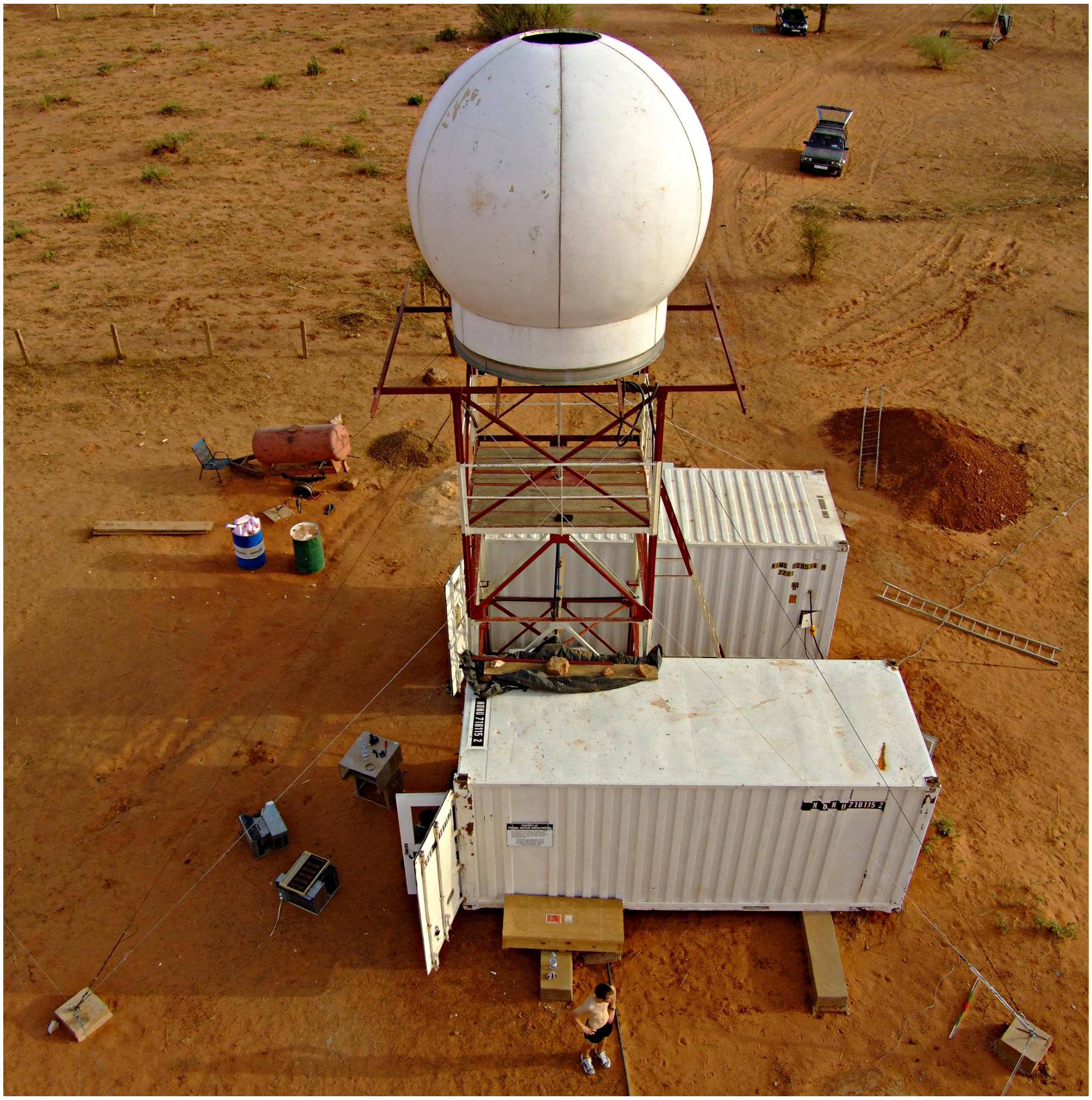

Figure 2-2: A photograph of the MIT radar installation at Niamey from the tower over the radar. Photograph taken 12 September 2006 by Brian Russell.

ity Experiment (DUNDEE) (*Rutledge et al.*, 1992), aboard R/V *John V. Vickers* off the coast of Papua New Guinea for the Tropical Ocean Global Atmospheres/Coupled Ocean Atmosphere Response Experiment (TOGA COARE) (*Rickenbach and Rutledge*, 1998), aboard R/V *Ronald H. Brown* in the middle of the Pacific Ocean about halfway between Hawaii and Ecuador for the Pan-American Climate Study (PACS) (*Yuter and Houze*, 2000), and in Alabama for microburst detection studies (*Williams et al.*, 1989). When not otherwise engaged, the MIT radar sits atop the Green Building.

Radar surveillance scans were recorded every 10 minutes. Of 40 gust fronts identified crossing the Niamey radar site in June–September 2006, 32 crossed while the radar was operational, and radar PPI images show 22 of those gust fronts crossing the Niamey site. The other 10 fronts are not documented only because not every surveillance scan was readily available; in every case where a surveillance scan was available and a gust front was observed, it was visible on the radar.

It is straightforward to locate fronts (though they are sometimes delicate) and the reflectivity signature associated with convection, with one important caveat: reflections off a large aircraft hangar create a phantom line that looks like convection in the southwest quadrant (see for example Figure 2-3, a surveillance scan showing the phantom line).

The curvature of the Earth, combined with the low height of a gust front's head (its radar-detectable features have a ceiling around 2 km) and the elevation angle of the radar imply a maximum radius of less than 80 km for detection of gust fronts.

Scans available for 1–2 July and 4–5 July were made with elevation angle 0.5 degrees and maximum recorded range 150 km. The lower elevation angle implies a lower beam bottom, so the radar should be able to detect gust fronts at slightly greater distances for those two scans.

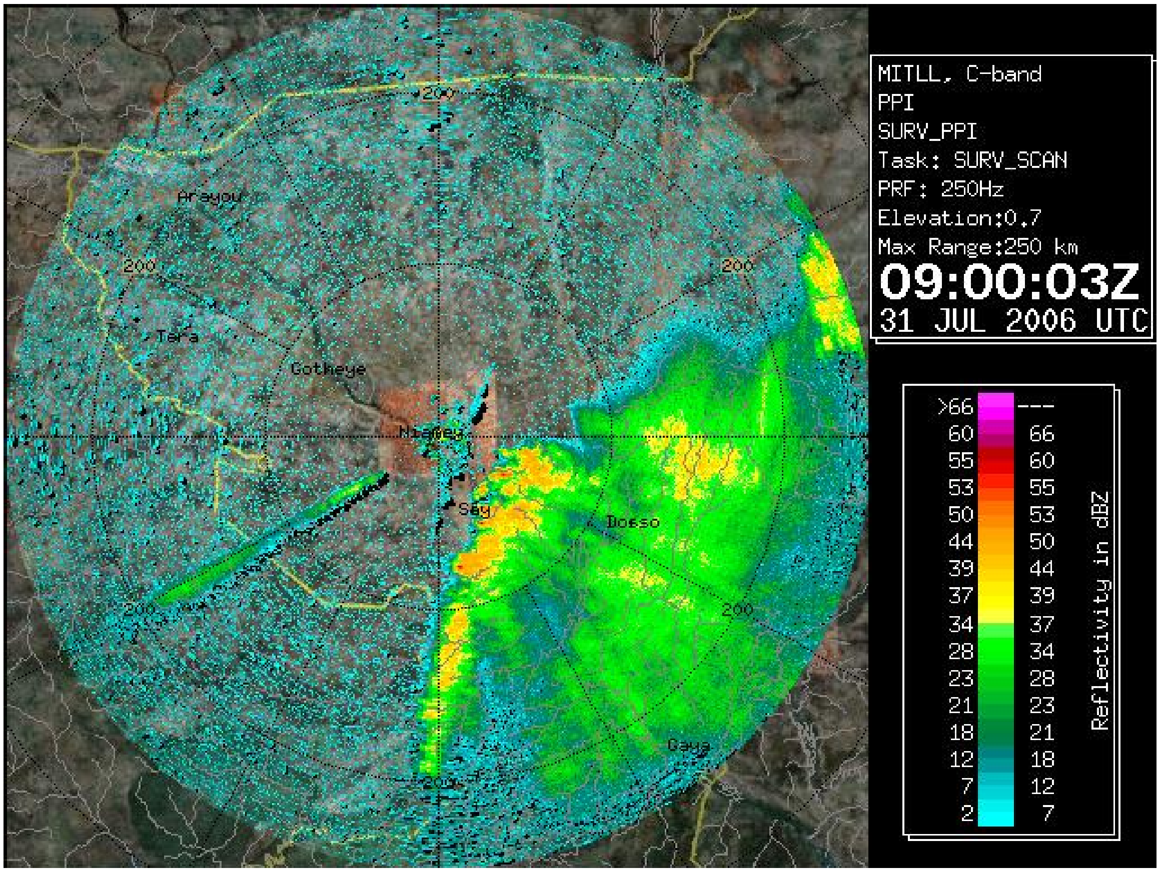

Figure 2-3: This radar surveillance scan for 31 July 2006 at 0900 UTC shows a gust front just east of the MIT radar site and the phantom line southwest of the radar site, caused by reflection off a large aircraft hangar nearby.

2.2 SEVIRI satellite imagery

The European Organisation for the Exploitation of Meteorological Satellites (EUMETSAT) operates two independent Meteosat Second Generation weather satellites in geostationary orbit around the Earth at approximately 0 degrees east, 0 degrees north (*Schmetz et al.*, 2002).

The satellites carry several instruments, including a radiometer called the Spinning Enhanced Visible and Infrared Imager (SEVIRI) with 12 channels that record 10-bit pixels in twelve image channels, ranging from 0.4µm–13.4µm. High-resolution (3 km) SEVIRI images of Europe, the North Atlantic, and Africa are made available at 15-minute intervals. The visible-to-infrared scale of the sensors allows the detection of shallow features with more precision than older satellite data products allowed.

Among EUMETSAT's data products is an RGB composite dust product, calculated based on three SEVIRI infrared channels and capable of revealing the transport of large amounts of lofted dust. In this product, the blue channel is created from the SEVIRI 10.8µm image, and the red and green channels are created by subtraction: red is 12µm - 10.8µm and green is 10.8µm - 8.7µm[1]. More sophisticated dust products that take advantage of information about the microphysics of dust are widely available (*Lensky and Rosenfeld*, 2008), but we elected to use the simple SEVIRI data product and found it highly effective in detecting dust movement associated with gust fronts. We sometimes found it helpful to examine only the green channel, which produces sharp boundaries along the edge of events but lacks the RGB product's power in qualitatively distinguishing dust from cloud and other IR-detected features.

The standard SEVIRI dust product is a "full-disc" image (see Figure 2-4) covering all of Europe and Africa and much of South America. This region is much larger than is interesting for our study of events in West Africa. We use an archive of these dust images as provided by the RADAGAST project (*Miller and Slingo*, 2007) and constrained to the region from 25 W to 25 E and 5 S to 30 N. Figure 2-5 shows one sample image of the SEVIRI dust product used for this research. The process

---

[1] This product thus ignores the 9.7µm ozone band.

used to transform these geostationary-projection images into rectilinear coordinates is documented in Section 4.5.

2.3 ZEUS/STARNET VLF lightning network

The ZEUS/STARNET lightning network (*Chronis et al.*, 2004) is an integration of radio receivers in Africa, Europe, and the Americas (*Morales and Anagnostou*, 2003) listening within the VLF range (specifically at 7–15 kHz) to measure the atmospheric radiation effects of lightning strikes. Atmospheric radiation pulses from lightning (sferics), primarily from the return strikes of cloud-to-ground flashes, can be triangulated using a technique traditionally called Arrival Time Distance (ATD), creating a long-range lightning network that can reliably locate lightning strikes in West Africa. With the ATD method, receivers have GPS-synchronized clocks and record the arrival time of sferics; when an event is detected by multiple receivers, those receivers' known location and the difference between arrival time creates a set of possible points and times where the lightning could have struck. A single event is detected in multiple receivers, creating many sets of data that can be intersected (or, equivalently, equations that can be solved) to find the lightning strike in space and time.

The number of active receivers in the ZEUS/STARNET network is ever changing. From 25 July–30 September 2006, "European" ZEUS receivers were active in Birmingham, U.K.; Roskilde, Denmark; Iasi, Romania; Larnaka, Cyprus; and Evora, Portugal; and "African" STARNET receivers were active in Adis Ababa, Ethiopia; Dar es Salaam, Tanzania; Bethlehem, South Africa; and Osun state, Nigeria. The location of events in 2006 also used additional Western-Hemisphere receivers, including sites in Guadeloupe; Fortaleza, Brazil; and Sao Paulo, Brazil. Reprocessed data are available for a slightly shorter interval, from 1 August–30 September 2006. The full network recorded 18.4 million strikes for August 2006 and 34 million strikes in September 2006. The complete data set is available online at *http : //www.zeus.iag.usp.br/AMMA/ftp/tar/* but remains provisional and subject to additional reprocessing (*Morales*, 2010); with additional preprocessing to include

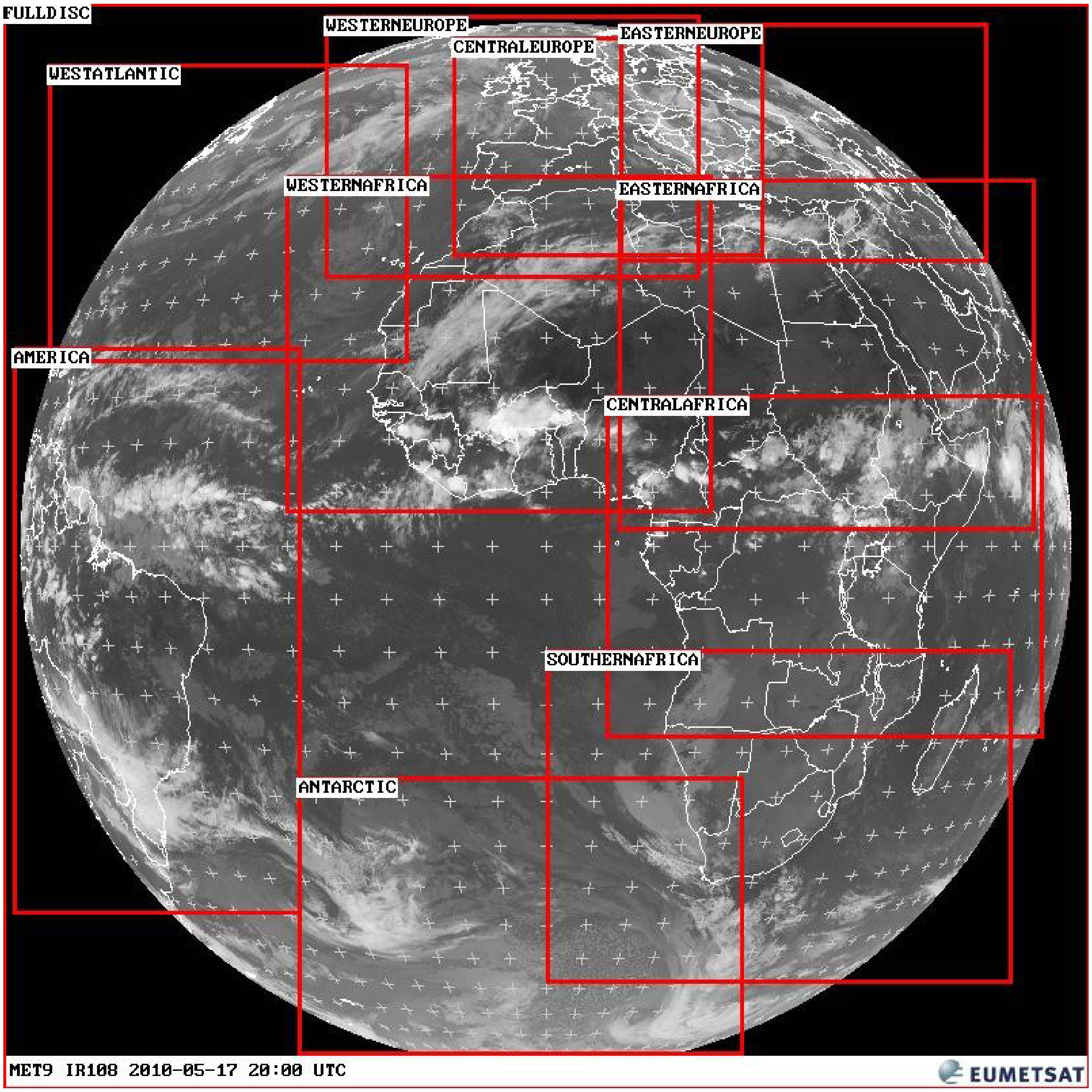

Figure 2-4: The SEVIRI 10.8μm “full disc” image from 17 May 2010 at 2000 UTC for 30 August 2006 at 0730. The A circle is shown with radius approximately 250km and centered over Niamey, the same bounds shown in our radar PPI images

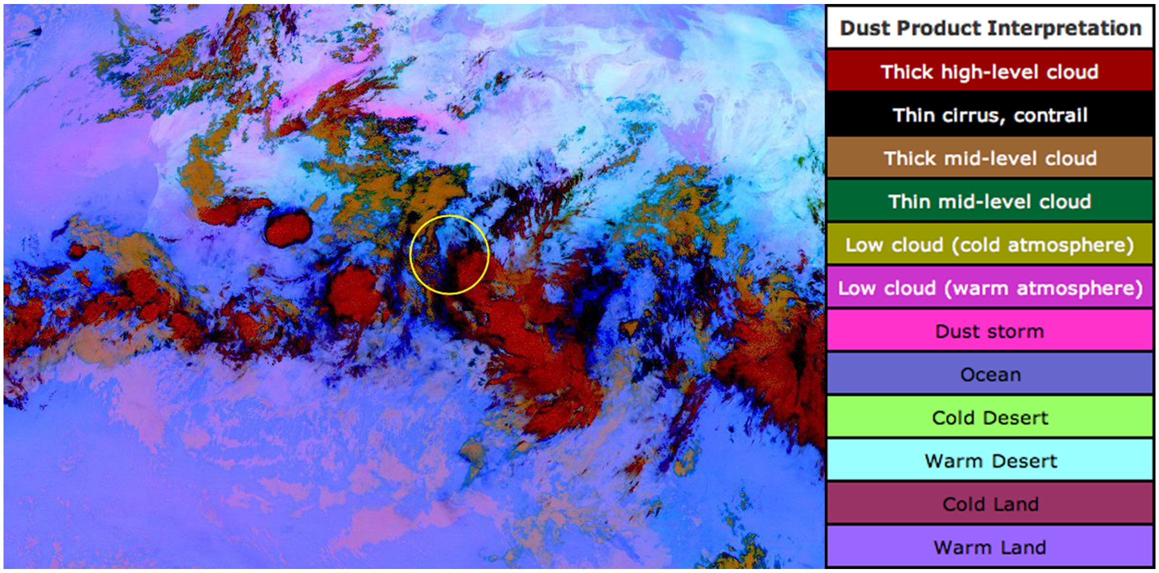

Figure 2-5: The SEVIRI dust product for 30 August 2006 at 0730. A circle is shown with radius approximately 250km and centered over Niamey, the same bounds shown in our radar PPI images

only strikes with less than 20 microseconds of residual error in the ATD solution (a method *Morales* (2010) recommends), we obtained useful data.

The time error of these data is reportedly on the order of 1 millisecond. The spatial error of these data is reportedly 10–20 km within the network, so they are especially useful in the aggregate for tracking events that generate substantial numbers of lightning strikes, like MCSs and squall lines. This reported error is consistent with an error analysis of the ZEUS network in 2003 when it consisted of six receivers throughout Europe (*Chronis and Anagnostou*, 2003); its error was found to be less than 40 km within the network (mode 20) and less than 400 km (mode 220 km) for locations $>$ 5000 km outside the network The convective environment around Niger is within a few hundred kilometers of the monitoring station at Osun, Nigeria and surrounded by other stations, so we should expect to see low, in-network spatial error for all lightning measurements we use. We overlaid these lightning strikes on top of SEVIRI dust product images (Section 4.5) and found that the two generally agreed; the lightning strikes plotted in aggregate appear to show squall lines, MCSs, and isolated thunderstorms atop those features as detected in SEVIRI dust product data. The lightning data include a few unusual features, such as a tendency to show a sharp diagonal line of strikes along a front which overshoots the actual front boundary as shown in previous and subsequent lightning and dust product images; so it is helpful to compare them with satellite images. Likewise, the satellite images sometimes show apparent strong cloud activity and dust movement which actually has few corresponding lightning strikes; lightning strike data enhances our understanding of exactly when convection regenerates along a gust front and when a storm has dissipated most of its convective energy, but its associated cloud continues to move.

2.4 ARM Mobile Facility surface meteorological station

We use one-minute-resolution data from the surface meteorological instrumentation of the Atmospheric Radiation Program Mobile Facility (*Ackerman and Stokes*, 2003) deployed in Niamey in 2006 to coincide with the African Monsoon Multidisciplinary Analysis (AMMA) (*Redelsperger et al.*, 2006). Data from ARM (see installation photographs, Figure 2-6) and AMMA have helped focus attention on Saharan dust storms, where surface stations provide information about the dust's optical properties and its contribution to radiation balance that cannot be inferred from satellite information alone (*Slingo et al.*, 2006). The ARM Mobile Facility's high-frequency samples of basic surface station measurements — visibility, wind speed and direction, temperature, moisture, and rainfall — provide key data that have greatly improved our understanding of gust front behavior. The instruments do, however, represent only a point sample, so their measurements may not be complete representations of conditions all along a front.

Wakimoto (1982) found that as gust fronts at mid-latitude crossed a surface station, meteorological instruments recorded a pressure rise, followed by a wind shift, then a wind surge, a temperature drop, and finally rainfall. Figure 5-14, a plot of ARM Mobile Facility instrument data from 11 July 2006, shows a sample case that validates this pattern. The data available from the ARM site are extravagant in

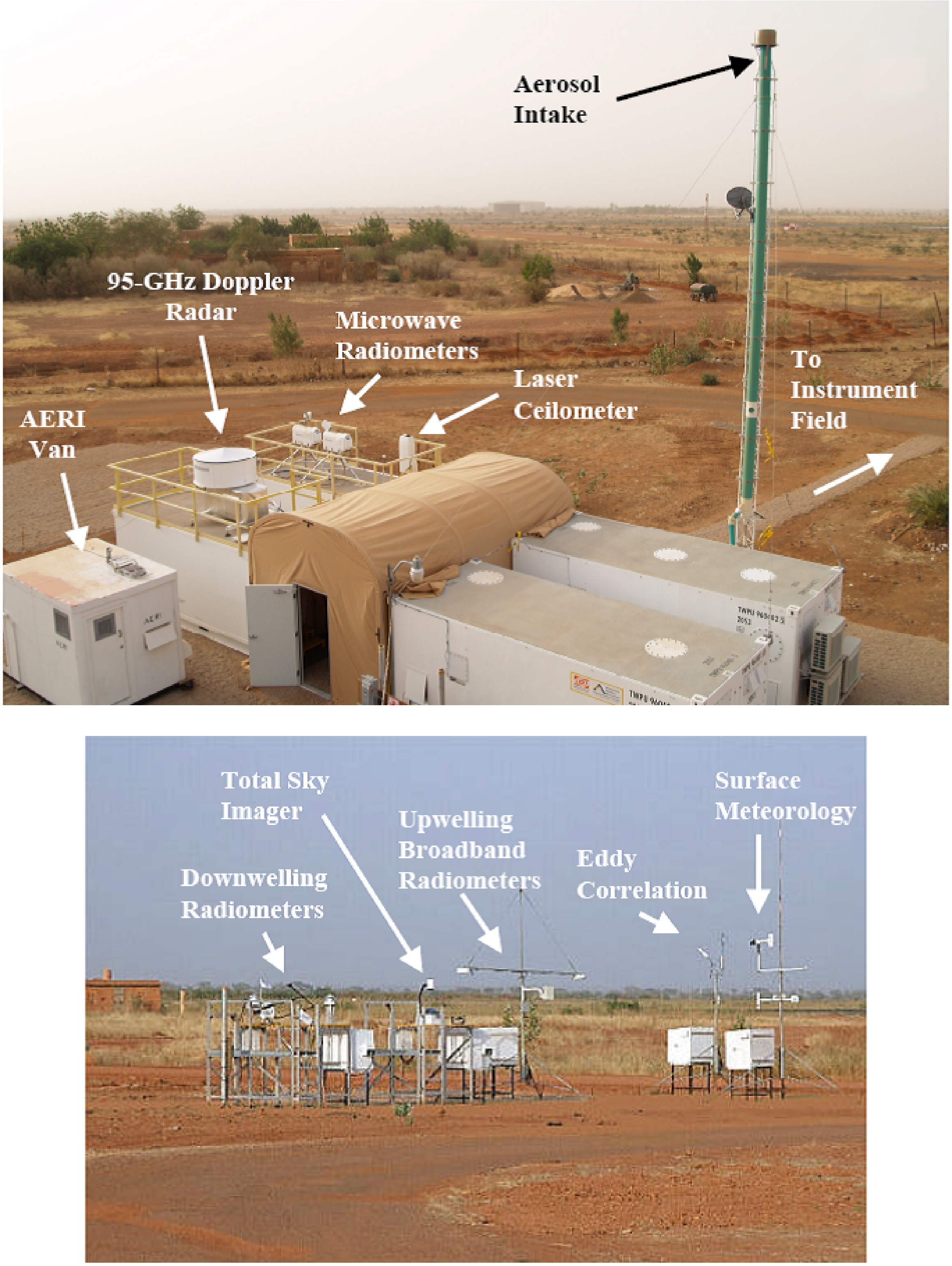

Figure 2-6: Top: the Atmospheric Radiation Program Mobile Facility in Niamey, Niger. Bottom: the associated instrument field, approximately 100 m from the main facility. Photos from Sally McFarlane and attributed to Mark Miller.

their reliability, high 1-minute sampling rate, and availability of corroborating data from additional sensors. However, the quantities they measure are basic enough that gust front signatures can be sought among data from other surface stations in Africa, for example one-hour resolution data widely available in surface stations throughout the continent. We have documented evidence of a particular gust front studied by *Bou Karam et al.* (2010) using surface station data from Agadez, Niger; In Salah, Algeria; and Tamanrasset, Algeria.

2.5 ECMWF vorticity analysis

The European Centre for Medium-Range Weather Forecasts provides daily global analyses and reanalyses at 0000, 0600, 1200, and 1800 UTC that forecast common atmospheric factors including wind and temperature. To understand MCS interaction with synoptic-scale African Easterly waves, we have relied on the interpretation of another ECMWF data product, the interim reanalysis, which provides potential vorticity at 700 hPa at 1.5 degree resolution. (Vorticity measures the rotation of the air at that altitude relative to the Earth's surface, with a positive vorticity meaning clockwise motion.)

2.6 CALIPSO satellite lidar

NASA's Cloud-Aerosol Lidar and Infrared Pathfinder Satellite Observation mission (CALIPSO) carries three instruments: the 532 nm and 1064 nm Cloud-Aerosol Lidar with Orthogonal Polarization (CALIOP) (*Winker et al.*, 2007), the Imaging Infrared Radiometer (IIR), and the Wide Field Camera (WFC). CALIPSO and the CloudSat satellite (which measures clouds with a W-band radar) were integrated in April 2006 into a formation of three other satellites, collectively called the "A-Train", which fly along a 705 km sun-synchronous orbit and cross the equator at 1330 local time (*McGill et al.*, 2007). The same location on the ground is measured by each satellite within a 15-minute interval, and CALIPSO and CloudSat are kept within 15 seconds

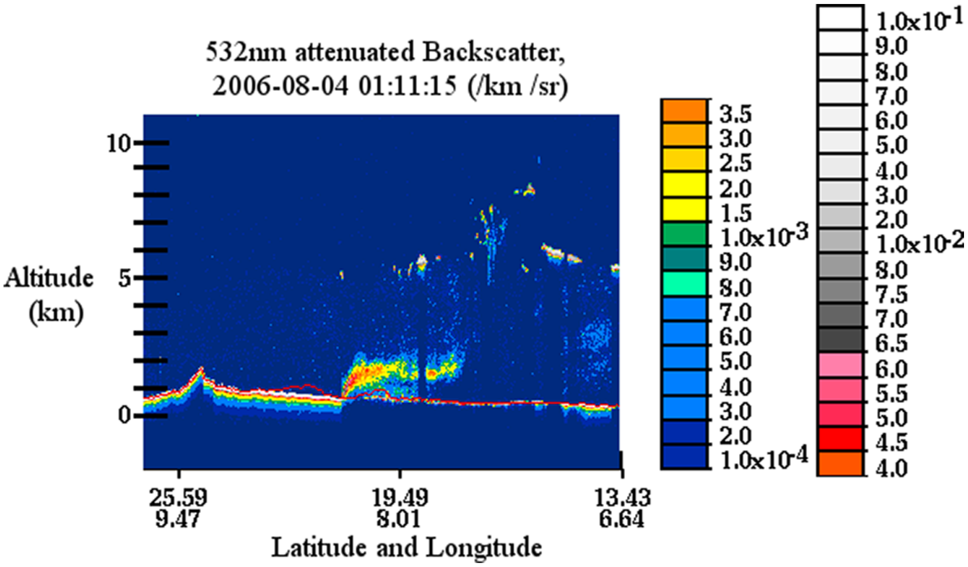

Figure 2-7: The CALIPSO lidar image of a gust front on 4 August 2006, as reported in *Bou Karam et al.* (2010), shows a gust front with a head approximately 2 km high.

of one another.

Attempts to locate intersections of gust fronts with CALIPSO lidar were largely unsuccessful, in part because the CALIPSO lidar's observation grid covers a different vertical track every few days, reducing the number of times where an intersection is possible, and in part because gust fronts are narrow features oriented mostly north-to-south, and the lidar track is also narrow and oriented north-to-south. Intersections with a synoptic-scale event with a gust front oriented west-to-east were successfully located in *Bou Karam et al.* (2010). The relevant portion of the CALIPSO track is reproduced in Figure 2-7, showing a 2 km height for the gust front's head.

Our research has shown a way to identify gust fronts' precise location as they are launched and propagate across Africa using geostationary satellite imagery. This improved view of gust front location and propagation distance means that future attempts to find CALIPSO intersections with gust fronts are likely to be substantially more successful than attempts to locate intersections using spatially restricted radar data alone.

Chapter 3

Conceptual background

This chapter introduces the concepts behind how gust fronts are thought to form, propagate, and assist new convection; how the aerosol in dusty gust fronts affects the weather; how mesoscale convective systems (MCSs) propagate; and how African Easterly waves (AEWs) interact with MCSs.

3.1 Gust front initiation

The Thunderstorm Project (*Byers and Braham*, 1949) identified three phases of a thunderstorm: the cumulus stage, typified by an updraft of air traveling about 1–30 m/s as clouds grow and accumulate water, and drops begin to fall; the mature stage, in which the updraft continues but is adjoined by a downdraft caused by evaporative cooling when massive water droplets and graupel particles drag air downward; and the dissipating stage, in which air flows predominantly downward until the cloud breaks up.

As a thunderstorm enters the mature stage, the initial downdraft cools down relatively slowly, and mixture with outside air results in evaporative cooling that keeps the downdraft cold relative to its surroundings. An outflow of cold air is thus directly associated with the downdraft. When the outflow is associated with strong winds, a persistent discontinuity forms between the outflow and the surrounding air; this outflow boundary outruns the rain and is detected miles beyond the periphery of the storm cell. *Byers* (1949) reported that the first gust of air from a downburst is the strongest (a view confirmed by the laboratory models of *Fujita et al.* (1990)). They propose that strong winds continue to be associated with the cold outflow, with the wind speed and "gustiness" decreasing as the air spreads farther away. They add a caveat that the gust front's wind speed may be sustained if a nearby cell reaches the mature stage and releases a new burst of cold air to sustain the existing gust front. This is the case for a row of thunderstorms making up a squall line, where each new convective cell provides more cold air to a cold pool. If each thunderstorm experiences a downdraft and launches a gust front in concert, a one-dimensional gust front is launched parallel to the parent squall line.

3.2 Gust front propagation

A gust front can be modeled physically as a density current, sometimes called a gravity current, an event where a density contrast exists between two fluids (in this case, between the cold, moist front and the warm, dry surroundings) (*Simpson*, 1982). The current is sustained as the warm air rises above the head of the current to produce mixing billows. The shape of a dusty gust front, or haboob, has been found to match closely with the shape of laboratory models of density currents made by introducing salt into fresh water (*Simpson*, 1969). A single gust front was examined by *Charba* (1974), who found that its structural characteristics (head at 1700 m, cold air with constant depth 3350 m upstream of the head, wind speed surge slowed at the ground by frictional drag, large vertical wind shear at front edge) showed much similarity with laboratory simulations.

Knippertz et al. (2009) conducted numerical simulations of three gust fronts, treated as density currents, and performed sensitivity studies to show that the position and propagation direction of a density current depends largely on the initiation parameters of deep convective cells; that is to say, the problem forecasting gust fronts was found to be essentially a problem of forecasting moist convection. One microphysical result of the sensitivity study did affect gust front speed: when the turbulence length used for vertical mixing was increased, precipitation was more common but weaker, and the gust front was reportedly larger and faster, with higher winds. The theoretical density current propagation speed, for incompressible steady flows, is often given as $V_f = k(gH\Delta\rho/\rho)^{1/2}$ (*Droegemeier and Wilhelmson*, 1987) and depends on g, acceleration due to gravity; k, internal Froude number; $\Delta\rho$, the contrast in air of a density current across the front; ρ, the density of the environment; H, the height of the density current head or of the cold air upstream of the head. Numerical models based on this relationship found that gust front head depth and propagation speed depended primarily on the outflow's vertical temperature distribution (explaining why in atmospheric tests, the ratio $\Delta\rho/\rho$ is sometimes replaced by $\Delta T/T$). A similar equation proposed by *Wakimoto* (1982) is tested in Section 5.4.3.

Traditional models of gust fronts as density currents are one-dimensional; the gust front propagates "forwards" and the squall line is "behind" the gust front. In satellite observations of two-dimensional gust fronts which form as circular outflows from isolated thunderstorms, we observe these fronts propagating quickly after the initial outflow, then slowing down. The behavior of two-dimensional outflows has been studied in the context of viscous fluid dynamics: *Simpson* (1987) (citing (*Huppert* (1982) and *Didden and Maxworthy* (1982)) distinguishes between "radial" (one-dimensional) and "two-dimensional" gravity currents. For the radial case, velocity and time are related $V \sim t^{-7/8}$, while the relationship for the two-dimensional case is $V \sim t^{-1/5}$. These theoretical results, although designed for a viscous model, are consistent with our qualitative observation that gust front velocity declines over time more quickly for isolated thunderstorm outflows compared with outflows from squall lines.

3.3 Gust front-initiated convection

The analysis of thermodynamic soundings (*Williams and Renno*, 1993) has shown that much of the tropical atmosphere is conditionally unstable. In many situations, a finite vertical displacement of a surface parcel is sufficient to release the instability and create moist convection.

Wilson and Schreiber (1986) found that most new storms form near a boundary like a gust front and that boundaries are associated with the resurgence of old storms, with storms very likely to form within 0–20 km of a moving boundary, within 15 km of a stationary boundary, and within 5 km of colliding boundaries. They theorized that when boundaries collide, forced lifting intensifies, making new convection easier to form. In their study, colliding boundaries which created new atmospheric instability, as measured by comparing condensation temperature versus sounding temperature, were most likely to create new convection or strengthen existing convection.

Regeneration of convection along a single squall line was modeled by *Crook et al.* (1990), a study which found three characteristics in the regeneration: an increase in low-level moisture; an increase in low-level shear; and a mesoscale oscillation, or "sloshing", in which a convective system's subsidence stage feeds the formation of a new convective system along the first system's gust front. Even when a storm is convectively inactive, the gust front still forces velocity on the order of 6–7 m/s, a factor *Crook et al.* (1990) deliberately excluded from models to isolate the mesoscale oscillation effect. This effect was explained as the atmospheric response to the heating and cooling of the convective system.

An analysis of 30 gust fronts with average head depth 1.3 km, average temperature drop 3.5 C, and average propagation speed 8.6 m/s (*Mahoney*, 1988) found that outflow boundaries can create new convection by mechanical forcing, or by a mechanism that makes strong updrafts, extending higher than boundary layer tops, and creates circulation that gives rise to new convection. Curiously, the gust front speeds recorded by Mahoney do not correlate well with measured temperature drop, as we found with ARM data (Figure 5-19 in Section 5.4.3).

3.4 Characteristics of dusty events

Not all gust fronts are dusty. Gust fronts at mid-latitude propagating over vegetated terrain are nearly invisible. But nearly all gust fronts over the semi-arid Sahel and the arid Sahara are prominently dusty. Vertical dust flux is related by a cubic function to wind speed (*Cakmur et al.*, 2004), and the strong vertical wind shear associated with gust fronts lofts large amounts of dust.

Whether gusty dust fronts affect convection differently, and the specific effect of dust, can be understood as a case of the general problem of the effect of aerosol particles on convection, a question which is especially timely for global climate models. Qualitatively, increasing aerosol concentration results in more cloud condensation nuclei, a key factor in the microphysics of convection. But the literature is conflicted on what, exactly, those extra CCN do — in *Rosenfeld* (1999), smoke from forest fires almost completely suppressed tropical warm rain processes, and air pollution was found to suppress rainfall in extra-tropical locations. Subsequent numerical modeling (*Khain and Pokrovsky*, 2004) reproduced this result, showing that under cloud-dynamics models, high aerosol concentrations will increase the height at which rainfall begins. *Fan et al.* (2007) used simulations to create the more nuanced hypothesis that aerosol has minimal effects on cloud microphysics for dry air (40% surface relative humidity), but in moist conditions (60–70% surface RH), increases in aerosol concentration will increase cloud water content and create stronger precipitation and more intense radar reflectivity within convective systems.

Local storms loft significant amounts of dust and can contribute to the dustiness of West Africa far from the initial convection; in a 7–8 July 2006 case (*Bou Karam et al.*, 2009), a dry cyclone that formed over Niger created strong surface winds of about 11 m/s and lofted substantial amounts of dust to 4–5 km altitude, where it was available for long-range transport over distances far exceeding the cyclone's 400 km width.

Other effects of African dust on weather have been noted by *Anuforom* (2007), who remarked that Saharan dust has been shown to affect radiative balance (*Diaz et al.*, 2001) and atmospheric electrical properties (*Ette*, 1971) (also studied recently in the Sahel by *Williams et al.* (2009)). *Flamant et al.* (2009) studied a 5–6 June 2006 case and found that large amounts of dust in a gust front affect not just the cloud, but also the insolation in the region of the Sahelo-Saharan planetary boundary layer, affecting the development of the intertropical discontinuity (ITD), the movement of which is a key synoptic-scale driver for the rainfall of the monsoon season.

3.5 MCS behavior with size

Satellite analysis of the cloud associated with 3200 deep convective systems (regions with satellite infrared temperature $T_{IR} = 245K$ or lower) by a tropical meteorologist and 4700 by an automated system found that the average radius of the MCS is linearly correlated with the average lifetime (*Machado et al.*, 1998); the results were the same for the manually and automatically tracked systems, although the reported average size of an MCS was 20–30% higher for the automatically tracked MCSs, suggesting sensitivity issues in the process. The larger systems were found to have larger system-average reflectance and more, larger, colder convective clusters (highly active, cold T_{IR} ¡ 218 K, centers of convection). Larger system reflectance was correlated with system lifetime, a result which supports the measurements of *Mathon and Laurent* (2001) that larger MCSs have longer lifetimes.

Rotunno et al. (1988) discussed the theoretical underpinnings for how MCSs interact to form squall lines and provided a theory showing how independent, moderately sized cells of MCSs could interact without any need for a “special” kind of squall line MCS.

The observations discussed in Section 5.6 cast doubt on the idea that squall line MCS (SLMCS) speed increases with size, but evidence is also presented that SLMCS lifetime, propagation distance, and total lightning production all increase notably with size.

3.6 AEW interaction with squall line mesoscale convective systems

The propagation of AEWs is important to forecasters because there is a relationship between more AEWs leaving the African coast and a more intense Atlantic tropical cyclone season (*Thorncroft and Hodges*, 2001). An AEW can be triggered by convection that generates a MCS, as in *Berry and Thorncroft* (2005), a case study of an AEW in 2000 which was likely triggered by an MCS but which also triggered multiple new MCSs within the AEW's structure.

Strong convective systems are often triggered by strong shear in the African Easterly Jet (*Mohr and Thorncroft*, 2006), the same phenomenon which contains instabilities that give rise to AEWs. Simulations of the AEW and AEJ show that moist convection can reinvigorate AEWs, contributing to their development (*Cornforth et al.*, 2009). Understanding how and where MCSs form and propagate can thus improve our understanding of AEW behavior.

AEWs have long been thought to constrain the development and westward propagation of individual MCSs: in *Reed et al.* (1988) squall lines are shown to grow east of an AEW's ridge and die near an AEW's trough. According to this view, an MCS generated within an AEW is halted within that AEW. In *Payne and McGarry* (1977, Figure 10), convective cloud is shown to vary in quantity depending on its proximity to an AEW. Recent work by *Fink and Reiner* (2003) examining West Africa in 1998 and 1999 found a favorable location for squall line generation in the area west of the AEW trough (which, because of the nature of an AEW nature, is roughly equivalent to the area east of the ridge). That study showed a stronger influence of the AEW the further west it was located: AEWs contributed to 20% of squall line generation at 15 E and 68% of squall line generation at 15 W. The relationship between AEW and squall line organization was found to be strongest in August and September.

We show in Section 5.8 that SLMCSs in August and September 2006 that propagate distances substantially greater than half a typical AEW wavelength can do so because no prominent AEW is present.

Chapter 4

Processing sensor data

This chapter discusses the techniques used to turn the raw data from our apparatus into processed values. We discuss how we generated gust front speed, propagation distance, and duration, as measured by radar and satellite imagery; we show how to generate Hovmoller diagrams that depict the long-term movement of features identified in lightning strike data; and we describe the Lagrangian method used to quantify how much lightning is associated with an event.

4.1 Determining GF speed from radar images

4.1.1 Tracking gust fronts

Each individual image frame from the 10-minute radar surveillance scans containing a gust front was annotated with the location of the front, and the front's travel was tracked with "CellTracker" software, originally designed for tracking the movement of biological cells in microscopy (*Shen et al.*, 2006). Multiple tracks were annotated along different points of the radar-visible front, then a single track was created which represented the part of the front that crossed the radar site (generally the center of the visible portion) and traveled perpendicularly between each front as defined every 10 minutes. This averaging provides a better accounting for local variation in front propagation than simply using a single track. We also tried computing the area between the fronts and dividing by the average linear extent (based on the track measurements), but the calculation turned out to be unreliably sensitive to how much of the front was visible. We use the distance traveled along a track immediately before crossing the MIT radar site and immediately after, divided by 10 minutes, as an “instantaneous” speed associated with the radar crossing.

4.1.2 Errors in gust front speeds

Most of the MIT radar PPI images had resolution of 500 km / 480 px, meaning that an error of one pixel in a ten minute interval results in an error of 1.73 m/s in speed. (Two early scans in July had resolution 300 km / 480 px instead, so a one-pixel difference in ten minutes is a difference of 1.04 m/s in speed for those events.)

The manual process used to annotate tracks was performed by rigorously measuring gust fronts that extended for tens of pixels, so the actual error of the change in front movement has error at the sub-pixel scale, less than 1.73 m/s. In some frames more distant from the radar, the front cannot be seen well, and error may be higher (we infer the front’s position when we can see it in frame 1 and 3 but not 2, for example). It is easiest to see thin lines when they’re directly over the radar site, which means that the instantaneous speeds we report are the most accurate of any of the 10-minute speeds we recorded.

4.1.3 Propagation distances and times for gust fronts

This calculation also produced gust front propagation distances and times, which, owing to the limited horizontal resolution of the radar for low features, were quite short. For events where radar data was available and the gust front could be clearly measured, it had measurable extents from 4 to 18 frames, with a mean of 9.5, corresponding to being detectable in radar for 40 to 180 minutes, with a mean of just 95 minutes.

4.2 Determining squall line speed

4.2.1 Radar image processing

Rickenbach et al. (2009) analyzed a complete collection of MIT radar volumetric images from 5 July-27 September 2006 by manually tracking the leading edge of squall lines in successive images. Their work focuses on "squall line MCSs", the MCSs composed of a single strong squall line, which represent the most common type of MCS at Niamey from July-September. They produced speed information for 28 of those squall lines.

4.3 Determining gust front speed from satellite images

4.3.1 Manual annotation

The same manual annotation approach that generates speeds for radar images can be applied to SEVIRI satellite dust product imagery. Because the resolution of the images is lower, the stakes are higher: we use RADAGAST project images with 6.3 km/pixel resolution, for which a single pixel error in a 15 minute interval represents a difference in speed of 7 m/s. By limiting our measurements to change per 3 hours, we reduce error to 0.58 m/s per pixel. Our actual measurements were performed along events visible in tens or hundreds of pixels and were performed with enough rigor to ensure sub-pixel precision. This method works well only for dusty gust fronts with a large extent, hundreds of kilometers or more, whose progress can easily be tracked with relatively low-resolution images. Small gust fronts from moderately sized MCSs may appear as only a few pixels in SEVIRI images, at least initially. On the other hand, large fronts may vary substantially in behavior along local subsections of the front, and those variations can make it difficult to track the exact location of a large gust front.

We have used this technique to produce tracks for two gust fronts associated with

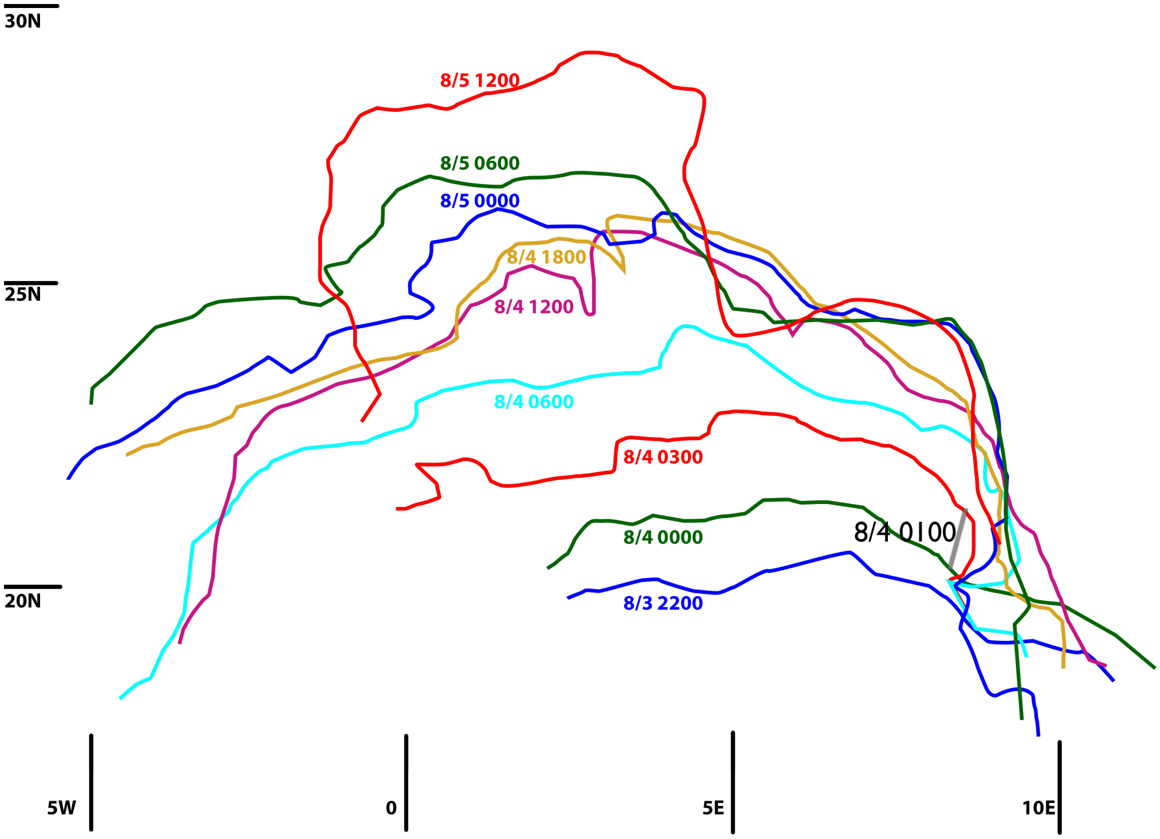

Figure 4-1: The track of the dusty gust front associated with a synoptic-scale event from 3-5 August 2006, propagating northward through West Africa. The gray line marked "8/4 0100" drawn perpendicular to the front between 5 E and 10 E is the intersection of CALIPSO satellite lidar with the front, shown in Figure 2-7 and discussed in *Bou Karam et al.* (2010).

a synoptic-scale event from 3-5 August 2006 (*Bou Karam et al.*, 2010), one headed north and the other headed west through Niamey, by applying a contrast-enhancing filter to the image, then manually creating a vector graphic that traced the front's edge exactly. We overlaid the individual tracks of the northward event to create Figure 4-1, which shows that this method is viable for tracking the motion of synoptic-scale events. The measured edges of the fronts change from image to image as the dusty gust front becomes more or less readily discerned from surroundings. The technique's key disadvantages is that it works well only for large events.

4.3.2 Automated measurements

To reduce error, we had to limit sampling to only every three or six hours. But this method seems to discard a disappointing amount of our 15-minute-resolution data. Luckily there is a solution: because we are more interested in the progress of fronts over time, we can use a method which discards almost all of the data at irrelevant locations and takes a cross section of the imagery along one possible track. This approach has been used when the actual track of an aircraft following a storm front was available (*Flamant et al.*, 2007) But we show how it can be used when a precise track of the storm is not already known, by using two possible tracks, one which stays at Niamey's latitude (13 N) and travels from east to west, and a second which stays at Niamey's longitude (2E) and travels from north to south. Since most of the gust fronts we study cross Niamey traveling predominantly east-to-west (with a few propagating north-to-south), this simple approach is effective.

A sample dust product cross-section is shown in Figure 4-2. The front can be tracked as it crosses 13 N and heads west over time. A false-color version of the green channel alone (Figure 4-3) shows the change even more clearly. We can mark the beginning and end of a dust product in one of these cross-sections to find its distance traveled (in degrees latitude or longitude, which are roughly 111 km in extent near 0 N, 0 E) and the total time involved. By computing the slope, we can measure the gust front's average speed over its entire detectable extent.

These cross-sections are effective at showing a front's movement but may be misleading if a front leaves 13 N or 2 E completely, so we additionally use these measurements to produce more careful estimates. Manual examination of the SEVIRI dust product images around the observed beginning and end times from a cross-section image lets us locate the precise latitude, longitude, origin time, and ending time for each gust front that crossed the MIT radar.

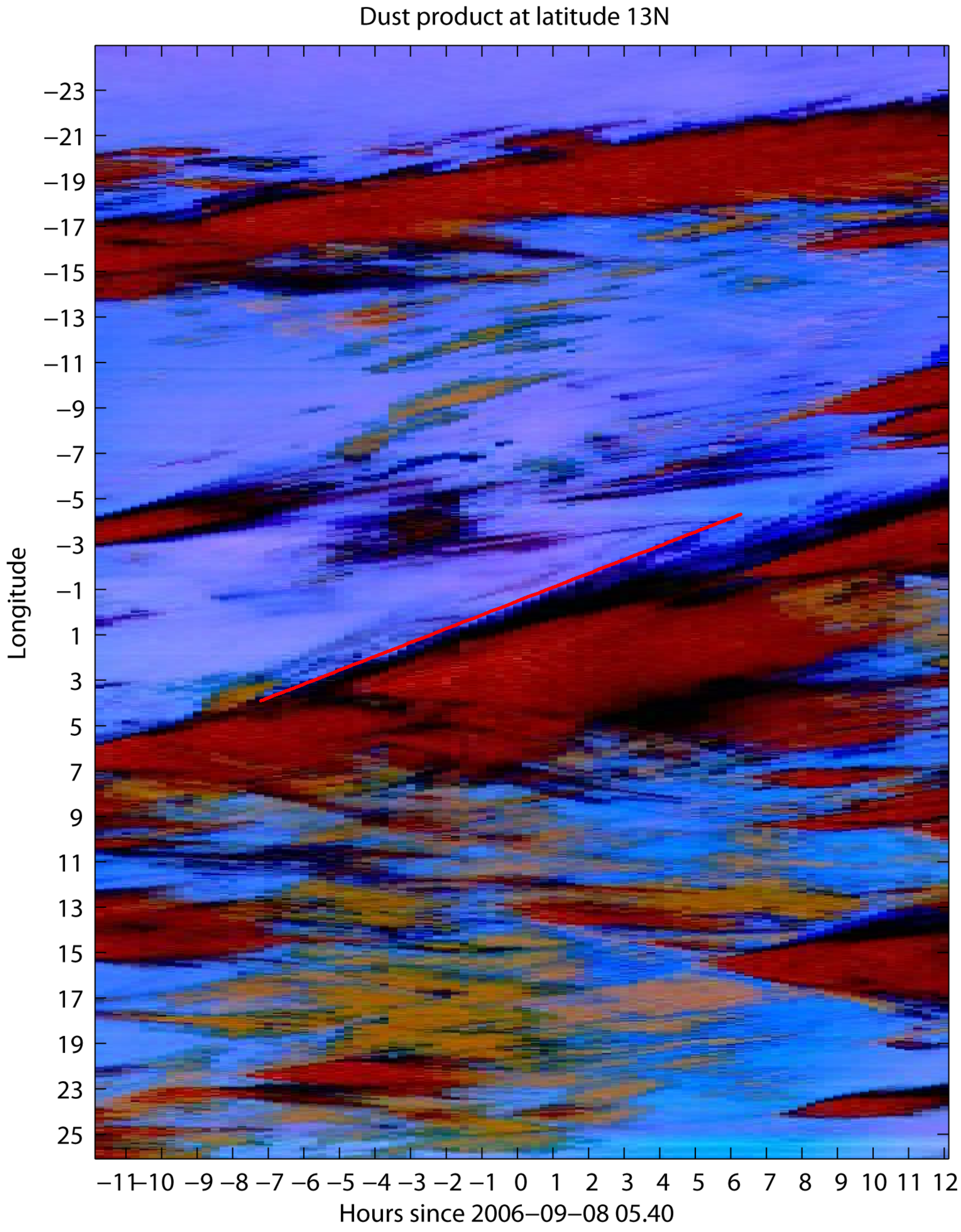

Figure 4-2: In this typical SEVIRI dust product cross-section, a gust front that crossed the MIT radar site (longitude 2 E) on 8 September 2006 at 0540 UTC is tracked in SEVIRI dust product imagery for the 12 hours before and after the crossing.

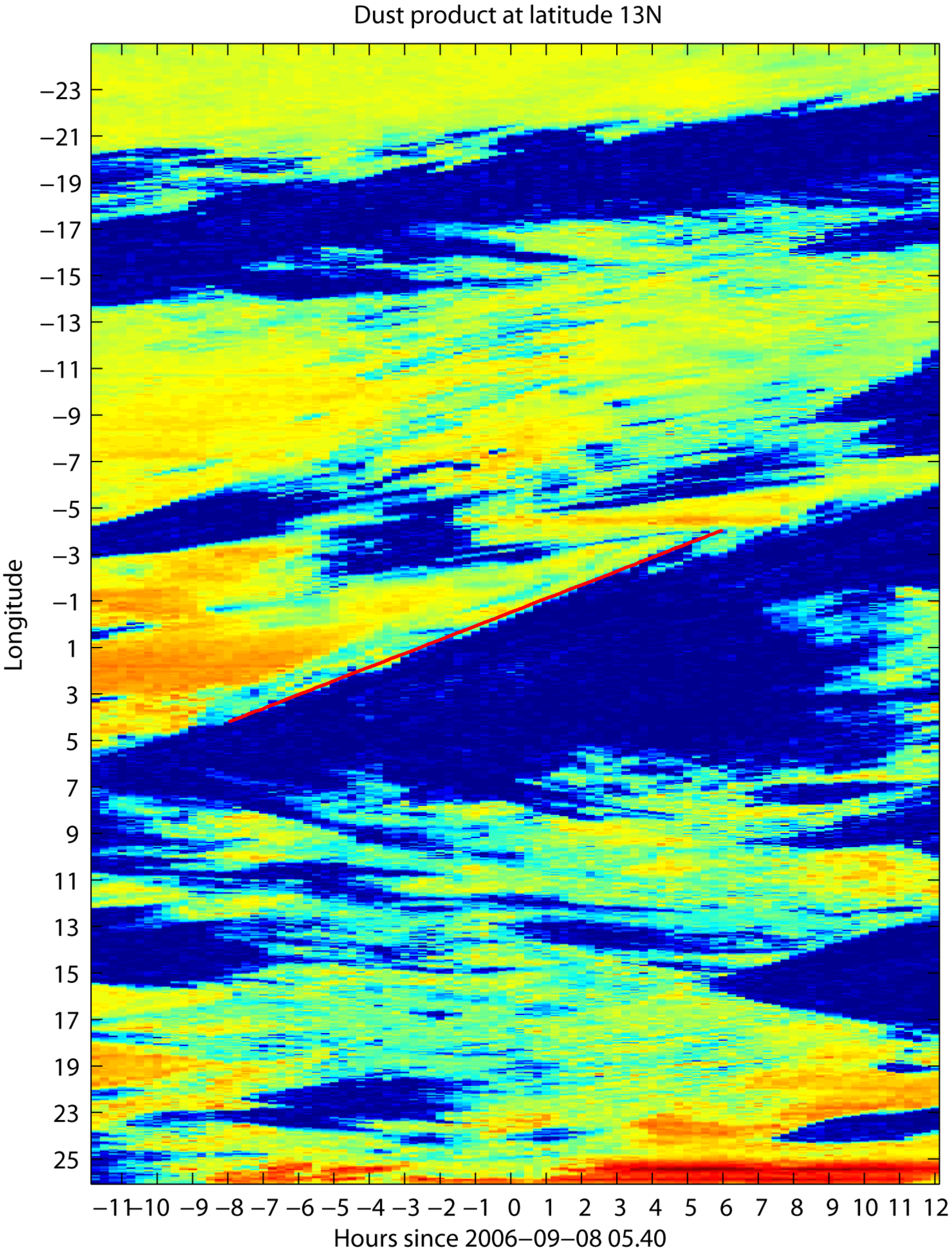

Figure 4-3: This false-colored version of the green channel of Figure 4-2 shows the stark contrast of the front edge, also detectable in individual SEVIRI dust product image frames. Some space-time variability is evident along the leading edge of the front.

4.4 Stripes in the lightning Hovmoller diagram

4.4.1 Automated Hovmoller analysis

Hovmoller diagrams plot a scalar field's value against time and one dimension of space and are helpful in meteorology for showing long-term phenomena where wave motion is suspected. The remaining dimensions of space not represented along one of the graphs's axes are typically represented by integration. A concrete example is shown in Figure 4-4: we integrate lightning flashes from 8N–18N (a 10 degree latitude region centered on Niamey) and plot every day against longitude. This plot shows squall line MCSs as bands of lightning moving from east to west over many days. Each "cell" in this graph is an integration over 1 hour of time and one degree of longitude. (We generally graph only five or six days at a time and increase our time resolution to fifteen minutes per cell when we do so.) The Matlab code to generate these diagrams is given in Appendix A.1.

We plot the logarithm of lightning strikes per "cell", a technique suggested by *Morales* (2010). Plotting a linear function of lightning strikes per cell results in muddy, hard-to-read images; plotting the logarithm of lightning strikes makes trends easier to see at the expense of making it difficult to check a specific numerical value — for example, values of 2000 and 3000 strikes per 15 minutes and per degree longitude are not readily distinguishable.

An especially interesting feature of these Hovmoller plots is the long, narrow stripes that represent squall lines, which we have quantified, characterized, and associated with the translation of squall lines (see Section 5.7). These stripes typically have fairly constant slope (representing speed) throughout their propagation across the continent; their duration is typically several days; and their extent is tens of degrees longitude. Occasionally a strong lightning storm spills into multiple Hovmoller cells, creating multiple possible "starts" or "ends"; at a time where lightning is active in multiple longitudes, we favor the westmost longitude for both "start" and "end" (this could represent the leading edge of a squall line), and at a longitude where lightning is active at multiple times we favor the earliest time for both "start" and

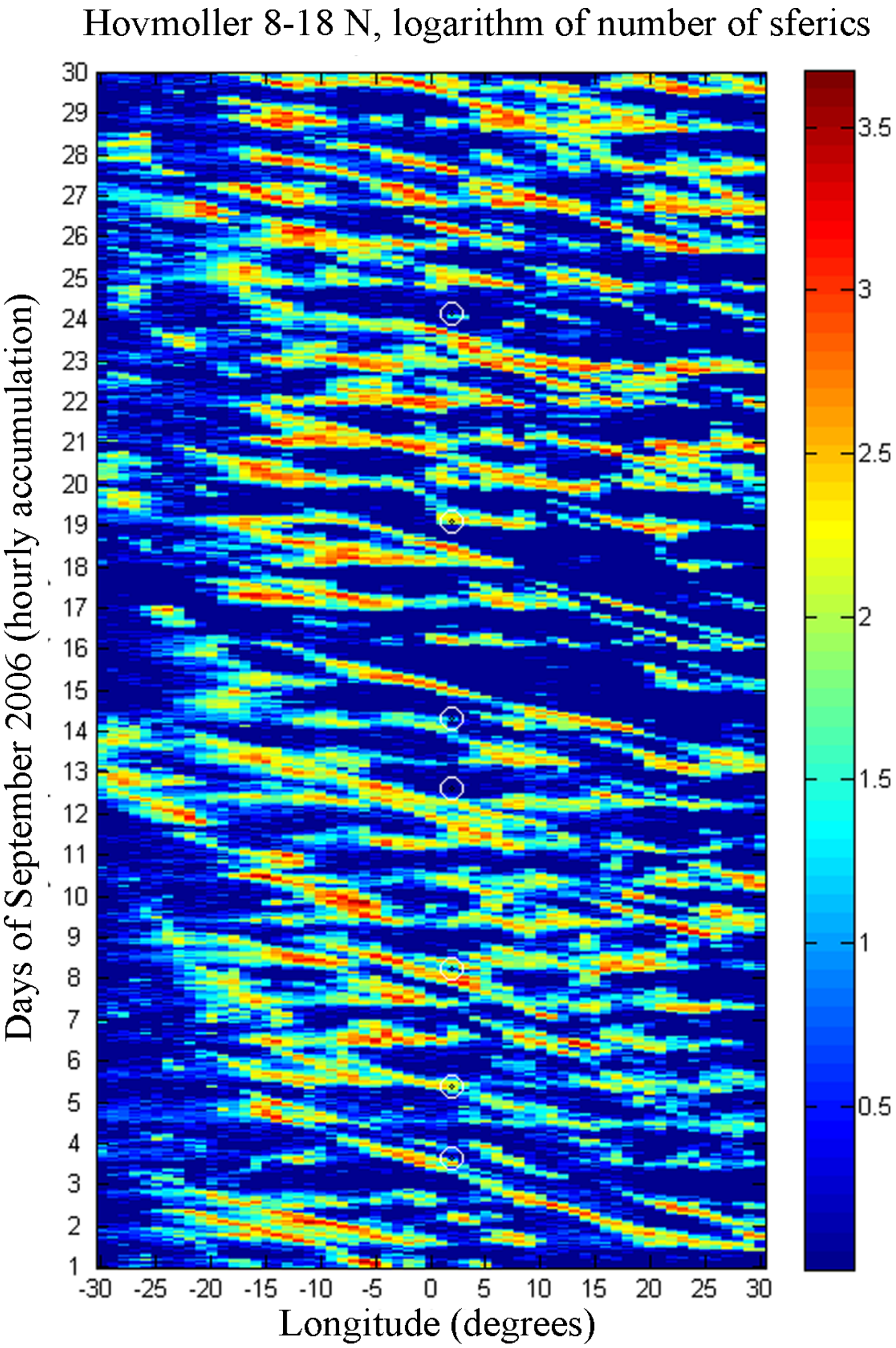

Figure 4-4: This lightning Hovmoller diagram shows lightning strikes for September 2006 integrated from 8-18 N latitude. Each distinct image cell has dimensions 1 degree longitude by 1 hour. Circled in white at 2 E longitude are the times when gust fronts were observed to cross the MIT radar at Niamey. A Hovmoller plot for August lightning activity is given in Figure 5-41.

"end" (a convention to make measurement consistent). Stripes sometimes include periods where there is little lightning activity; a stripe may include several segments separated by little or no lightning if the speed of each segment is nearly the same and the stripe exhibits continuity, such that there is no phase shift between the two segments.

A difference of a single cell in measuring distance represents 1 degree longitude (about 111 km); in measuring time it represents 15 minutes. The amount of error in our average speed calculations depends on the error in distance and time; for typical values of distance and time, an error of one "cell" in distance has an order of magnitude greater effect on speed than an error of one "cell" in time. For example, for a stripe with length 35 degrees longitude and duration 3 days, an error of 1 degree longitude would affect speed by about 0.4 m/s, and an error of 15 minutes would affect speed by about 0.05 m/s. We are measuring events along long lines, tens or hundreds of pixels in length, and so we likely encounter <1 pixel error.

4.5 Combining lightning maps and SEVIRI infrared dust images

To improve the utility of the lightning stripes, we annotated each available SEVIRI dust product image frame with dots representing ZEUS/STARNET lightning strikes (see Section 2.3), then made movies showing the progress of storms as viewed by the dust product and lightning simultaneously throughout August and September. SEVIRI dust product images are available every 15 minutes and were annotated with the lightning data from the nearest 15 minutes (so an image from 0000 UTC was annotated with data from 2352:30–0007:30 UTC).

SEVIRI dust product images use a geostationary projection which becomes less linear the further the image is from 0 N, 0 E. The difference between the geostationary satellite projection and an equirectangular projection (linear relationship between latitude / longitude and pixel value) is minimal at Niamey and near the equator, but above 20N it becomes especially noticeable. Although the SEVIRI image extends from 25W to 25E and 5S to 30N, at the top the image extends from (30.7 N, 30.3 W) to (30.7 N, 30.3 E), and at the bottom the image extends from (5.1 S, 25.1 W) to (5.1 S, 25.1 E). The equations that convert a latitude and longitude to a pixel value are straightforward and given in (*Wolf and Just*, 1999); Matlab code to perform the transformation is presented in Appendix A.2.

Integrating the SEVIRI dust product context with the lightning product made it possible to examine the dust and cloud context for lightning stripes, which provided useful validation that the stripes identified in Hovmoller diagrams represented a continuous system of MCS activity and not unrelated clusters of lightning activity whose phase and speed happened to coincide.

4.6 Counting lightning strokes with Lagrangian analysis

To get a quantitative measurement of how much lightning a storm contains, we use a Lagrangian technique that treats the lightning producing system as a “parcel” with a scalar quantity that can be measured over time (in this case, amount of lightning strikes). In West Africa during the summer, lightning-generating convection is often limited to a single squall line, so it is frequently possible to draw a box around the squall line’s entire extent inside of which most lightning strikes are associated with that event. By manual inspection of movies showing the SEVIRI dust product and the lightning superimposed, we developed boxes for most of the MCSs associated with squall lines that launched gust fronts crossing Niamey, and we measured the amount of lightning over time for each event. Sample code to generate these graphs is given in Appendix A. After producing these data, we report the number of lightning strikes per minute. We also report another quantity, lightning strikes per minute per unit length, when we have manually measured the extent of a squall line at a particular time. This metric, shown in Section 5.5, gives a rough measurement of the strength of the convection along a squall line that takes into account its extent.

Chapter 5

Results

This chapter presents several key results about about how gust fronts interact with MCSs and synoptic-scale events. First, a tabulation of all observed gust fronts and their characteristics is presented, and the data are shown to validate what is known about preferred times and locations for convective initiation. Then these data are used to produce an observational validation of the density-current model of gust front propagation. Gust fronts are shown to have satellite-determined mean propagation distance 750 km and frequently exceeding 1000 km, meaning that many events extend beyond the mesoscale to the synoptic scale.

Evidence for the conceptual model of gust front initiation from thunderstorm downbursts is shown with lightning-stroke Lagrangian data, validating our ability to count lightning strokes within a storm using the Lagrangian method. Finally, a remarkable phenomenon is shown in a Hovmoller diagram of lightning over Africa: long, continuous "stripes" of convection that last for thousands of kilometers and as long as five days are tabulated and their possible context, influence by gust fronts, and interaction with synoptic-scale activity is explored.

5.1 Gust front incidence, diurnal and seasonal variation

Table 5.1 shows our measurements for gust fronts crossing the MIT radar site: temperature drops and crossing times were available for all 40 events using ARM Mobile Facility data, and SEVIRI measurements were available for the 30 of those events. What features must an event have to be SEVIRI visible? It must have attained at least tens of kilometers in extent, since our SEVIRI images have resolution about 6 km/pixel and a single pixel of dust is unlikely to be detected. It must not be obscured by high-level cloud, normally not a problem for gust fronts which proceed out past trailing convection, but possibly an issue for detection if the gust front propagates beneath high cloud. Deep cumulonimbus clouds without convection are a common problem in satellite identification of convective cells (*Donovan et al.*, 2008). For additional measurements from surface stations, see Appendix B.

It may help prediction of gust fronts to know whether there are certain times a gust front is more likely to be launched. We would expect this to be similar to answering whether there are certain times of day an isolated storm is likely to be generated spontaneously (and ground observations do clearly show especially thunderstorm-prone times of day) or certain times of day a squall line is likely to spawn a gust front. For the purposes of diurnal variation, we can track two different quantities: the time a gust front is observed crossing Niamey (guided by ground and radar observations, then confirmed by visibility measurements validated with a sharp drop in surface temperature), and the time a gust front first becomes visible in satellite imagery. Neither tells the whole story about when gust fronts are launched: attempting to infer launch time from Niamey crossing times introduces error because gust fronts propagate at different speeds, from different locations, and for different amounts of time before they reach Niamey; while inferring satellite-observed launch times introduces a subjectively measured quantity based on a measurement (when a gust front is first satellite-visible) which is necessarily inaccurate for fronts that begin with size smaller than can be detected in satellite images. Gust fronts launched at the same

Date of GF radar site crossing (2006, UTC)	Temperature drop at ARM site (C)	Radar: 10-minute speed (m/s)	SEVIRI: observed duration (hr)	SEVIRI: observed propagation distance (km)	SEVIRI: average speed (m/s)
1 June 16:58	3.3	-	23	730	8.8
2 June 17:16	11.6	-	13	340	7.2
4 June 17:37	3.7	-	-	-	-
7 June 20:04	10.8	-	13	240	5.1
15 June 02:12	3.9	-	17	420	10.2
17 June 22:15	12.2	-	12	700	11.8
21 June 20:43	4.8	-	16	590	15.8
27 June 19:10	5.2	-	-	-	-
2 July 00:06	5	14.3	15	660	10.7
5 July 00:22	2.5	12.1	21	1180	12
6 July 23:13	4.4	12.6	15	930	13.3
9 July 00:07	4.4	11.4	-	-	-
10 July 16:40	6.4	-	16	600	15.8
11 July 18:45	3.2	11.6	7.6	160	19.1
12 July 18:43	3.6	-	12	240	21.7
14 July 05:12	7.1	21.3	18	760	12.8
15 July 04:04	2.9	-	23	1120	14.8
17 July 06:42	6.7	9.38	24	1360	13.7
19 July 05:13	3.9	19.4	12	840	22.4
20 July 18:38	3.6	-	-	-	-
22 July 09:43	5.7	18	4.3	320	19.6
25 July 07:02	2.6	12.6	-	-	-
31 July 09:24	3.2	14.2	8.5	670	16.8
3 Aug. 13:49	6.5	20.2	20	920	9.5
6 Aug. 08:00	2.2	12.4	-	-	-
11 Aug. 03:21	2.3	16.6	-	-	-
17 Aug. 09:56	2.6	-	17	920	14.8
18 Aug. 08:40	5.8	15.4	17	820	14.1
22 Aug. 03:19	3.2	-	24	1920	15.7
26 Aug. 14:39	8	12.7	21	1470	14.9
28 Aug. 02:28	6.5	16.6	24	1450	15.1
30 Aug. 07:34	3.2	15.2	8.4	290	7
3 Sept. 14:43	5.1	16.4	24	1280	17
5 Sept. 09:22	6.1	13.3	22	1090	17.2
8 Sept. 05:40	3.6	8.11	24	1350	6
12 Sept. 15:70	10.3	-	-	-	-
14 Sept. 07:32	4.3	-	16	860	5.6
19 Sept. 01:53	6.8	-	20	1060	20.5
24 Sept. 03:10	6.3	21.4	-	-	-
30 Sept. 08:28	2.9	-	-	-	-

Table 5.1: Gust fronts crossing the MIT radar site, June-September 2006

time of day equidistant from Niamey may arrive several hours apart if their speed varies. And the cloud cover inside squall lines and MCSs associated with a gust front may be unusually large on some days, making measurements on those days inaccurate. Niamey crossing times are ultimately based on ground station observations and are available for all 40 gust fronts, while we can measure SEVIRI-based origin information for only 30 of those events.

Nevertheless, the graphs show similar results: two peaks, one peak in late afternoon and a second smoother peak in the late evening or early morning. *Janiga et al.* (2009) found similar patterns in convection initiations plotted against time: a sharp diurnal peak around 1800 UTC comes from local convection in the Air Mountains, and a second smoother peak around 0500 UTC represents new convection initiated by long-lived MCSs as they approach Niamey. Our peaks (Figure 5-1) from Niamey crossings occur at 1900 UTC (sharp) and 0800 UTC (smooth), slightly later than those recorded by *Janiga et al.* (2009), but these peaks also represent a somewhat different phenomenon, a gust front which is a byproduct of convection and which has generally spent some time propagating before it reaches Niamey. (For a comparison of measured gust front and squall line speeds, see Figure 5-30.)

Our data for SEVIRI origins (figure 5-2), based on 30 cases where the origin time could be inferred from SEVIRI cross-section images, directly reflect the first time that a gust front is visible in SEVIRI dust product satellite imagery. This time is doubtless earlier than the “true” launch time of the gust front than the time the gust front reaches Niamey, but now instead of including undesired information about the time for a gust front to reach Niamey from its original launch location, our data exclude desired information about the time a gust front spends under cloud cover, where it is invisible to satellite sensors. Both Niamey crossing times and SEVIRI-determined origin times show a lull from 1200–1400 UTC (1 event at Niamey, 0 events recorded in SEVIRI), which suggests that those hours are especially unfavorable to both new convection and the maintenance of convection.

We would expect to see some seasonal variation in the number and strength of gust fronts crossing Niamey. Early in the summer, observers see stronger wind gusts and

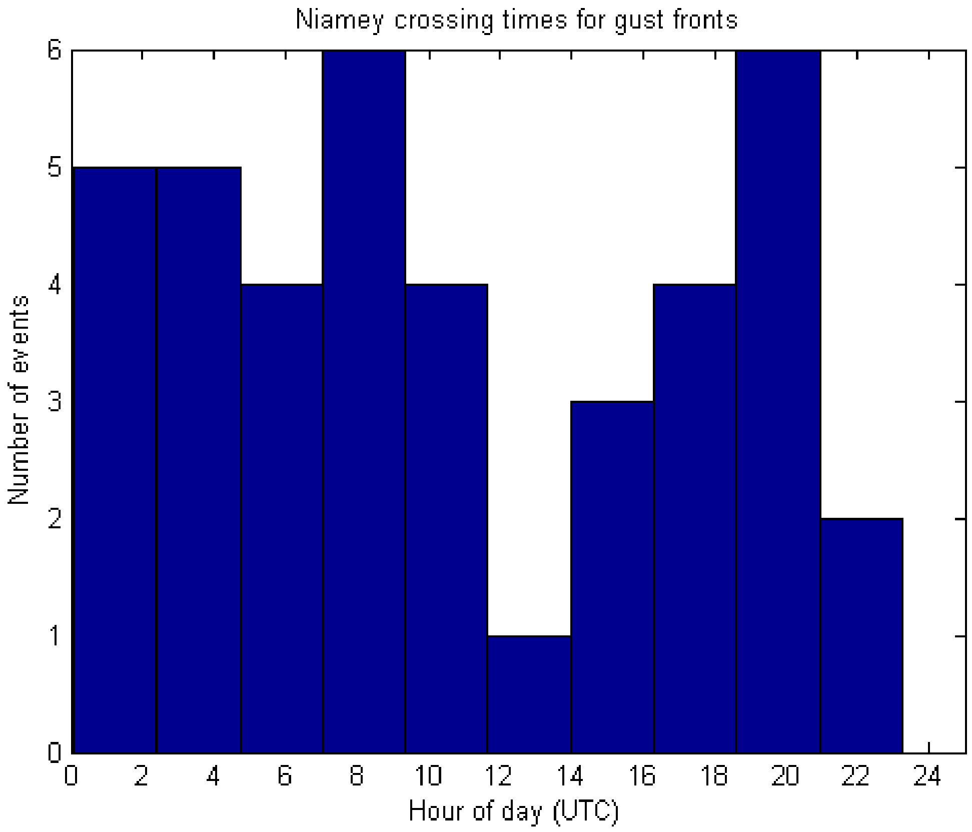

Figure 5-1: The diurnal variation of gust front crossing times at the Niamey radar site. (13.4915 N, 2.1698 E), with crossing times determined by ARM station measurements.

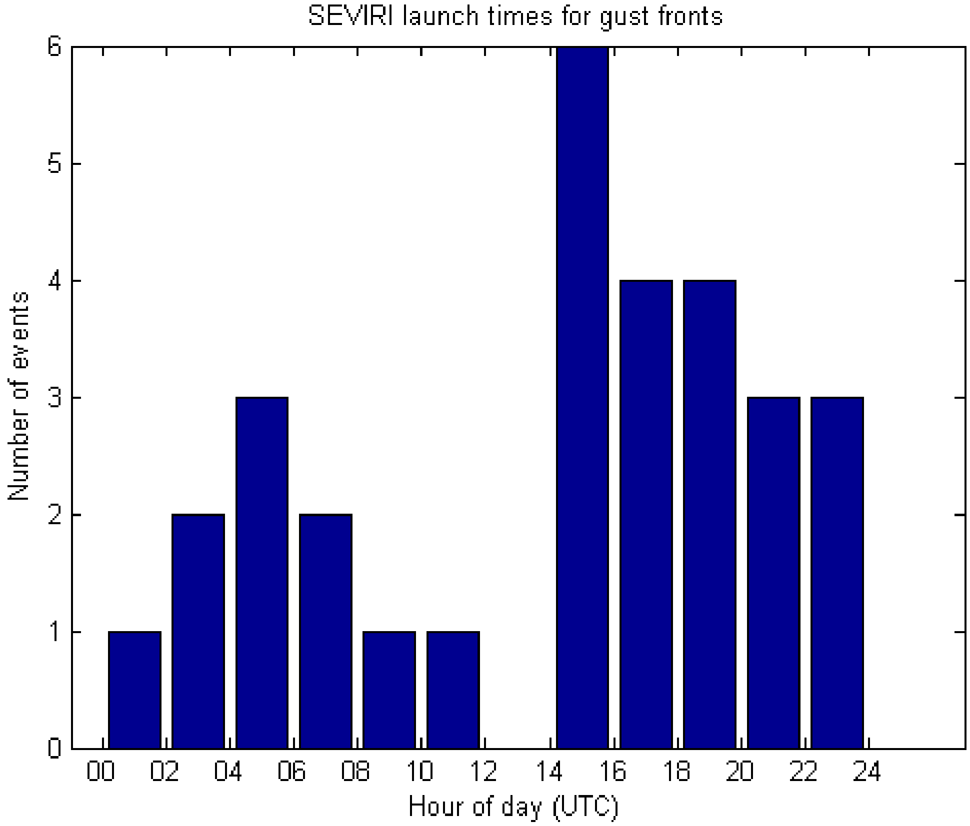

Figure 5-2: The diurnal variation of a gust front initiation times based on SEVIRI satellite observations of the first time a gust front became visible during summer 2006, for 30 different gust fronts.

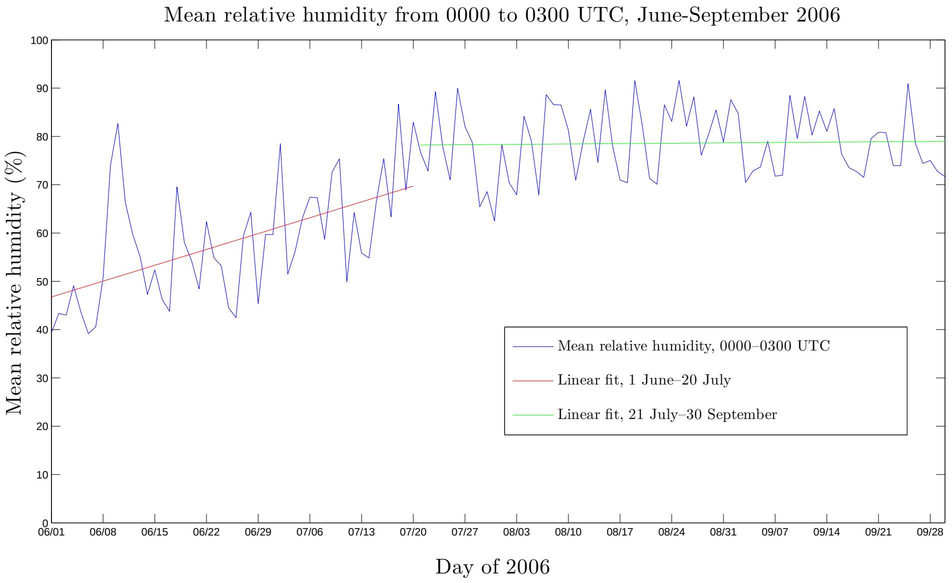

Figure 5-3: Mean relative humidity from 0000-0300 UTC as measured by the ARM surface station at Niamey. The first 50 days, from 1 June to 20 July, have linear least-squares fit y = 0.4687x + 46.3, with y in units of percentage relative humidity and x in units of days; this slope translates to about 3.3 percent relative humidity increase per week. The remaining days, from 21 July to 30 September, have linear least-squares fit y = 0.0109 + 77.7 — relative humidity remains close to 80% once it reaches that threshold.

drier air; after June, the monsoonal flow intensifies, rainfall becomes more frequent, and gust fronts are likely to loft less dust because the surface material is wet and packed instead of dry and loose. A plot of mean relative humidity, figure 5-3, shows how the surroundings become wetter as the season evolves. Yet the gust front data paint a more subtle picture: June, August, and September have about the same number of gust fronts observed to cross Niamey, while July has a spike with almost twice as many.

Figure 5-4, a plot of temperature drop versus time, records no strong trend — with linear correlation coefficient r = -.013 — but reveals that of the four events which yielded the highest temperature drops at Niamey, three were recorded in the first week of June. Our sampling period with the radar, which begins in July, may simply miss the dustiest, gustiest days; perhaps most of those were in June, May, or April. If the rainy season has any effect on the strength of gust fronts, it could be that only a small amount of moisture is sufficient to prevent most high-intensity

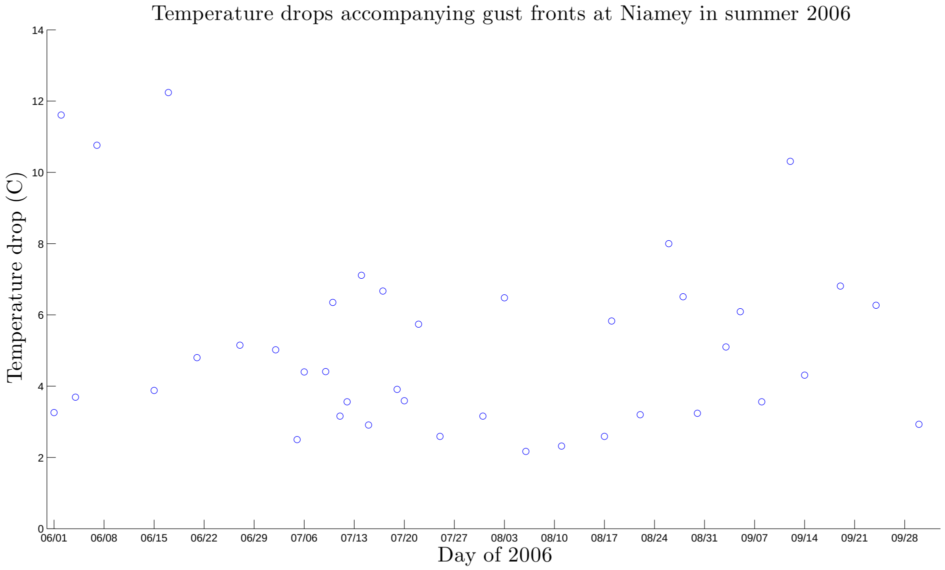

Figure 5-4: The abrupt drops in surface-level air temperature associated with gust fronts that crossed the ARM Mobile Facility at Niamey, Niger from June-September 2006.

haboobs.

By the numbers, radar-measured 10-minute instantaneous speed (Figure 5-5) likewise shows little stronger trend — with linear correlation coefficient r = 0.17 — and manual examination of the plot shows no clear trend. It is likely that both speed and temperature drop change over a gust front's lifespan, since we have seen fronts which slow down and stop moving altogether late in their propagation, and we show in Section 5.4.3 that speed and temperature drop are linked. We have relatively few data (only 22 points for speed), not enough for us to ignore the contributions of diurnal influences or the influence of front age on individual data points when considering the seasonal variation.

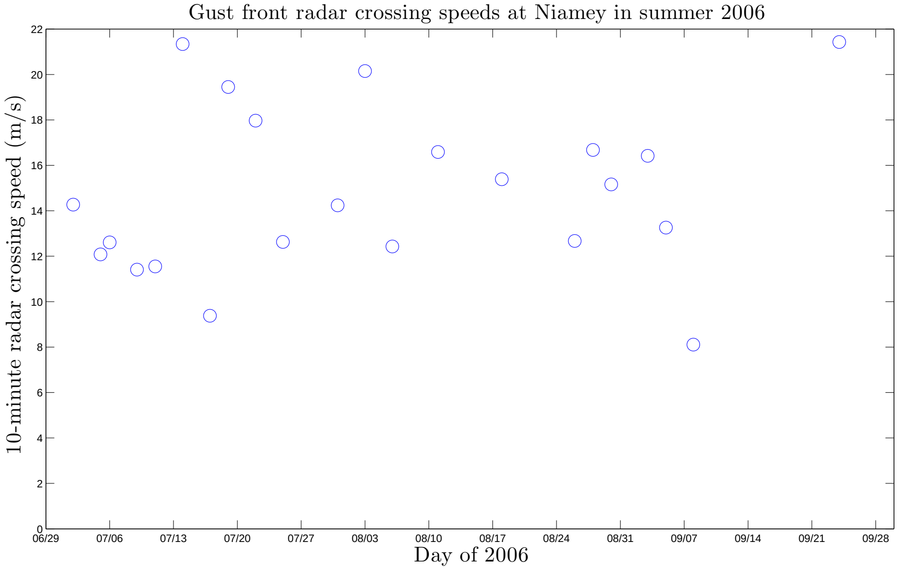

Figure 5-5: The 10-minute crossing speeds recorded at the Niamey site for gust fronts that crossed from June-September 2006.

5.2 Gust front visibility minima

Not all events caused equal drops in visibility when they crossed the MIT radar; that is to say, not all gust fronts were equally dusty, or more precisely, the amount of airborne particular matter that maximally occluded a horizontal visibility sensor, creating a minimum in visibility, at the ARM Mobile Facility varied during various different gust fronts. Recorded horizontal 1-minute visibility dropped below 2 km for most fronts (Figure 5-6); the lowest visibility recorded was 29 m on 17 June, while the maximum sensor recording was 11.5 km on 17 August[1], and a distribution of 1-minute visibility is given in Figure 5-7, and the mean was 2.4 km. Over the 10-minute time scale, most events still recorded less than 2 km visibility (see Figures 5-9 and 5-10, but the minimum visibility was higher (48 m, 17 June), the maximum was higher (20 km on 15 July and 17 August), and the mean was 6.5 km. The lowest-visibility events tended to occur earlier in the season — see Figures 5-8 and 5-11 for plots of 1-minute and 10-minute visibility versus time, which show that the moderately dusty events ($>$ 10 km 10-minute visibility) all occur in July or later.

---

[1] The visibility sensor records 20 km maximum (in the presence of no dust at all.)

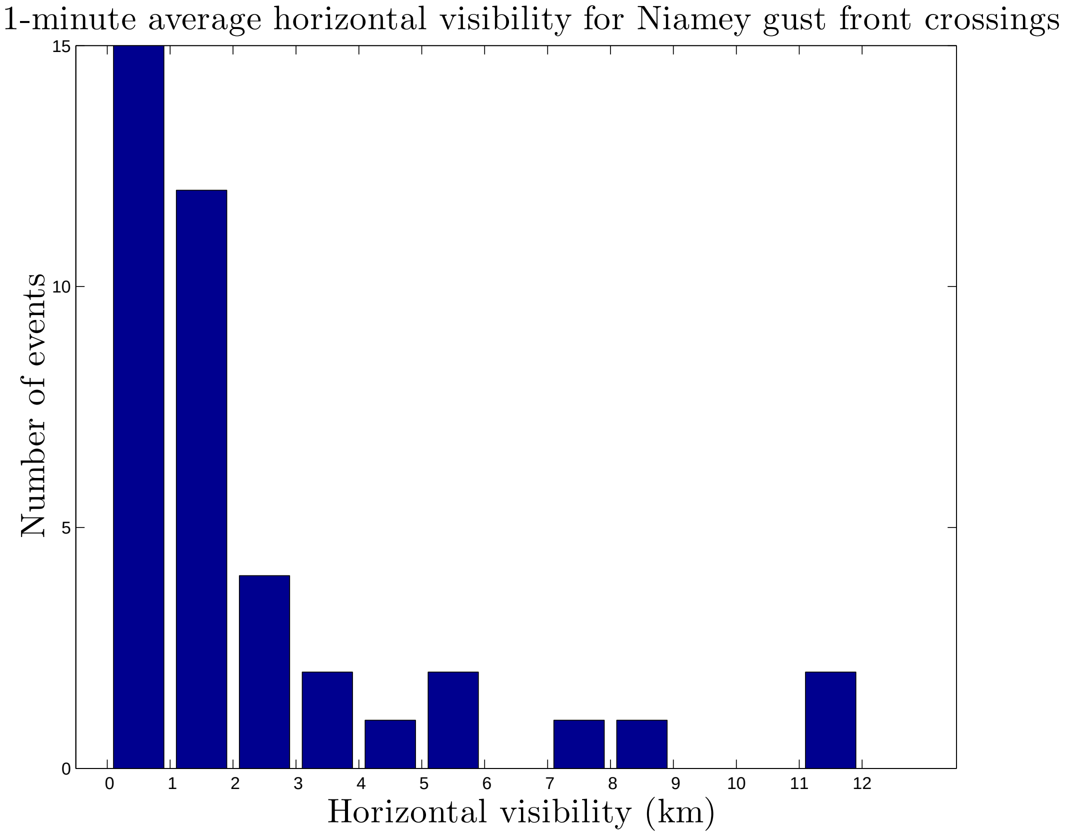

Figure 5-6: The distribution of 1-minute minimum visibility measured at the Niamey ARM Mobile Facility site as gust fronts crossed Niamey in summer 2006.

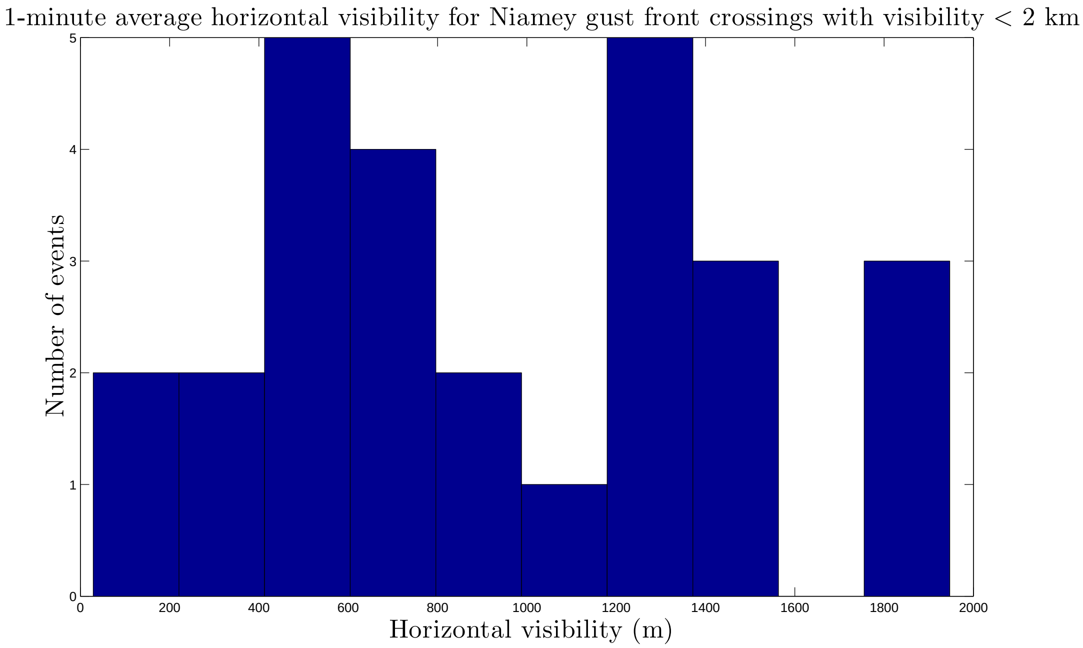

Figure 5-7: The distribution of 1-minute minimum visibility measured at the Niamey ARM Mobile Facility site as gust fronts crossed Niamey in summer 2006, showing only visibility measurements below 2 km.

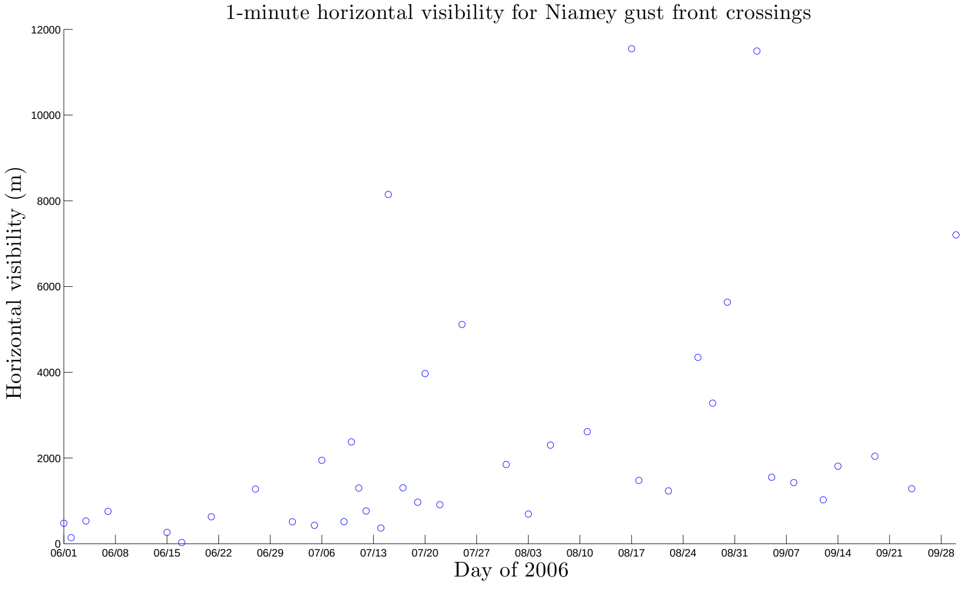

Figure 5-8: The distribution over time of 1-minute minimum visibility measured at the Niamey ARM Mobile Facility site as gust fronts crossed Niamey in summer 2006.

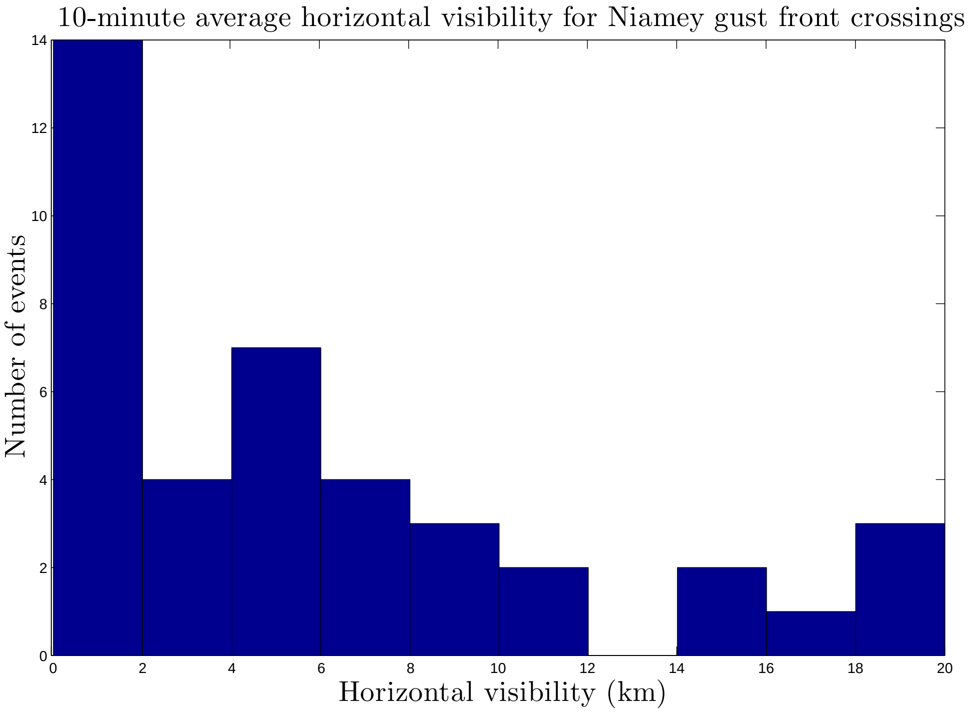

Figure 5-9: The distribution of 10-minute minimum visibility measured at the Niamey ARM Mobile Facility site as gust fronts crossed Niamey in summer 2006.

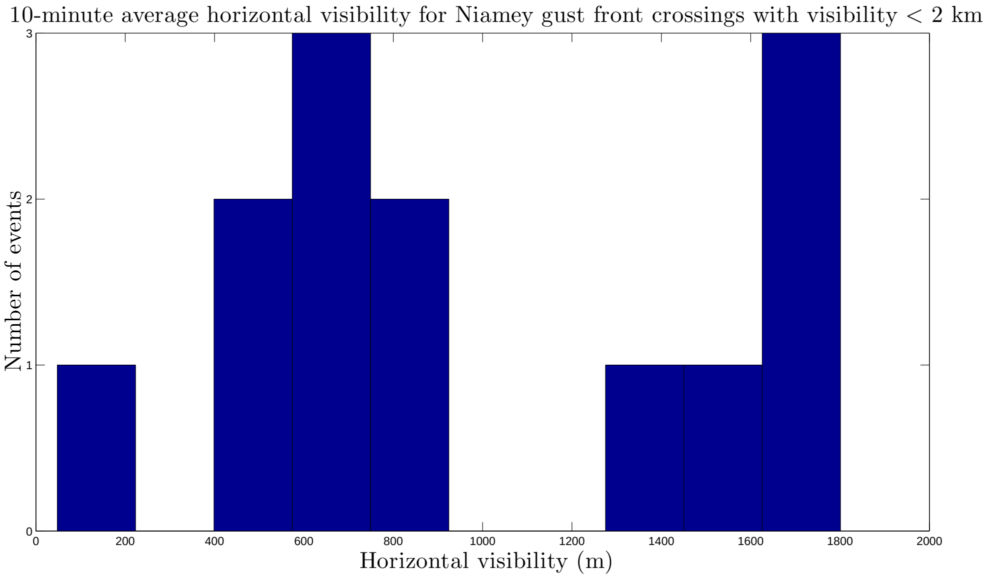

Figure 5-10: The distribution of 10-minute minimum visibility measured at the Niamey ARM Mobile Facility site as gust fronts crossed Niamey in summer 2006, limited to events with visibility < 2 km.

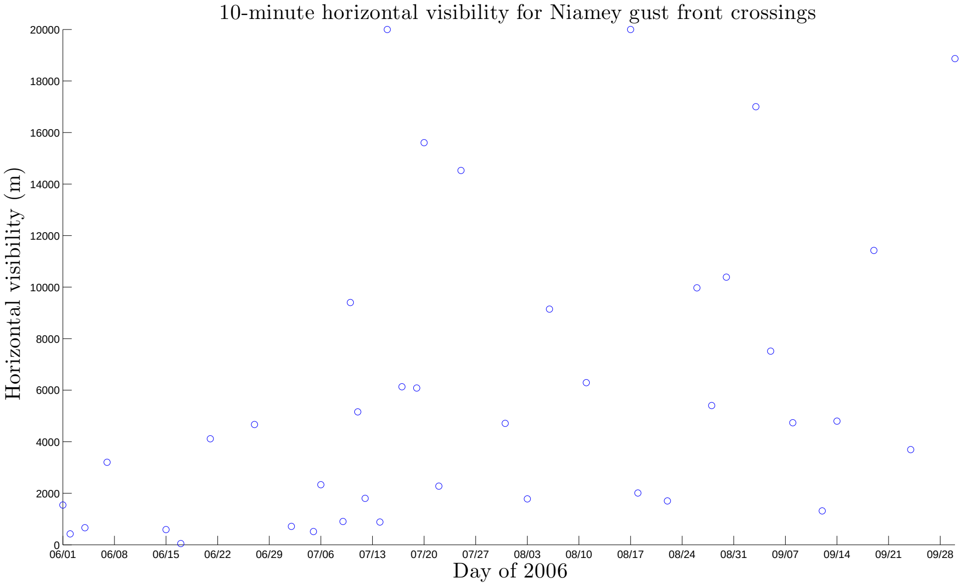

Figure 5-11: The distribution over time of 10-minute minimum visibility measured at the Niamey ARM Mobile Facility site as gust fronts crossed Niamey in summer 2006.

5.3 Geographical origins of gust fronts

Just as certain locations are favorable to convection, we would also expect to see that certain locations are favorable to gust front initiation. The same analysis of satellite imagery which produced origin times was also used to produce origin locations (Figure 5-12), and the results show a cluster of initiations near the Air Mountains northeast of Niamey. These match the findings of *Janiga et al.* (2009), which located a nexus of new convection in the Air Mountains as the origin for many MCSs which reached Niamey. Moderately sized multicell thunderstorms often form as new convection or along a squall line near mountain ranges, where updrafts are common and can initiate new convection.

Because satellite-inferred origins are ill-defined in the presence of high cloud, we would prefer to have another way to measure the beginning points for gust fronts. If we assume that gust fronts are launched near the beginning of the mature phase of a thunderstorm, our lightning stripes provide a viable alternative way to locate the origin of convection that we can then validate as the origin of a gust front using the SEVIRI dust product. We can measure the longitude of origin of the lightning stripes, and the time when lightning strongly surges (a stripe begins) will be closely correlated with convective initiation. Our measurements (Figure 5-13) show a distinct peak between 20 E and 30 E longitude, which supports the finding of *Laing et al.* (2008) that certain locations are preferred for convection. *Mekonnen et al.* (2006) have argued that this particular maximum reflects the geographical influence of the Darfur highlands and is a strong contributor to new storms.

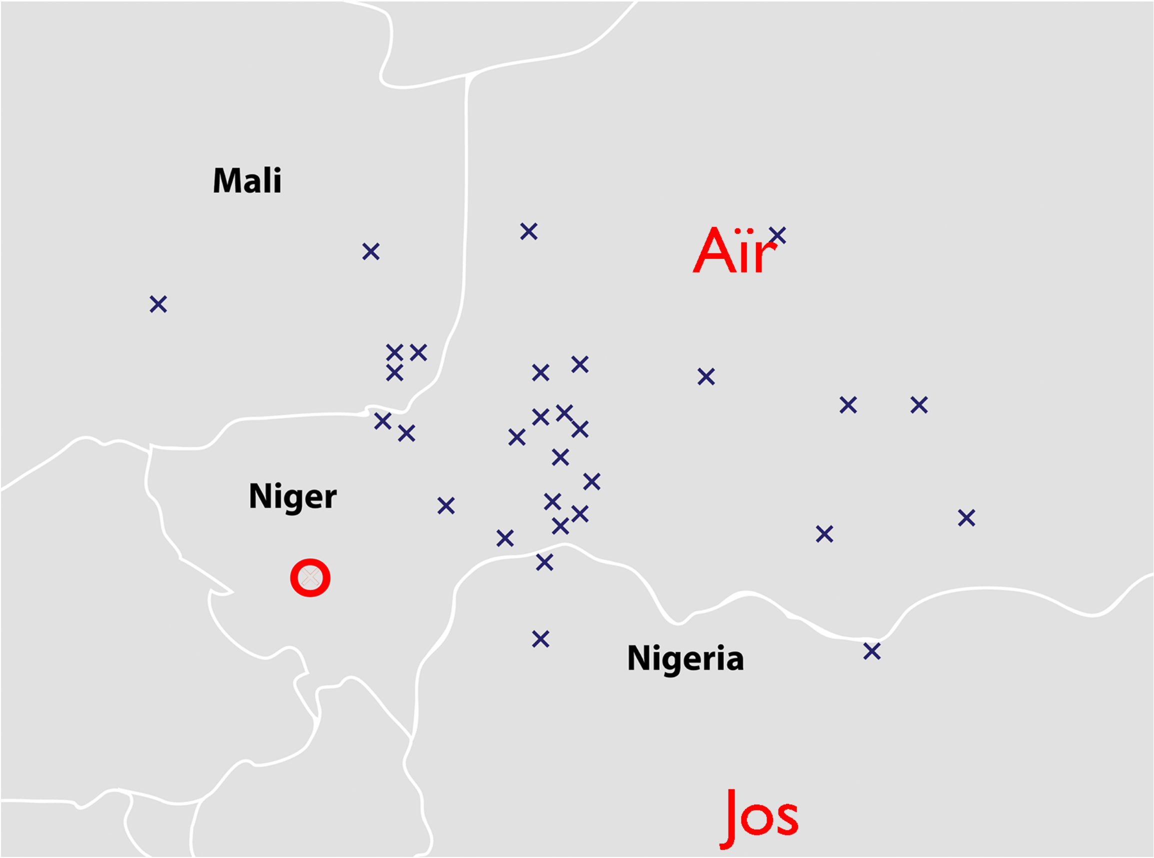

Figure 5-12: The locations at which gust fronts first became visible in SEVIRI dust product imagery, overlaid on a political map of West Africa. The radar site is shown as the red circle at Niamey, Niger. The label "Air" marks the southernmost point of the Air Mountains, a region of high convective initiation, near Agadez; the label "Jos" marks the highest point of the Jos Plateau, a region which in some studies has been a significant source of convection.

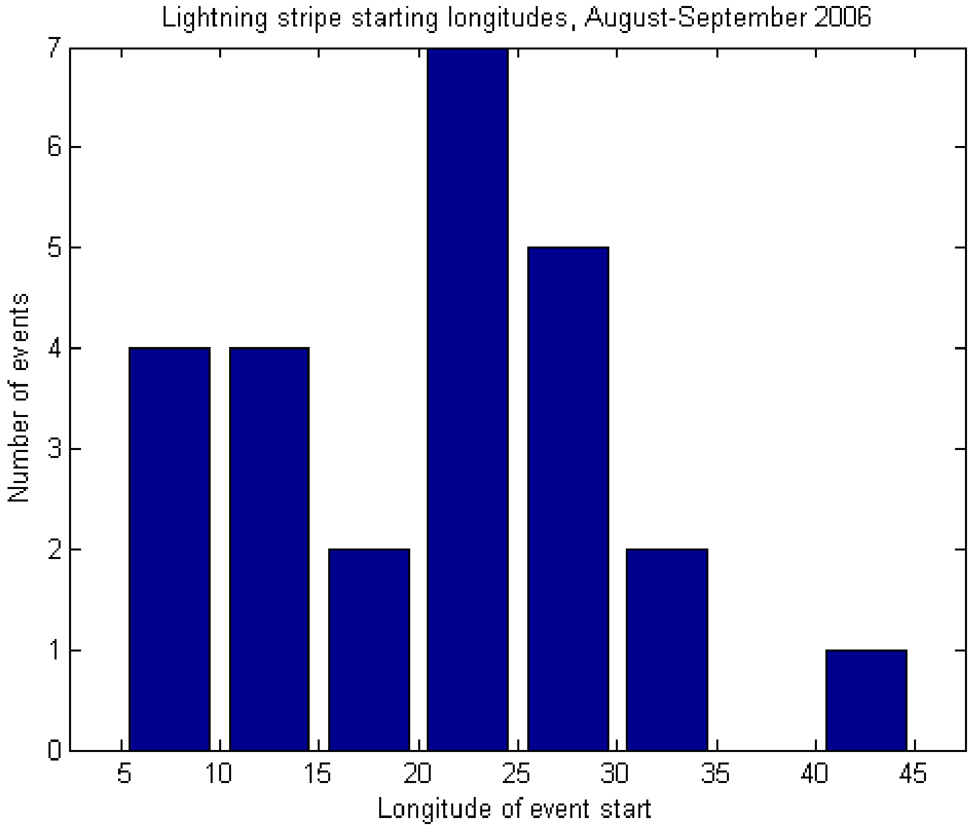

Figure 5-13: The longitudes at which lightning stripes were first recorded.

5.4 Gust front taxonomy: 1D SL vs. 2D isolated

While SEVIRI images provide good estimates of GF lifespan for short-lived, isolated events, one encounters difficulty measuring gust fronts which form along a large squall line but are not fast enough to out-pace that squall line's mid- and upper-level cloud activity. Our approach is likely to underestimate the age and extent of gust fronts formed from large systems. Still, it gives much larger values for average GF extent than could be previously measured using weather radar alone (see Section 5.6).

5.4.1 1D vs 2D events

There is a qualitative difference in the radar profile of a gust front generated from an isolated thunderstorm compared with one generated along a squall line. The first appears to be a circular, two-dimensional outflow that propagated in every direction; the second is detected only as a thin line in front of the squall line and is mostly one-dimensional. We present a taxonomy for these one-dimensional and two-dimensional storms based on radar and satellite observations. Qualitatively, the two-dimensional circular outflows travel faster, but do not propagate as far as their one-dimensional counterparts.

Two-dimensional outflows come from a point source, a thunderstorm which is (at least at the time it generates a gust front) isolated. These outflows from isolated thunderstorms are visible on average at least once a day in the SEVIRI dust product for West Africa during summer 2006 and were not uncommon at Niamey, where they represented 8 of the 30 SEVIRI-detectable gust fronts. They typically propagate for only a few hundred kilometers and only a few hours before they become impossible to see in the SEVIRI dust product. (See Section 5.4.2 for more on these cases.) But we have a paucity of radar data for these outflows against which we can test the density-current model: 5 of the circular outflows arrived at Niamey in June 2006, when the radar was not operational, and 2 were on days in July which are missing in our radar surveillance scans.

That leaves only the event on 11 July, which was typical in every way in ARM

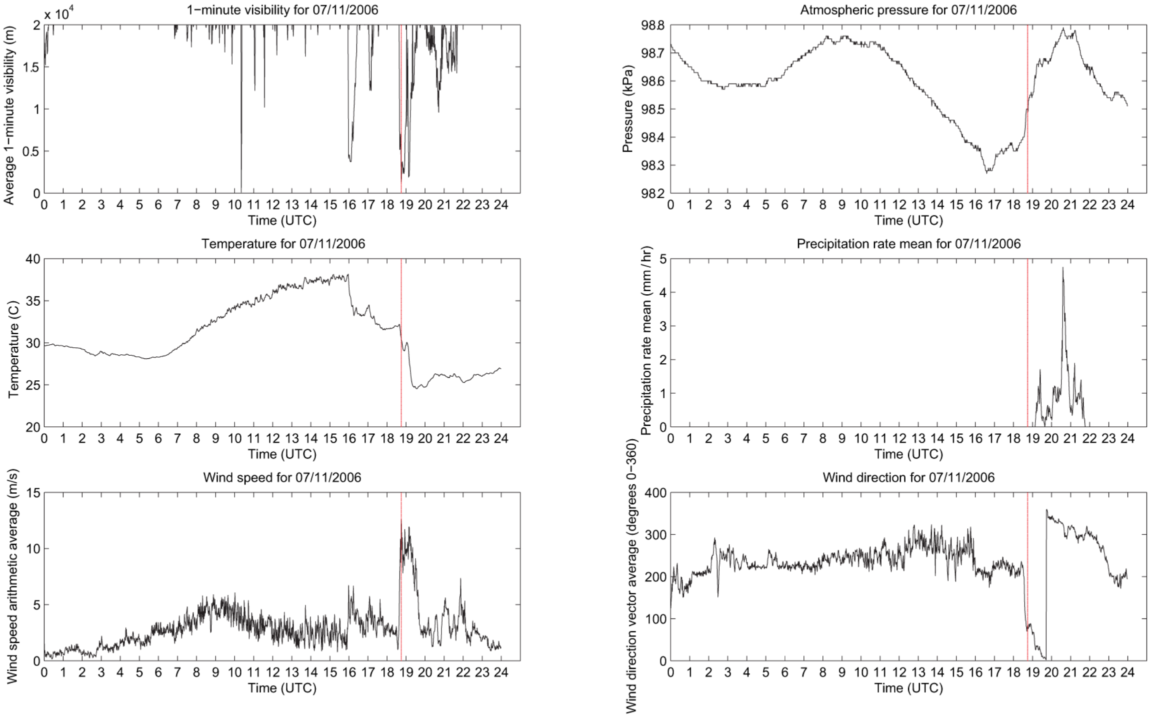

Figure 5-14: ARM surface station data for 11 July 2006 show a typical visibility drop, temperature drop, wind speed spike, pressure rise, and wind shift, followed by rainfall.

Mobile Facility surface station data (Figure 5-14). The 11 July event was measured by *Lothon et al.* (2010) but it made no impression on the SEVIRI dust product; events of this magnitude may be important but only detectable by radar or surface station measurements.

The radar does occasionally record gust fronts not accompanied by a squall line, for example on 3 September 2006, which might have originated from a squall line or which might have been formed by a smaller storm. See Figure 5-15 for the gust front's radar signature.

In one case, a gust front identified by *Lothon et al.* (2010) that originated around 1700 UTC on 10 July 2006 appeared as a circular outflow in the MIT radar's volume scans (Figure 5-16) and was visible for several hours in those radar images. That event was also visible, although at a very small scale, in SEVIRI dust product imagery (Figure 5-17).

In the absence of radar data, surface observations may miss the crossing of weak

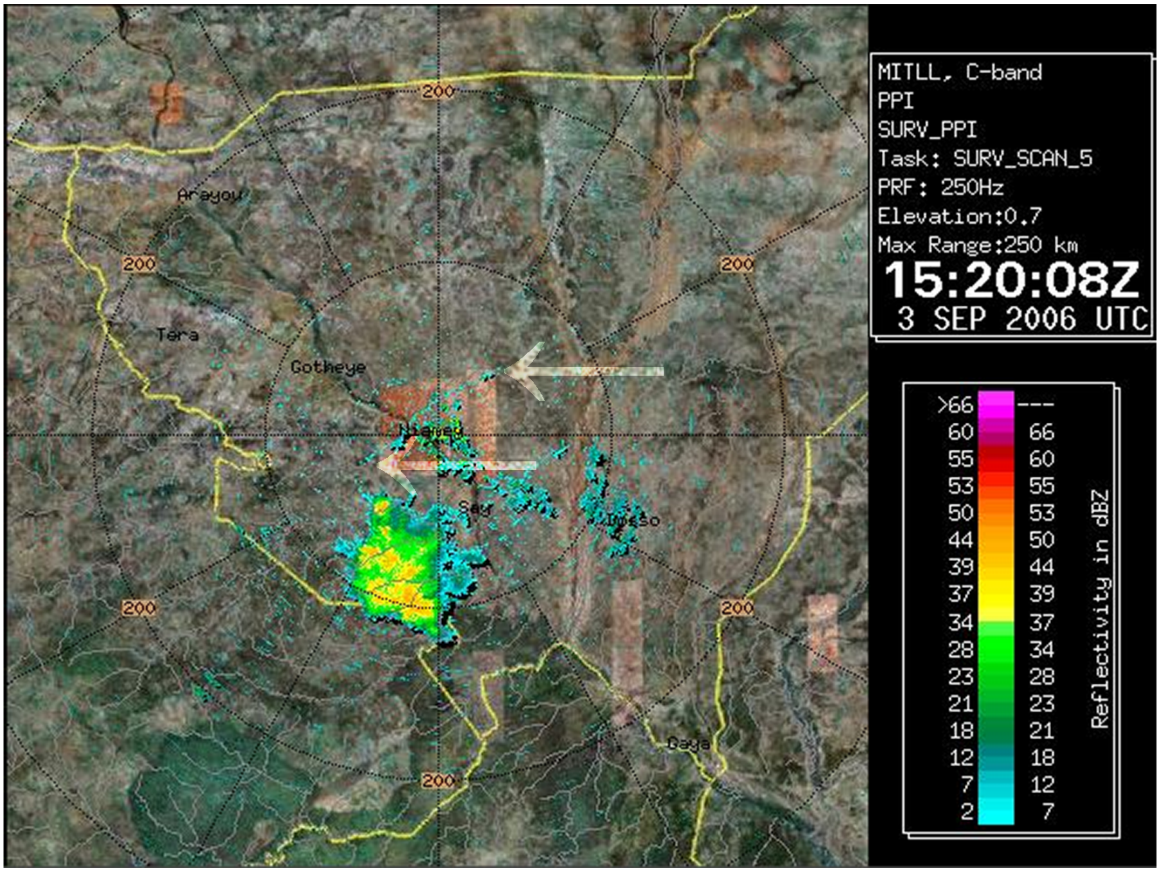

Figure 5-15: This radar surveillance scan shows a gust front as a thin line next to the radar site and just barely detectable. Arrows overlaid on the scan point to the top right and bottom left portions of the detected front. The front proceeded northwest and was not accompanied by a squall line; a small region of convection was detected behind the gust front. The gust front was first detected on the radar at 1440 UTC and no longer detectable at 1750 UTC.

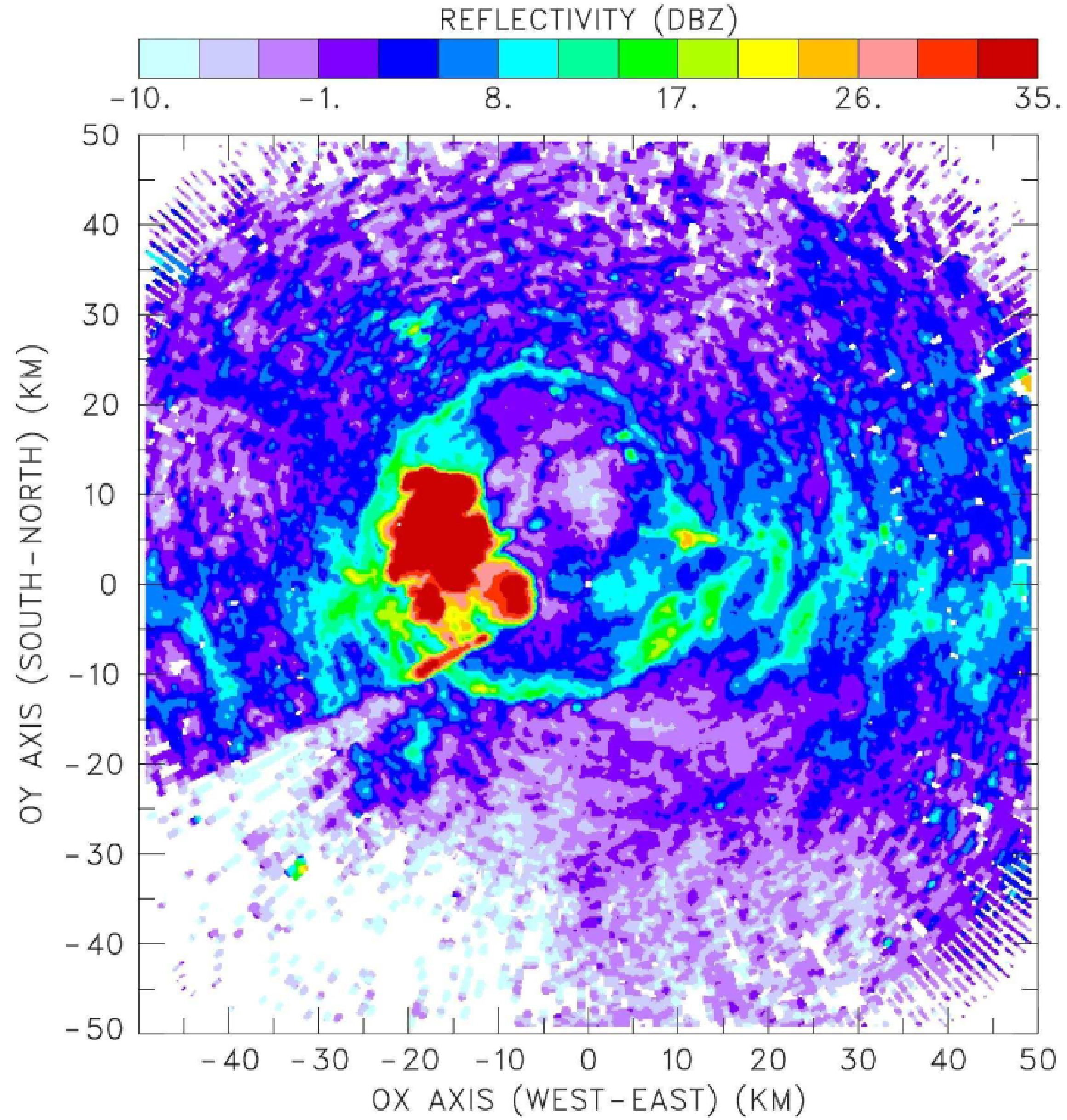

Figure 5-16: Reflectivity in plan view interpolated in vertical cross-section at Y=5 km, at 1700 UTC on 10 July 2006, a figure from *Lothon et al.* (2010), shows a circular outflow propagating away from the radar site.

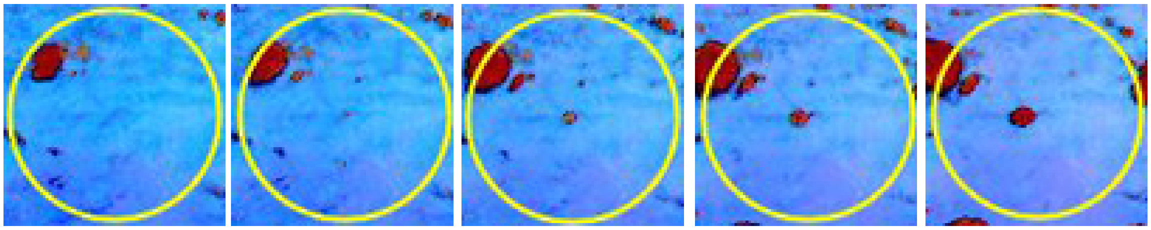

Figure 5-17: The SEVIRI satellite infrared dust product image, trimmed to a 250 km-radius circle surrounding the MIT radar site, on 10 July 2006, shows the satellite infrared context for the radar-recorded outflow of *Lothon et al.* (2010) From left to right, the times shown are 1600, 1630, 1700, 1730, 1800 UTC. The feature detected within this storm is primarily "thick high-level cloud", per the interpretation key in Figure 2-5. The 10 July case had 1-minute minimum horizontal visibility of 2.4 km and was one of only a few events with visibility > 2 km, so it was not among the strongest haboobs of the summer, but it did loft at least dilute amounts of dust. Despite the dusty nature of this front, no dust is detected in the SEVIRI image during the front's first two hours.

gust fronts. Table B.1, which presents detailed measurements of gust fronts from ARM Mobile Facility instruments, includes one event which was not recorded in our original tabulation of gust fronts, a gust front which crossed Niamey on 23 June 2006, according to visibility data. The gust front is only very moderately dusty (minimum visibility about 8 km) and contains only a small temperature gradient (1 C), but it can be detected faintly by manual review of SEVIRI image frames. SEVIRI imagery shows the event launched from an MCS at 8 E, 10 N at 1400 UTC on 22 June (the MCS itself launched in the Air Mountains at 1200 UTC on 22 June), and propagating almost imperceptibly for a day. At 1600 UTC on 23 June, after the event has crossed the MIT radar site, a strong band of new convection forms along the arc of the gust front, showing that even weak gust fronts can contribute to the organization of new convection. The event is last detectable at 0800 UTC on 24 June at about 3 W, 15 N; it propagates about 1300 km over about 42 hours.

5.4.2 2D events: more details

By direct observation of the SEVIRI dust product's cloud activity, we determined that 8 of the 30 SEVIRI-detected gust fronts originated from circular outflows rather than squall lines. See Table 5.2 for a summary of these events. The 8 gust fronts originating from circular outflows had mean propagation distance 480 km and mean observed duration 14 hr. The other 22 gust fronts, observed originating from squall lines, had mean propagation distance 990 km and mean duration 18 hr. Gust fronts can also originate from synoptic-scale events, as in 3-5 August 2006 (*Bou Karam et al.*, 2010).

The SEVIRI time cross-sections for the isolated events give us more information about gust fronts from squall lines compared with events from isolated thunderstorms. They do not differ much in average speed: the mean speed of the isolated events is 13.2 m/s compared with 13.8 m/s for the rest, a difference of less than five percent (see Figure 5-18). There are insufficient data to compare their instant radar crossing speeds: the radar was inoperative throughout June (five events), and of the remaining three events, radar data are only available for July 11. No outflows from isolated thunderstorms were observed to cross Niamey after July 12, suggesting that as the rainy season picks up, all the recorded gust fronts which reach Niamey originate from squall lines.

Perhaps squall lines are so common in late July and August and September that observers did not notice gust fronts from isolated outflows, or perhaps isolated outflows that reach Niamey are less common in the rainy months for a physical reason. The dominance of squall lines in generating gust fronts over Niamey suggests that baroclinic conditions (with a strong latitudinal temperature gradient reflecting favorable conditions for squall line formation) were more prevalent than baroclinic conditions (when a weak temperature gradient favors the formation of many isolated thunderstorms).

It is no surprise that gust fronts from isolated thunderstorms are measurably less persistent than those generated by squall lines: in SEVIRI product imagery, the total

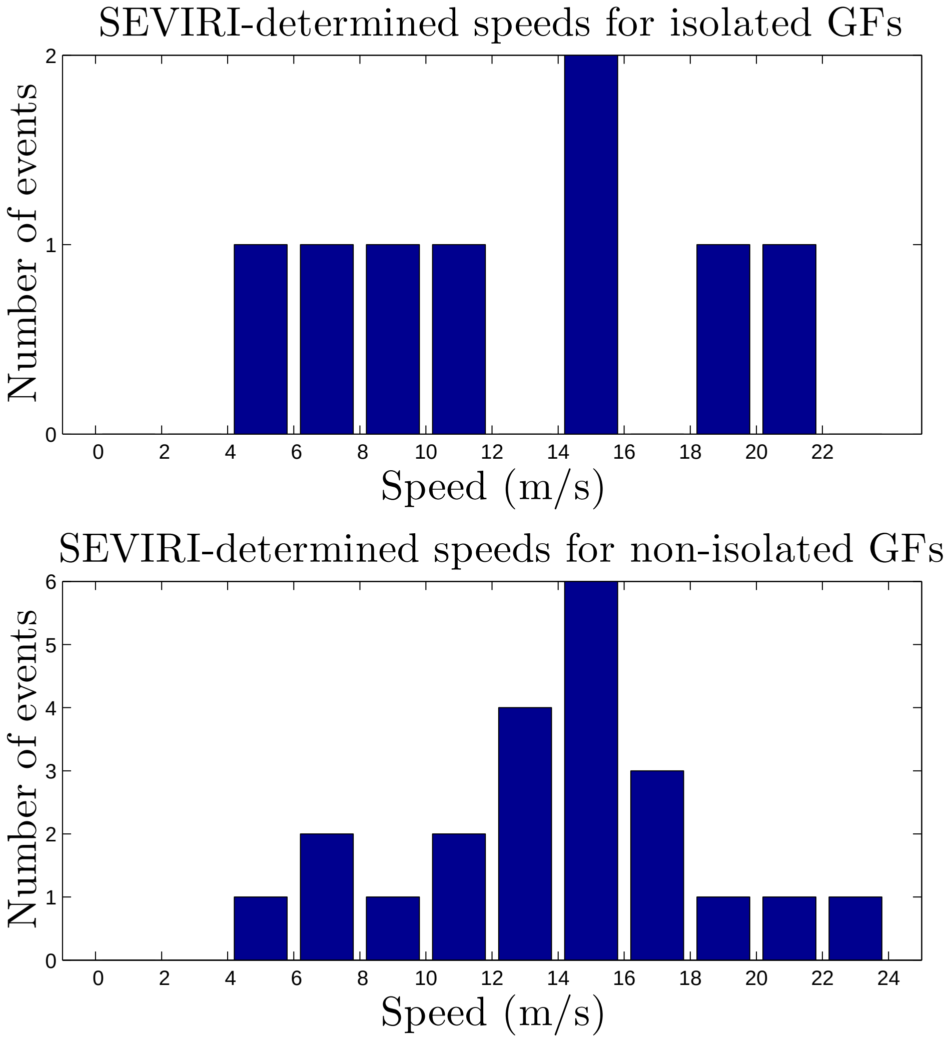

Figure 5-18: Average speeds determined with the SEVIRI cross-section method for gust fronts from isolated thunderstorms and for gust fronts generated from squall lines share the same mean; only 8 isolated events were recorded compared with 32 non-isolated events, precluding detailed statistical comparisons of these speeds.

Niamey crossing time	Event description	Duration (hr)
11 July 18:45	outflow directly over the radar	7.6
17 June 22:15	outflow northeast of Niamey at about 5E	11.5
12 July 18:43	outflow about 150 km southeast of the radar within the radar (surveillance scan unavailable)	12.1
7 June 20:04	multiple outflows occur directly over the radar site at 19:00	13.1
2 June 17:16	multiple outflows about 150 km due east of Niamey	13.3
10 July 16:40	outflow occurs directly above Niamey radar site (surveillance scan unavailable, but see figure 5-16)	15.6
21 June 20:43	outflow east of Niamey at about 5E combines with another gust front from a larger squall line	16.1
1 June 16:58	Outflow due east of Niamey at about 6E, combines with multiple outflows and propagates west	23

Table 5.2: Gust fronts originating from isolated outflows, June-September 2006

time that events were observed to propagate (shown as duration in Table 5.2) was 14 hours for the isolated gust fronts, compared with 18 hours for the other events. The isolated events propagated about half as far (mean 450 km versus mean 990 km for the others).

In SEVIRI product imagery, isolated gust fronts were detected for less time on average than gust fronts launched from squall lines (mean 14 hours for the 8 isolated events versus 18 hours for the rest) and they propagated about half as far (mean 450 km versus mean 990 km).

5.4.3 Gust front speeds

If gust fronts have the dynamic characteristics of a density current, as proposed in the model of *Wakimoto* (1982) (see Section 3.2), then we should expect to see that gust fronts with larger temperature drops travel faster. We validated the model using our radar and surface station measurements of speed and temperature, which represent point measurements at a single location and time along fronts that may be hundreds of kilometers long. (See Section 4.1.1 for details on the process we used.) Wakimoto gives a simple equation relating the propagation speed of the leading edge of a density current to physical parameters:

$V = k(gd(\rho_w - \rho_c)/\rho_c)^{1/2}$

V is the velocity. The height of the "head" of cold air within the gust front, d, can vary widely during the gust front's lifespan and is difficult to measure using surface instruments. Photographs often show a head at 1–2 km, and the height of a gust front observed by satellite lidar (see Section 2.6) was about 2 km (*Bou Karam et al.*, 2010). As an approximation in the face of uncertainty, we use d=2000 m for all calculations. The constant g is acceleration due to gravity (9.81 m/s). The densities ρ_w and ρ_c are the mean density of warm and cold air respectively, calculated using the ideal gas law as $\rho =$ p/RT, where p is absolute pressure (taken as a constant 1015 millibar, the mean of observations at the site), R is the specific gas constant for dry air (287.05 J/kg/K), and T is the temperature in Kelvin. The constant k, internal Froude number, is a dimensionless parameter that has been measured experimentally and in laboratory settings. Our observational test, shown in Figure 5-19, yields a best fit k value of 0.81, a close match to the density-current measurements *Wakimoto* (1982) cites with $k = 0.75$ from an observational study (*Benjamin*, 1968) and $k = 0.78$ from an earlier study (*Wakimoto*, 1982, pg. 1080).

The 11 July event, previously noted as a radar-measured isolated gust front, fits almost exactly on the best-fit line predicted by the density-current model, based on that event's temperature drop of 3.2 C and radar crossing speed of 12 m/s.

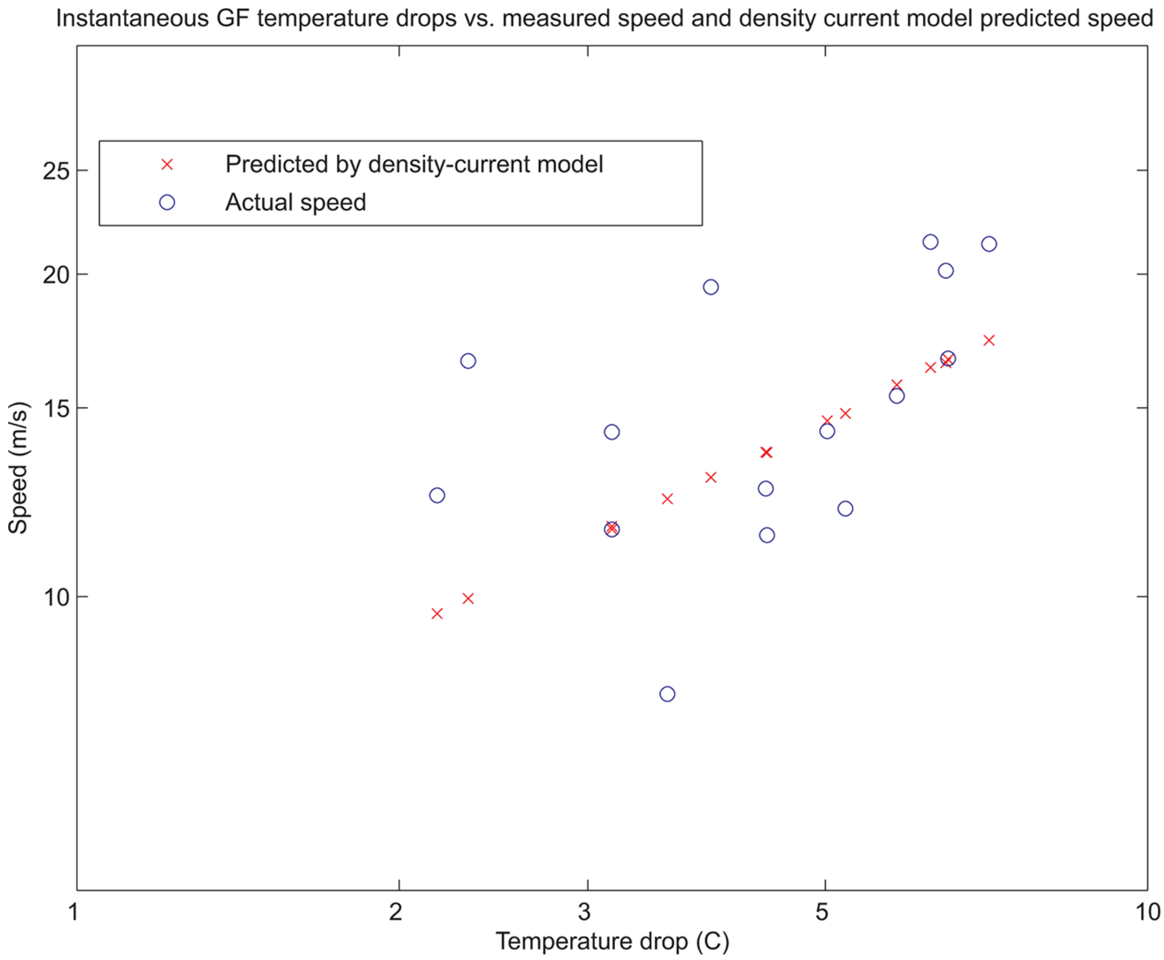

Figure 5-19: These radar-determined speed and ARM site-measured temperature drop data, plotted on a log-log scale, show how observations match with the best-fit predictions of the density-current model for gust front propagation. Some of the difference between predictions and observations comes from our use of a constant gust front head height d=2000 m; reasonable measurements of head height are 1–2 km.

5.5 The Lagrangian method for squall line lightning stroke counts

Of the 32 gust fronts associated with a squall line, 17 crossed Niamey in August or September, the months during which we have lightning data that can be used to characterize squall lines.

Counting lightning strokes provides a simple observational test for the traditional model of gust front launch; we would expect to see gust fronts following the peak of lightning activity associated with a microburst.

The ability to count lightning strokes is also important to forecasting: *Price et al.* (2007) has suggested a connection between lightning in East Africa and hurricane activity leaving the continent, citing the differences between the strong 2005 hurricane season (28 named Atlantic tropical storms and hurricanes) and the relatively weak 2006 hurricane season (10 named Atlantic tropical storms and hurricanes), which had nearly the same number of African Easterly waves (30 in 2005, 28 in 2006). In both seasons, about 70% of Atlantic AEWs were preceded by intense East African lightning, and in both seasons, 86% of named tropical cyclones and hurricanes were associated with intense East African lightning; the key difference between the two seasons was that the 2005 season had about 30% more East African lightning strokes and about 50% more total African lightning strokes.

Figure 5-20 shows the peak lightning based on Lagrangian measurements of lightning histories for each MCS that launched a gust front that crossed Niamey where the start and stop times of the MCS could be clearly located, the GF launch could be inferred from SEVIRI imagery, and the lightning's activity could be easily isolated from that of other nearby storms (for more on this technique, see Section 4.6). Table 5.5 gives details about the lightning counts for each case where it was possible to isolate the lightning activity.

Among the Lagrangian lightning histories for 16 events, 12 of them (75%) had a clear peak of lightning activity associated with a gust front's observed launch time. The mean offset between the lightning peak and the gust front's observed launch

MCS start	MCS age (hr)	MCS start long,lat	MCS end long,lat	MCS mean speed	GF launch time	Peak offset (hr)	Peak flashes per minute	Peak extent	Peak flashes per minute per 10 m
8/2 1515	47	15,20	-10,10	18	8/2 1730	0.5	13	290	3.6
8/5 1130	34	10,20	-8,10	19	8/5 2100	n/a	47	370	10.6
8/9 1245	75	17,10	-15,20	14	8/10 1600	-0.5	230	920	25.5
8/16 1100	28	10,20	-3,12	17	8/16 1245	n/a	20	550	7.0
8/17 1030	63	13,10	-20,20	17	8/17 1545	1	73	670	11.0
8/21 1315	54	10,17	-10,12	12	8/21 1715	-1.5	110	840	13.5
8/25 1430	43	13,17	-12,7	20	8/26 1000	0	40	540	7.4
8/27 0730	55	13,7	-15,18	17	8/27 1445	0	110	580	19.4
8/27 0715	108	25,17	-20,7	13	8/29 1700	-1	210	840	24.7
9/3 0315	28	7,12	-10,20	21	9/3 1445	0.5	13	480	2.8
9/4 1030	51	15,22	-15,17	18	9/4 1515	-0.5	9.3	270	3.4
9/7 1430	43	12,20	-13,13	19	9/7 1615	n/a	20	350	5.6
9/12 0230	55	12,10	-20,22	19	9/12 0715	n/a	20	310	6.4
9/13 1415	35	13,15	-5,22	17	9/14 0000	2	3.3	250	1.3
9/18 1400	46	7,10	-12,20	15	9/18 1745	-1	130	590	21.5
9/23 1415	36	10,22	-10,15	18	9/23 1745	1	37	440	8.3

Table 5.3: Lagrangian lightning measurements for MCSs, summer 2006. All times are UTC.
A positive peak offset means that the gust front was launched that many hours after a lightning peak.
Offset "n/a" means that there was no clear link between a lightning peak and a GF launch;
the maximum lightning within 4 hours of the GF launch time is still shown for these events.
We measure linear lightning strength as peak lightning flashes per minute / extent in km * 100,
or peak lightning flashes per 10 m.

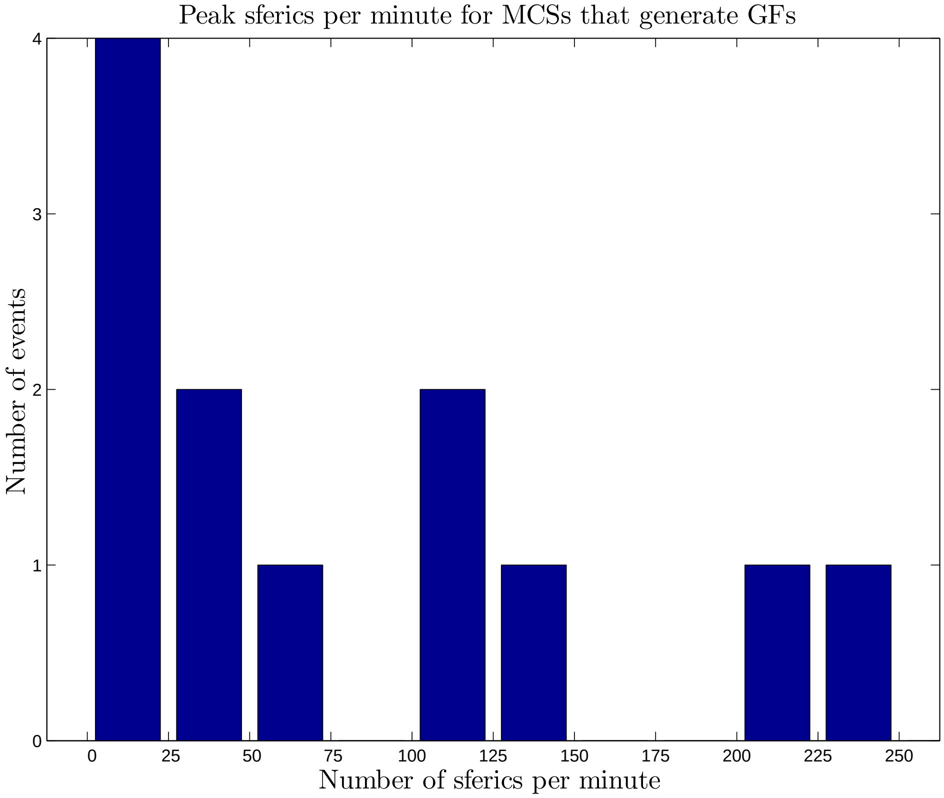

Figure 5-20: Distribution of peak lightning rates for MCSs which launched gust fronts whose origin could be traced to an MCS visible in SEVIRI dust product and lightning data, for MCSs which could be "boxed" and their lightning flash rates measured. Events for which there was no clear link between a peak in lightning activity and a gust front launch are not shown.

was about 0, although times vary from the peak arriving 1.5 hours later to the peak arriving 2 hours before launch time, showing the imprecision of SEVIRI-estimated gust front launch times. The absolute strength of the lightning (number of sferics per minute) varies widely from 3 sferics per minute to 230 sferics per minute (mean 68 sferics per minute). A more fundamental unit of "lightning strength" for a storm might take into account the length of the squall line being measured; we tried this metric by manually measuring squall line extent at the moment peak lightning was recorded and creating a metric with units of lightning strokes per minute per km, then multiplying by 100 so the metric ranges from 1–26. The distribution of this metric is shown in Figure 5-21. The highest value of 26 strokes per minute per 10 m extent is obtained on 10 August 2006 at 1630 UTC and reflects the contributions of a long, strong squall line (see Figure 5-22 for SEVIRI dust and lightning context) which the Lagrangian method has not completely isolated from nearby convection.

Figure 5-23 shows a strong positive correlation between our lightning stroke per minute per unit length metric and the length of a squall line at the time when the lightning stroke peak is recorded; longer stripes have more lightning per unit length. The linear correlation coefficient is r = 0.83. This observation is evidence that bigger storms, which have longer squall lines, are accompanied by deeper, more electrically active convective cells (cells with higher cloud top heights): storms with greater lateral development also have greater vertical development.

One case which shows no apparent correlation between the timing of any lightning peak and a gust front launch, August 16, is shown in Figure 5-24. Manual inspection of the SEVIRI-with-lightning image data does show the qualitative signature we expect to see (Figure 5-25), with an MCS initiating, beginning a cluster of lightning, and generating a gust front, but the quantitative signature we expect and see in every other case is not there. That signature may be small compared with the rest of the storm's lightning activity, or it may have occurred more than 1.75 hours before the inferred gust front launch time (this particular plot begins only 1.75 hours ahead).

A typical Lagrangian history for an event where gust front launch correlates with a clear lightning spike is given in Figure 5-26, for an MCS that began on 3 September

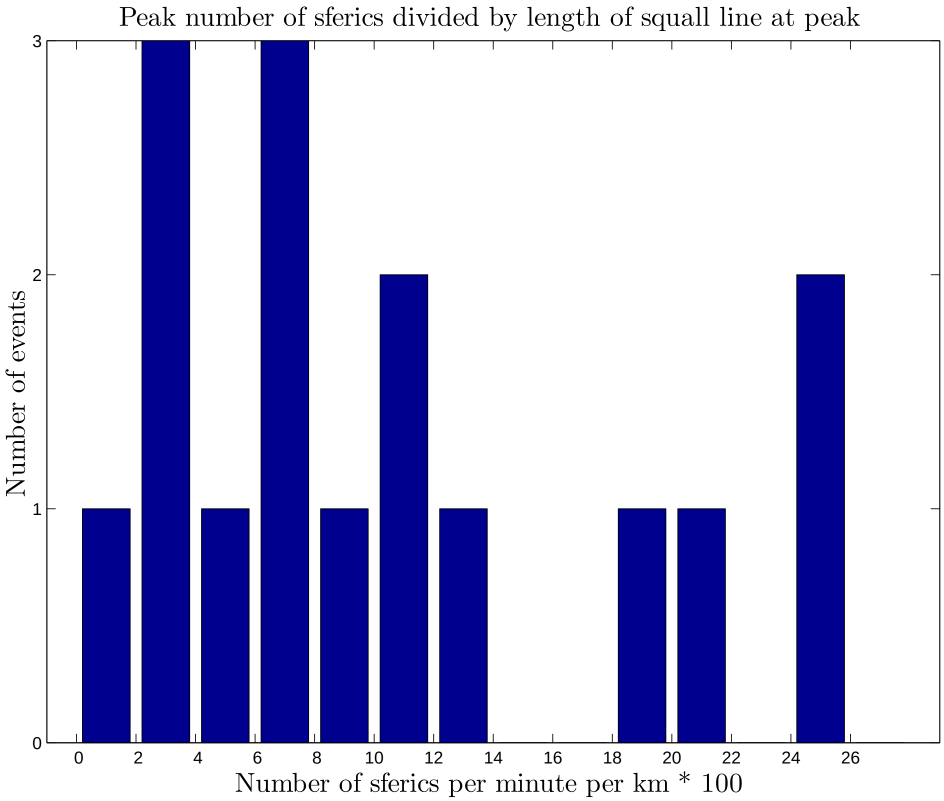

Figure 5-21: Distribution of peak lightning per minute per km * 100 for MCSs which launched gust fronts whose origin could be traced to an MCS visible in SEVIRI dust product and lightning data, for MCSs which could be “boxed” and their lightning flash rates measured. Extent was determined by manual measurement in SEVIRI imagery at the time of peak lightning activity near a gust front launch. Events are shown only if there is a clear link in SEVIRI imagery between a lightning peak and a gust front launch.

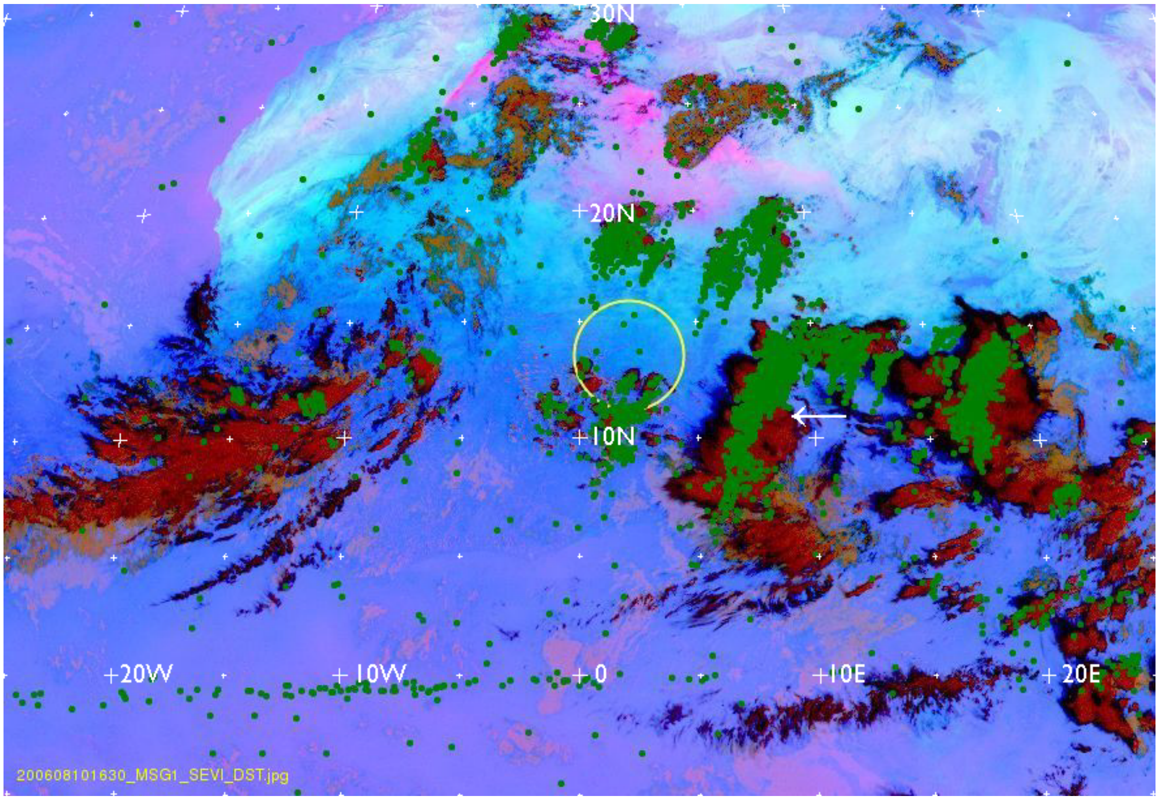

Figure 5-22: SEVIRI infrared dust imagery with lightning strokes overlaid for 10 August 1630 UTC, the time of peak lightning associated with a gust front launch (inferred at 1600 UTC) and with the highest measured number of lightning strokes per minute per extent. Part of the high amount of lightning (this event is the highest point of the distribution in Figure 5-21) comes from unrelated events between 15 N at 20 N, which are unfortunately included in Lagrangian calculations for this MCS because portions of the lightning associated with this MCS eventually propagate as far north as 20 N.

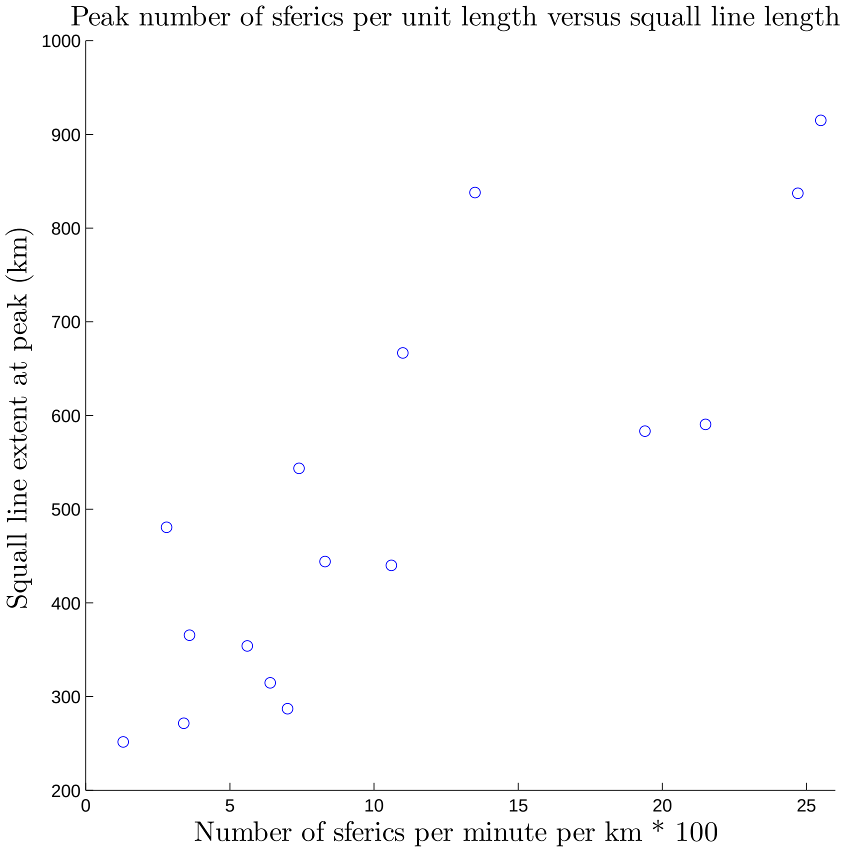

Figure 5-23: Lightning strokes per minute per unit length, as measured in Table 5.5, show a strong positive correlation with the length of the squall line at the time of the peak lightning measurement.

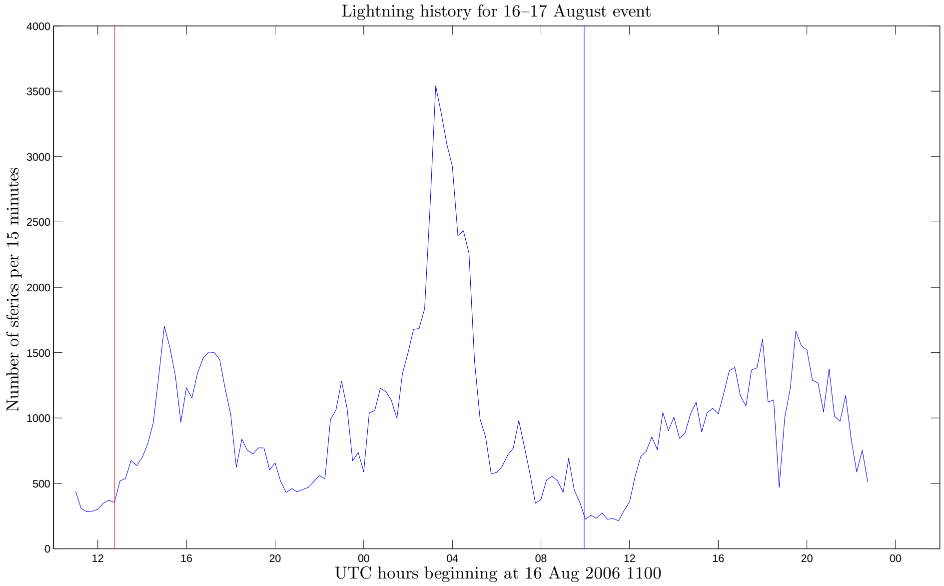

Figure 5-24: The Lagrangian lightning count from 16 August 2006, 1100 UTC to 17 August 2006, 1500 UTC, with a gust front launch inferred at 16 August 1245 UTC (red line), bounded by longitude 3 W to 10 E and latitude 12 N to 20 N. The gust front reached Niamey on 17 August 0957 UTC (blue line). This is an unusual case where the gust front launch does not follow an apparent spike in lightning activity.

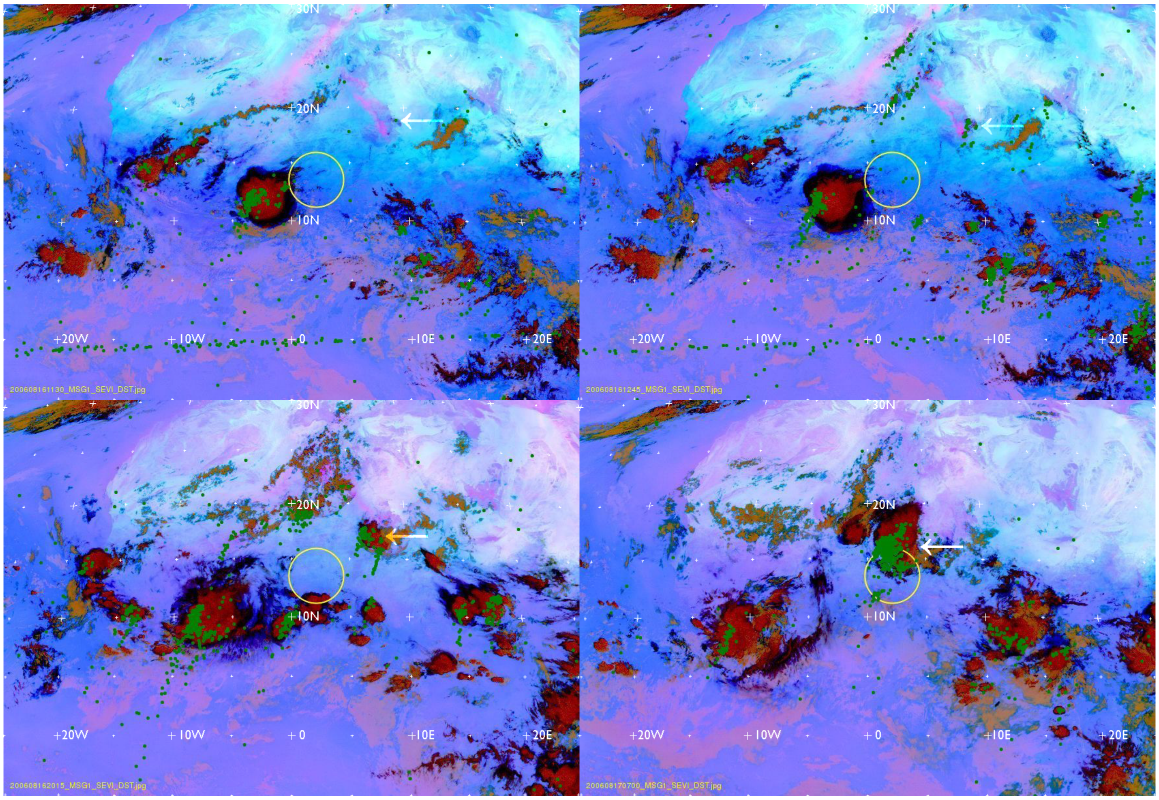

Figure 5-25: These four frames show the SEVIRI dust and lightning annotation for the MCS that was tracked with Lagrangian techniques from 16 August, 1100 UTC to 17 August, 1500 UTC, with a gust front launch inferred at 16 August 1245 UTC. Top left: at 1130 UTC on 16 August, convection has barely begun and is just detectable. Top left: a GF launch is recorded at 1245 UTC on 16 August; the front is hard to see in this image but can be backtracked from future images and is easier to see in a time sequence of SEVIRI alone (the front is mostly under lightning strokes). Bottom left: at 2015 UTC on 16 August, the MCS has developed into a strong system; its front can be clearly seen as an arc at the leading edge of the MCS. Bottom right: at 0700 UTC on 17 August, lightning activity has increased as the MCS continues to develop, but the front edge can still be seen. Note how the apparent size of the MCS as shown in SEVIRI imagery is much larger than the convectively active region shown by the lightning.

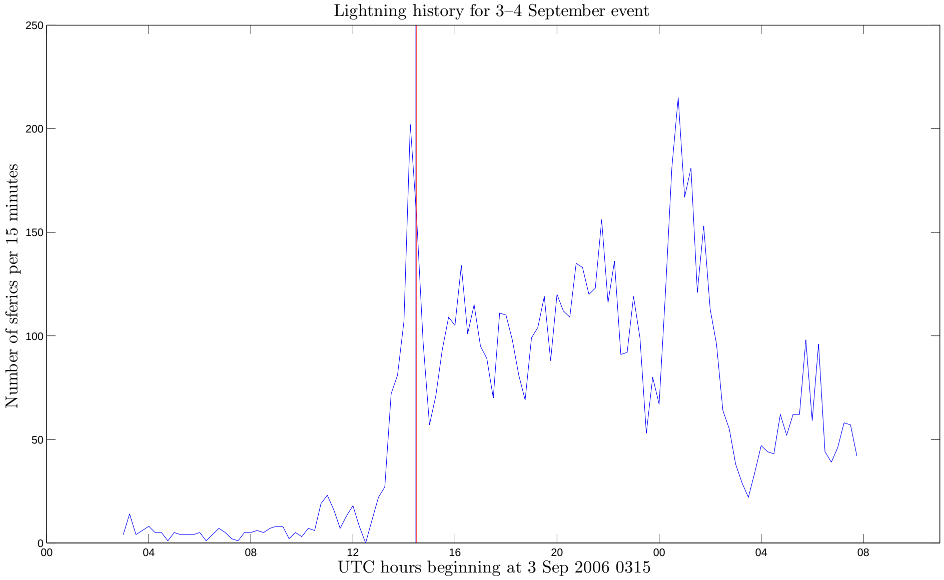

Figure 5-26: The Lagrangian lightning count from 3 September 2006, 0315 UTC to 4 September 2006, 0730 UTC with a gust front launch inferred at 3 September 2006, 1445 UTC (red line), bounded by longitude 10 W to 7 E and latitude 12 N to 20 N. The gust front reached Niamey on 3 September 2006 1443 UTC (blue line).

2006 at 0315 UTC and experienced a strong surge at about 1430 UTC; a gust front was launched from the MCS at about 1445 UTC, directly above the MIT radar and soon interacted with another front to produce new convection; the original MCS was no longer detectable in SEVIRI after 0730 on 4 September. SEVIRI context for the gust front immediately after its launch is show in Figure 5-27.

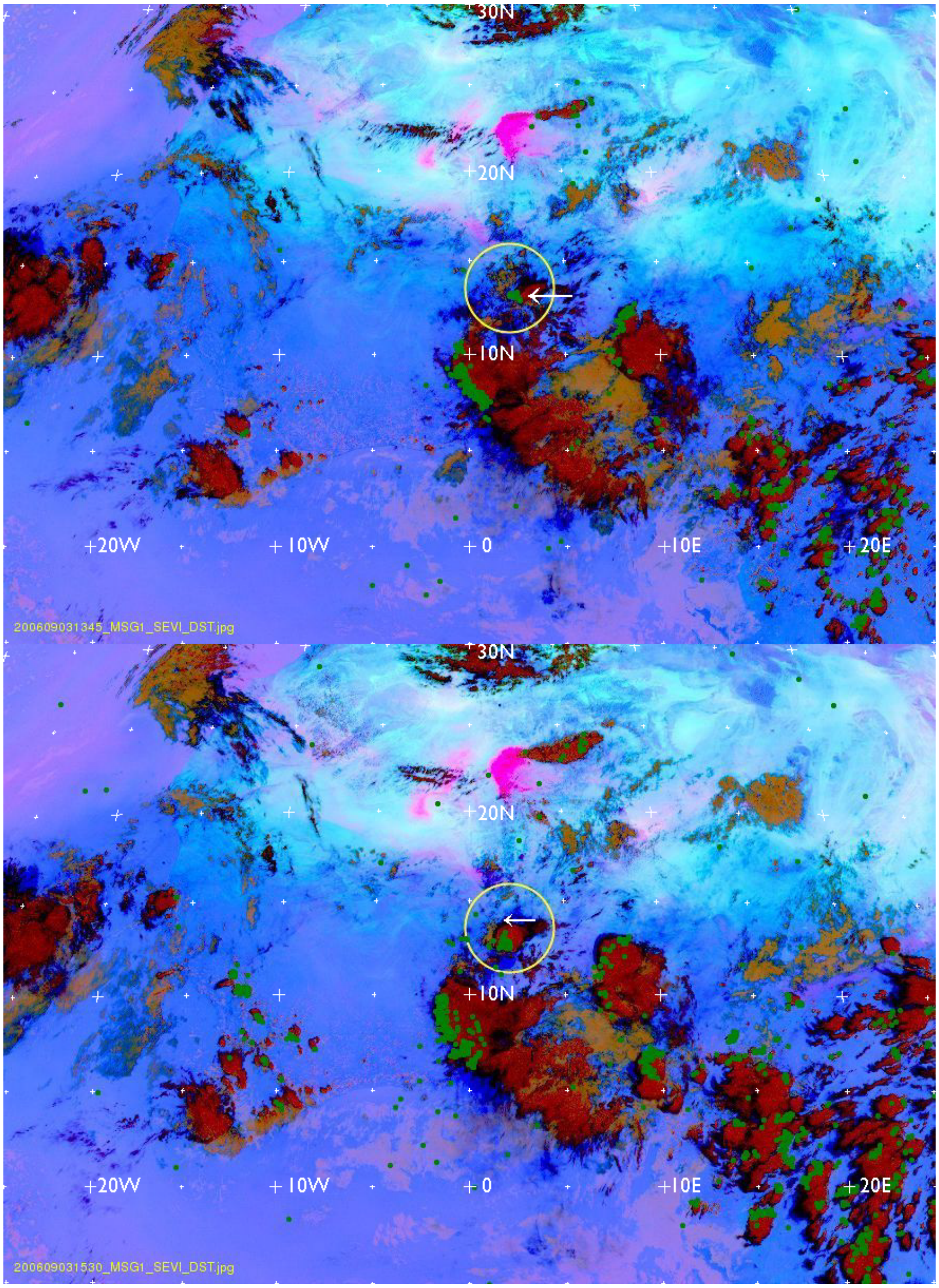

Figure 5-27: Top: the SEVIRI infrared dust images for 3 September 2006 at 1445 shows a small gust front being launched just above the MIT radar site; the gust front is largely obscured by lightning. Below: the SEVIRI infrared dust image on 3 September at 1530 shows the GF as an arc propagating in front of the squall line. The gust front is relatively poorly detected by SEVIRI.

5.6 Propagation distances for gust fronts and squall line MCSs

Our measurement of mean gust front propagation distance at 750 km provides a new "typical" range for the extent of squall-line associated gust fronts, for which the previous best observations (radar or inferred passage at a surface station) were less reliable (see Section 2.1). This range puts many gust front propagation distances within a factor of two of an African easterly wave's wavelength (usually at least 2000 km). These results highlight the importance of measuring gust front propagation with SEVIRI, rather than merely looking at the short propagation distances radar detects.

In order to understand how gust fronts interact with the MCSs they are sometimes created by, and sometimes generate, we compare the typical measured extents of each kind of event. SEVIRI produces images at the appropriate resolution to measure both of these features. Gust fronts which propagate relatively large distances are likely to cross another boundary, creating conditions that are favorable to (but not necessary for) new convection (see Section 3.3). Understanding these fronts' behavior, and knowing the typical diurnal behavior of storms and gust fronts, can aid in the prediction of new convection on the time scale of 2-3 days, beyond the life time of any particular gust front. Gust fronts with greater propagation distances have a larger total area over which new convection can be initiated, so understanding what affects extents will improve understanding of which gust fronts are likely to initiate new convection.

Figure 5-28 gives the distribution of gust front propagation distances. The maximum, about 1920 km, represents an unusually active system, but even a moderately sized system may travel over 1000 km. Satellite image deficiencies alone do not explain the five-fold variation in lengths, from 300 km to 1920 km. The propagation of gust fronts as density currents depends on the initial temperature drop, initial thickness, and the turbulence level in the boundary layer. We have also shown (Section 5.4.2) that gust fronts from isolated events propagate a mean distance of only 450

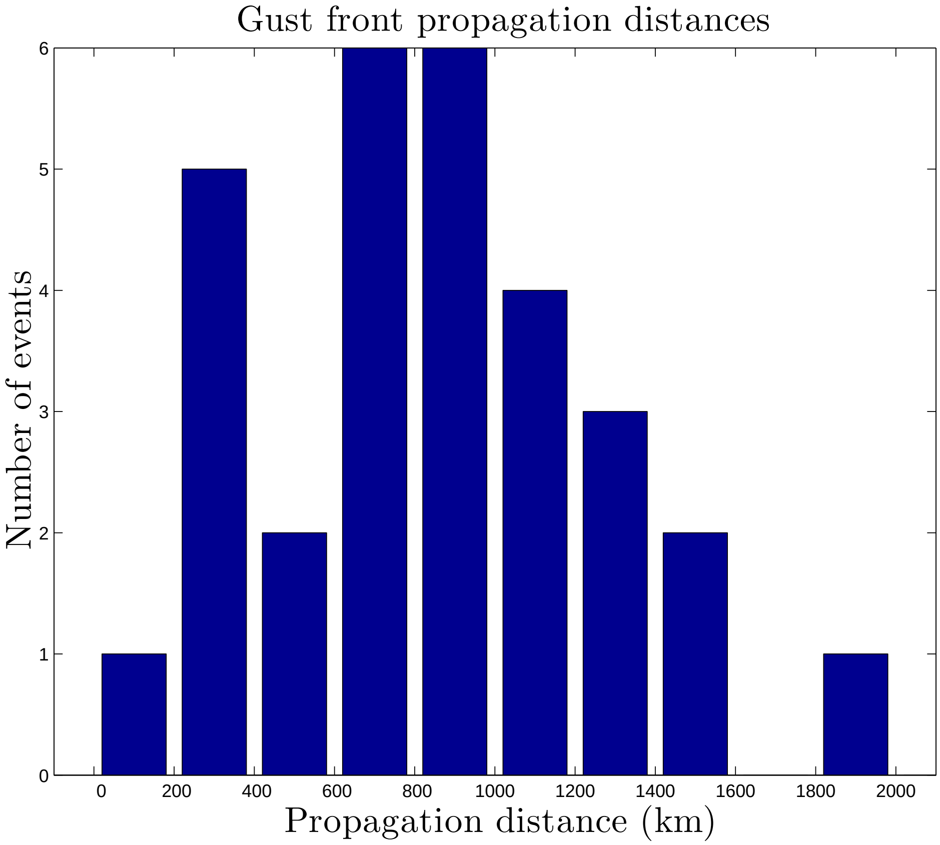

Figure 5-28: Distribution of gust front propagation distances for events whose origin and end were tracked with SEVIRI infrared dust imagery cross-section method. This distribution includes events generated from isolated storms as well as events generated from squall lines.

km, versus 990 km mean for gust fronts generated from squall lines.

These gust front propagation distances are shorter than the same quantity for MCS systems, measured by direct observation of when systems begin to propagate and stop propagating in SEVIRI infrared dust imagery (Figure 5-29). This is no surprise: an MCS does not typically represent a single cell or squall line, but rather a family of convective activity traveling in the same direction and often with approximately the same phase. Moreover, upper level cloud may continue advecting even in the absence of active convection, so these measurements may be overestimates. The gust fronts we measure with satellite measurements may be sustained or renewed by additional convection or by combining with other outflows, but they frequently

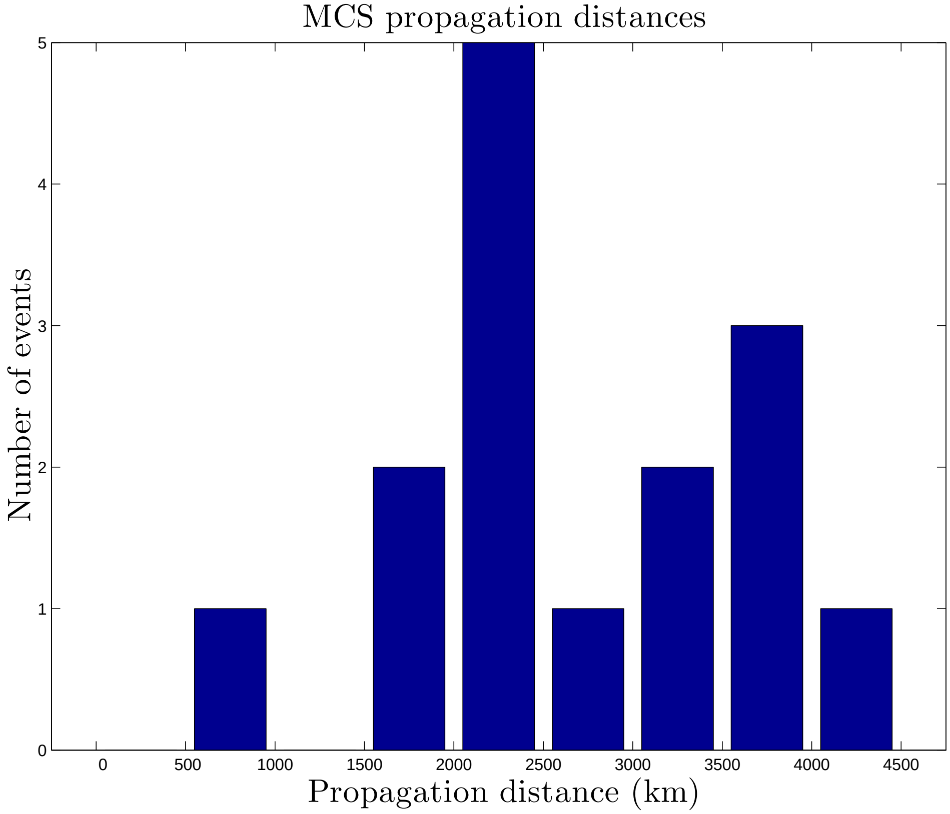

Figure 5-29: Distribution of MCS propagation distances for events whose origin and end were located in SEVIRI dust product images.

stop being detectable: as the beginning of an MCS's journey west, the gust front disappears into another front or forms new convection that sets up a new squall line, and at the end of an MCS's journey near the edge of the continent, the gust front will dissipate while some new convection and lightning will continue further west.

Figure 5-30, a comparison of radar-measured gust front speeds, MCS speeds, and lightning stripe average speeds, shows that gust fronts exhibit substantial variation in speed, although their average instant speed is roughly comparable with that of the events that spawn them. At the MIT radar site, gust fronts are occasionally measured traveling slowly (10 m/s) or very quickly (23 m/s), with a mean 17 m/s. MCSs measured over the long term, based on measuring the distance and time between the last SEVIRI-detected position and the first SEVIRI-detected position of an MCS, vary from 12–21 m/s, with a mean 18 m/s. And the lightning Hovmoller stripes which measure the propagation of a squall line's leading edge vary in average speed 11–20 m/s, with a mean 16 m/s, slower than the mean speed of a gust front.

Because many gust fronts seem to be generated by long-lived MCSs and then to travel at comparable speeds and in the same direction as those systems, we would expect squall-line generated gust fronts to behave similarly to the squall lines that cause them in terms of their age and duration. They are, however, driven by different physical processes: a gust front is maintained as a density current using the temperature difference between the cold pool and its surroundings, while a squall line is maintained by sustained latent heat release.

Mathon and Laurent (2001) found that MCSs with higher lifetimes travel at faster mean zonal speeds (see Figure 6f in *Mathon and Laurent* (2001)). *Machado et al.* (1998) found that MCSs with higher lifetimes in the Americas had lower minimum IR temperatures, indicating higher cloud tops or deeper convection; the longer-lived MCSs also had more convective clusters, a larger system radius, and a larger convective cluster radius (see Figure 8 in *Machado et al.* (1998)). Gust fronts display a similar behavior (Figure 5-31): age is roughly linearly correlated with speed, both determined by measuring SEVIRI cross-sections (discussed in Section 4.3.2). The faster gust fronts (which are also associated with a sharper temperature drop) propagate for longer times.

The absolute number of lightning strokes within the region of lightning activity enclosing a storm measures in some sense the strength of that storm. We can validate the findings of *Mathon and Laurent* and *Machado et al.* about the features of a well-developed MCS by plotting lightning strength (absolute maximum number of sferics during an MCS before a gust front launch) against extent, age, and speed, and we do so below. Maximum lightning strength is positively correlated with both extent (r = 0.26, Figure 5-32) and age (r = 0.39, Figure 5-33); surprisingly, it is negatively correlated with average MCS speed (r = -0.44, Figure 5-34). Storms with stronger peak lightnings tend to propagate for longer distances and for longer times; but they do not dissipate instantly. A more active MCS will take longer for its storm activity to wind down, so it will still remain a measurable MCS even as it moves more slowly,

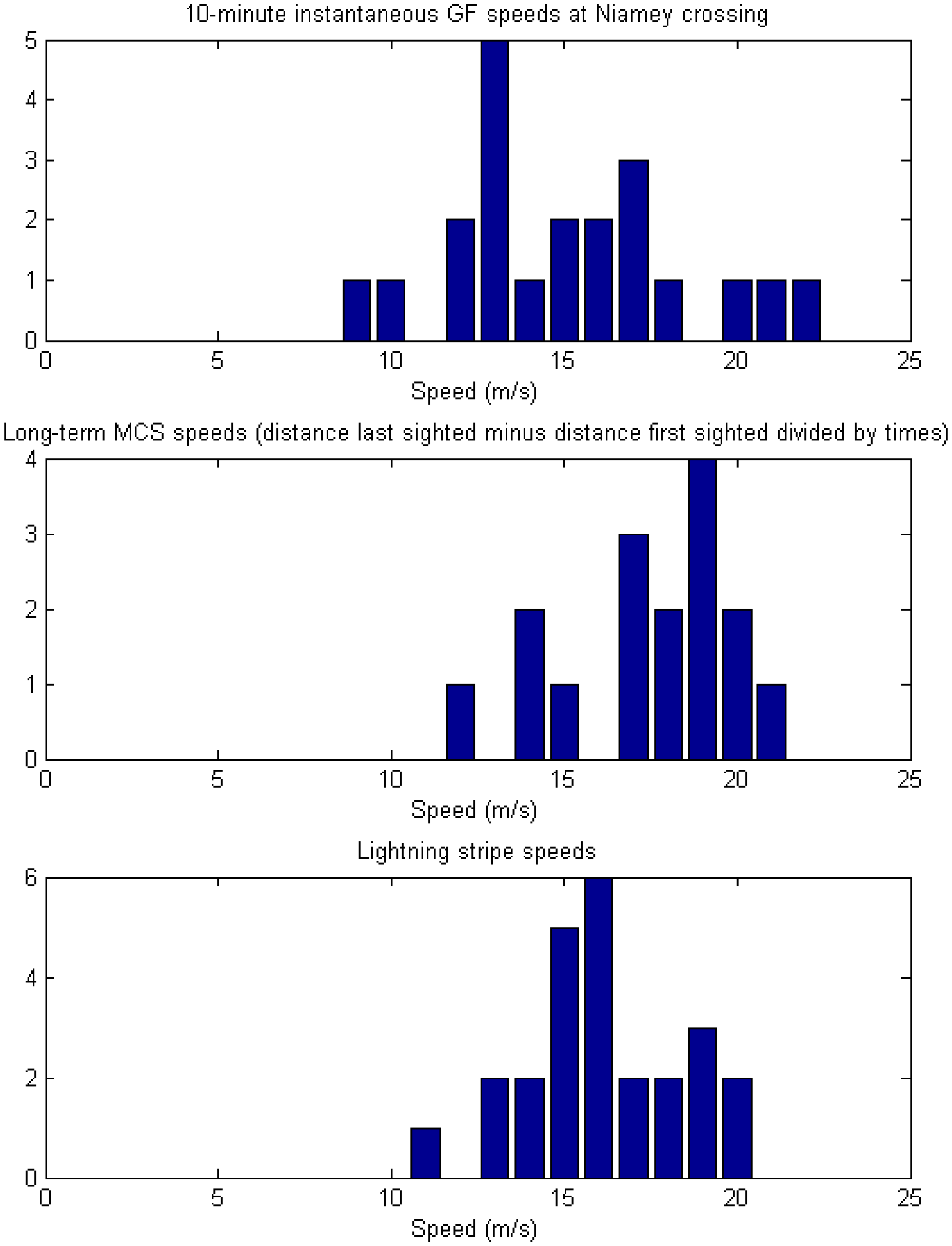

Figure 5-30: Distribution of speeds for gust fronts, MCSs, and Hovmoller lightning stripes that represent the movement of squall line systems. The gust fronts are measured at the 10-minute interval of their crossing over the MIT radar site; MCSs are measured from SEVIRI based on the first and last time and location they are detectable; and lightning stripe speeds are measured as the slope of lightning Hovmoller diagrams.

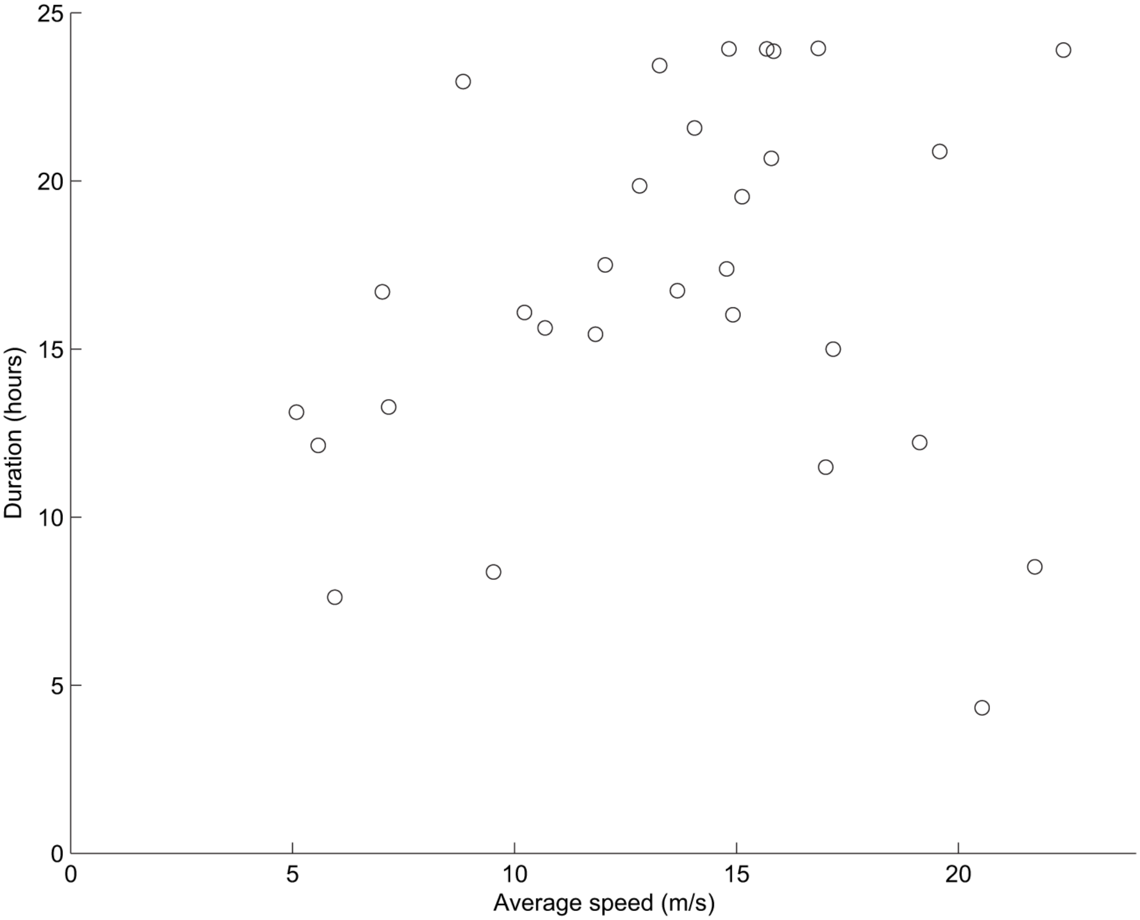

Figure 5-31: Gust fronts' speeds and durations for events which could be tracked using the SEVIRI cross-section method.

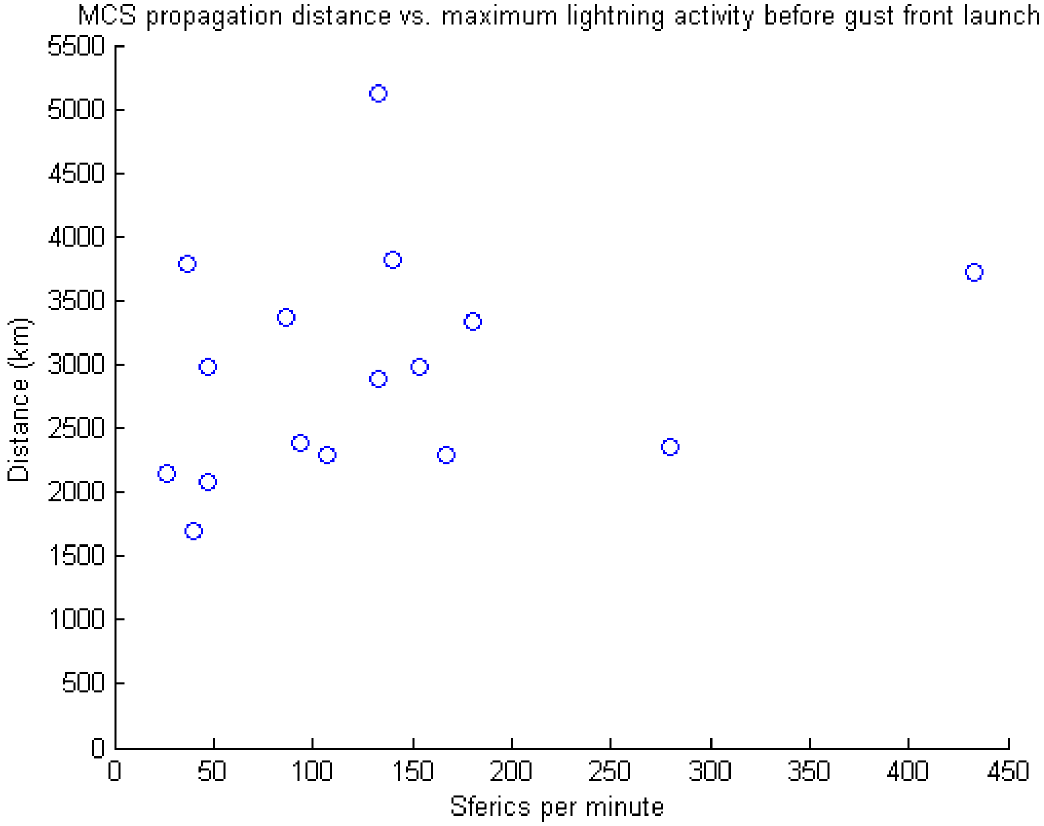

Figure 5-32: Peak lightning strength plotted against measured propagation distance for MCSs which could be isolated using the Lagrangian method and whose propagation could be tracked in the SEVIRI dust product.

and over its entire time of existence, the strong storm will record a relatively weak average speed.

Additional evidence that “larger” storms go further comes from measuring the maximum lengths of squall lines, then comparing those sizes against the propagation distances of the lightning stripes associated with those individual MCSs. We see a strong linear relationship (Figure 5-35, linear correlation coefficient $r = 0.61$): the storms with higher maximum squall line length also propagate longer distances. However, Figure 5-36 shows that there is not a strong correlation between squall line speed and lightning stripe length (linear correlation coefficient $r = 0.20$). Thus our observations do not provide evidence that faster squall lines propagate further.

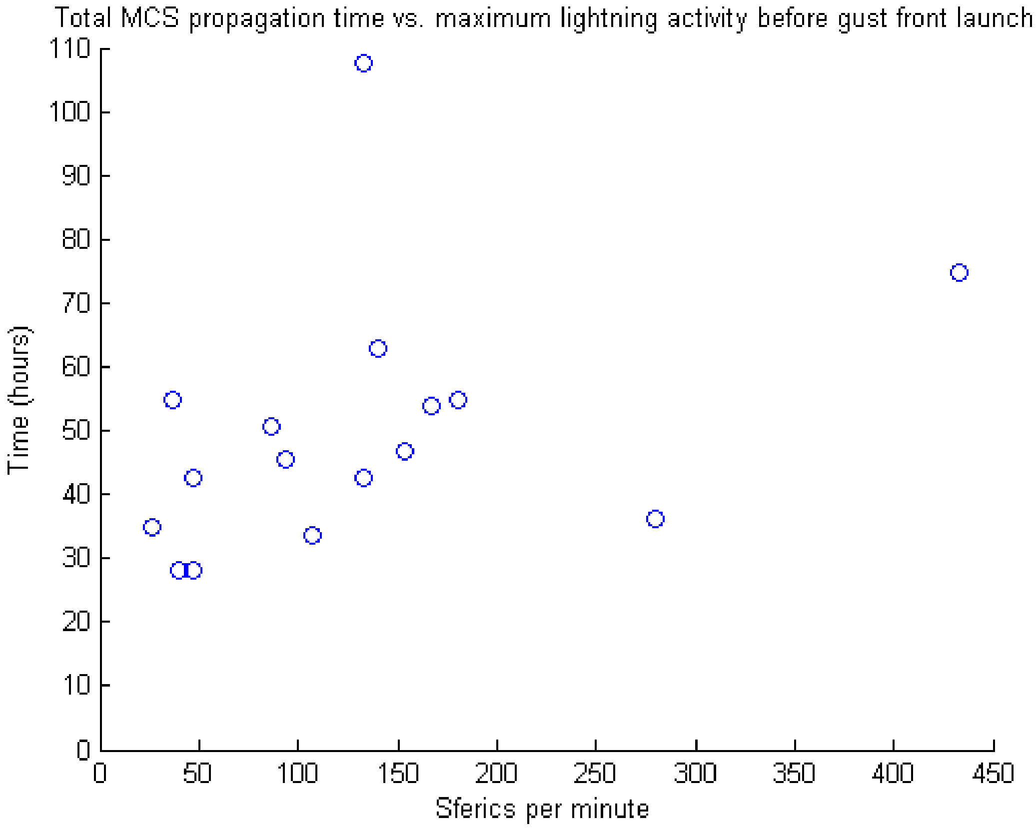

Figure 5-33: Peak lightning strength plotted against measured propagation time for MCSs which could be isolated using the Lagrangian method and whose propagation could be tracked in the SEVIRI dust product.

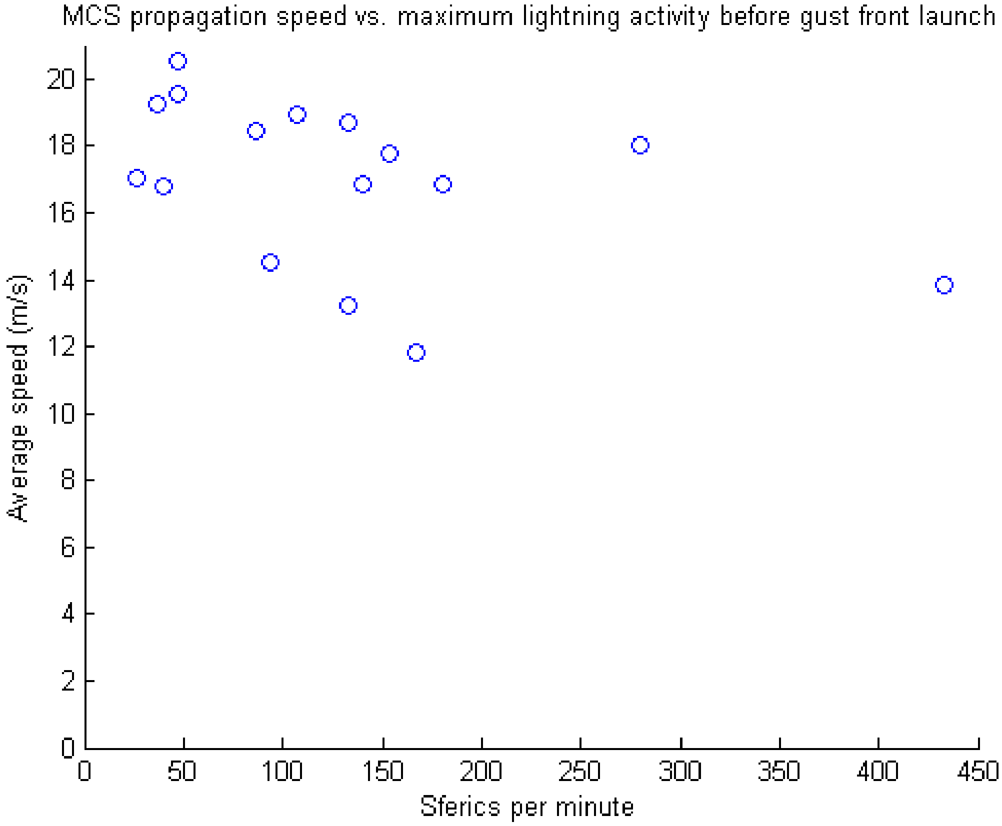

Figure 5-34: Peak lightning strength plotted against measured mean total propagation speed for MCSs which could be isolated using the Lagrangian method and whose propagation could be tracked in the SEVIRI dust product.

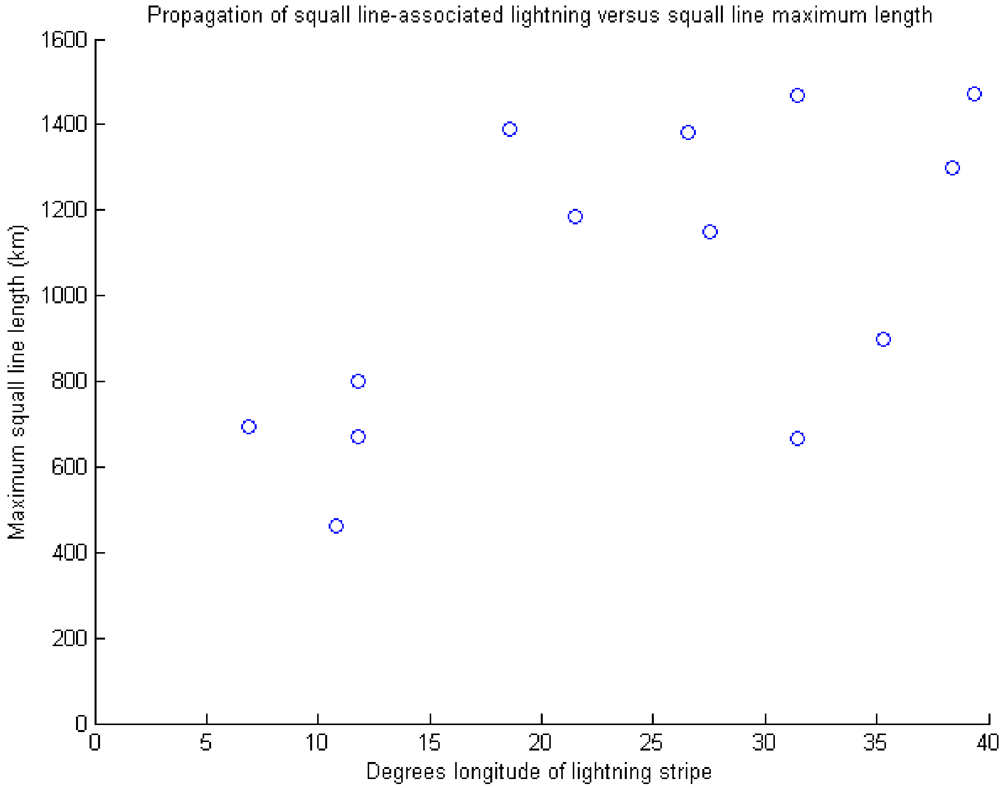

Figure 5-35: Longitudinal extent of a lightning stripe, associated with a squall line system, plotted against that squall line's maximum length, as measured in SEVIRI infrared imagery annotated with lightning stroke locations.

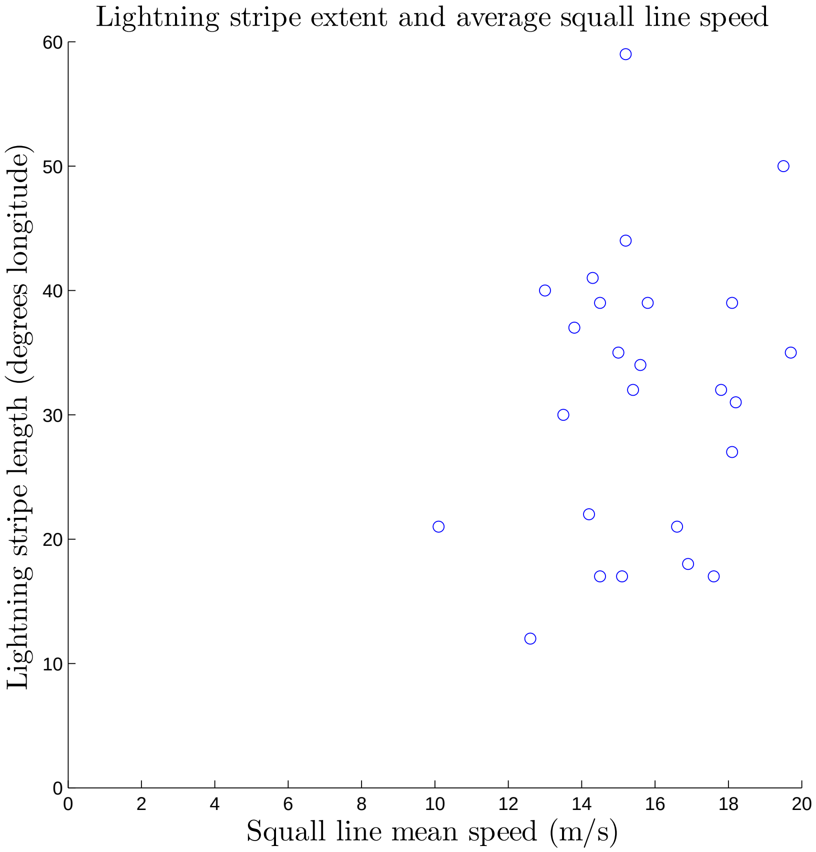

Figure 5-36: Length of the lightning stripe associated with a squall line plotted against that squall line's average speed, determined by measuring on a Hovmoller diagram the lightning associated with a squall line throughout its propagation. These two quantities are not strongly related (linear correlation coefficient r = 0.20), suggesting that faster squall lines do not propagate further.

Day start	Hour start	Long start	Extent (degrees longitude)	Duration (hours)	Speed (m/s)
1 Aug.	12	27	35	72	15.0
4 Aug.	10	25	44	89	15.2
6 Aug.	12	25	41	88	14.3
8 Aug.	12	26	39	83	14.5
11 Aug	12	39	17	36	14.5
13 Aug.	18	18	35	54	19.7
14 Aug.	2	31	12	30	12.6
16 Aug.	12	21	39	75	15.8
20 Aug.	4	17	21	64	10.1
20 Aug.	4	36	18	33	16.9
22 Aug.	18	17	17	35	15.1
24 Aug.	6	25	34	68	15.6
27 Aug.	12	25	39	66	18.1
27 Aug.	8	13	27	46	18.1
29 Aug.	2	34	30	68	13.5
31 Aug.	12	45	59	119	15.2
5 Sept.	8	22	40	96	13.0
7 Sept.	4	12	22	49	14.2
12 Sept.	4	11	32	55	17.8
13 Sept.	12	31	50	79	19.5
16 Sept.	8	32	21	40	16.6
18 Sept.	12	10	17	31	17.6
20 Sept.	12	15	31	53	18.2
26 Sept.	12	25	32	64	15.4
27 Sept.	12	33	37	83	13.8

Table 5.4: Stripes in lightning Hovmoller diagrams

5.7 Continuity of lightning stripes in Hovmoller diagrams

5.7.1 Stripe measurements

The vast number of continuous stripes of lightning within Hovmoller diagrams for August and September suggest that large storms, far from being uncommon, are almost always present in the summer – even if an African Easterly Wave is not. See tabulation of 25 lightning stripes lasting longer than 24 hours, Table 5.4.

The distribution of stripe lengths (Figure 5-37) shows one remarkable result: the

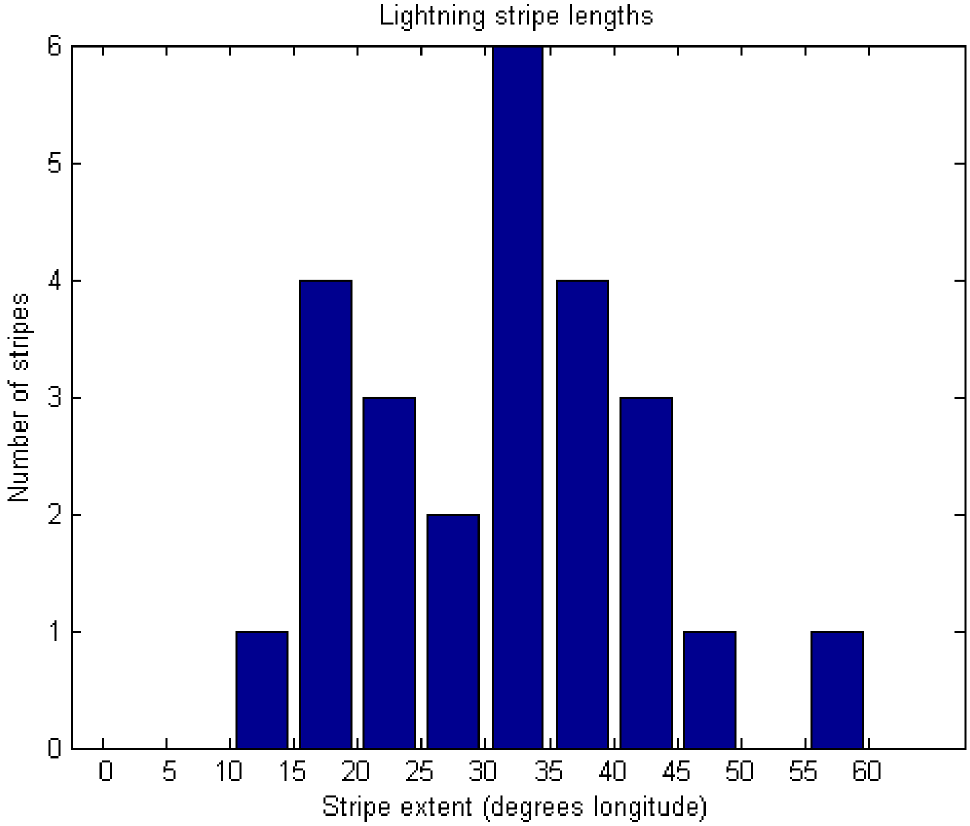

Figure 5-37: Distribution of lightning stripe extents for lightning stripes lasting longer than one day. For a definition of stripes and how they are measured, see Section 4.4.1.

mean lightning stripe length, 32 degrees longitude (about 3500 km), is longer than an AEW. Of the 25 events, 80% (20) extend continuously for greater than 20 degrees longitude (about 2200 km).

Also relevant is the distribution of lightning stripe initiation over time (Figure 5-38): there are twice as many day-or-longer stripes in August than in wetter September. The mean stripe length is nearly the same in each month (31.6 vs. 31.5 degrees longitude).

We have assumed that lightning stripes are a reasonable measurement of the movement of squall lines because, based on visual inspection of movies showing lightning overlaid on cloud images, the bands of lightning look like the leading convection typically observed in a radar profile of a squall line. We can justify this assumption by looking at measurements of squall line speed as they cross the MIT radar site

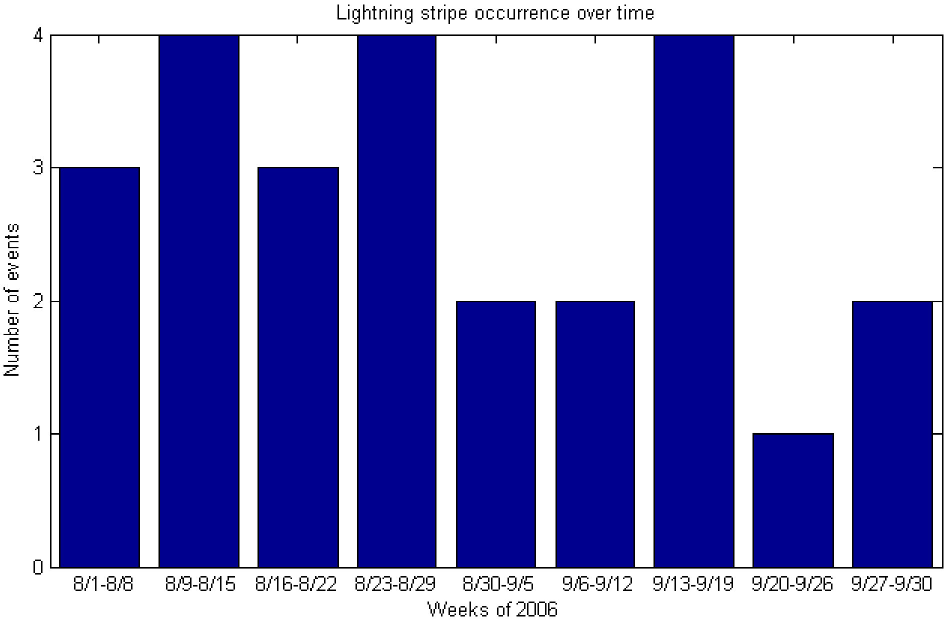

Figure 5-38: Distribution of lightning stripe initiation times over the months of August and September.

(*Rickenbach et al.*, 2009). These squall line speed measurements are only valid for the limited time when the squall line was detected by the radar, and only for the fraction of the squall line that appeared on the radar; but the speeds still match closely (Figure 5-39) linear correlation coefficient r = 0.44). So lightning stripe speed is a reasonable measurement of MCS speed.

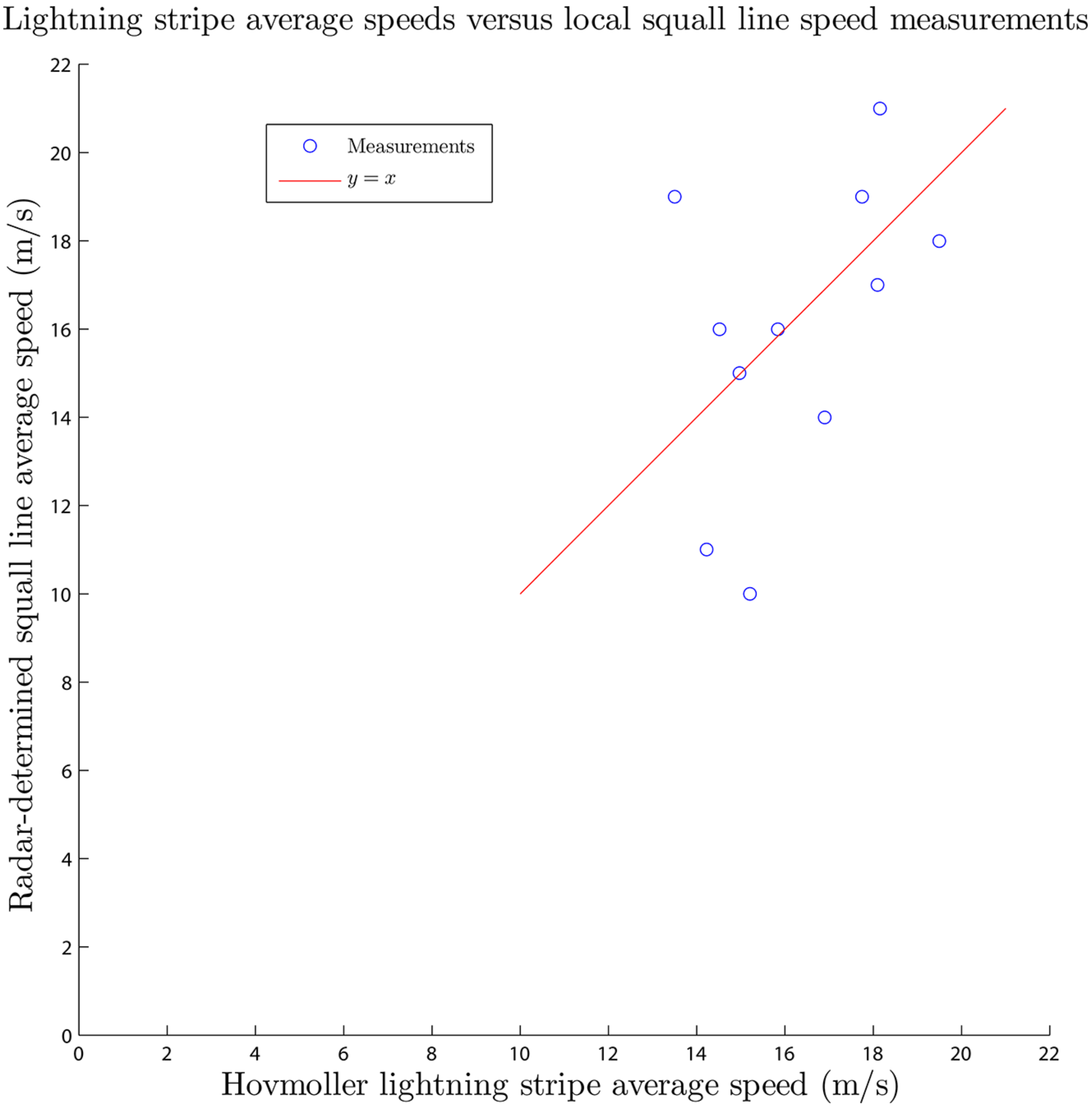

Figure 5-39: Squall line speeds measured by *Rickenbach et al.* (2009) based on radar data, plotted against the speed of the lightning stripes which included those squall lines. For reference, a 45-degree line $y = x$ is also shown. Not all squall lines were clearly associated with a lightning stripe; those squall line speeds are not shown. (We chose to measure lightning stripes with duration greater than 24 hours.)

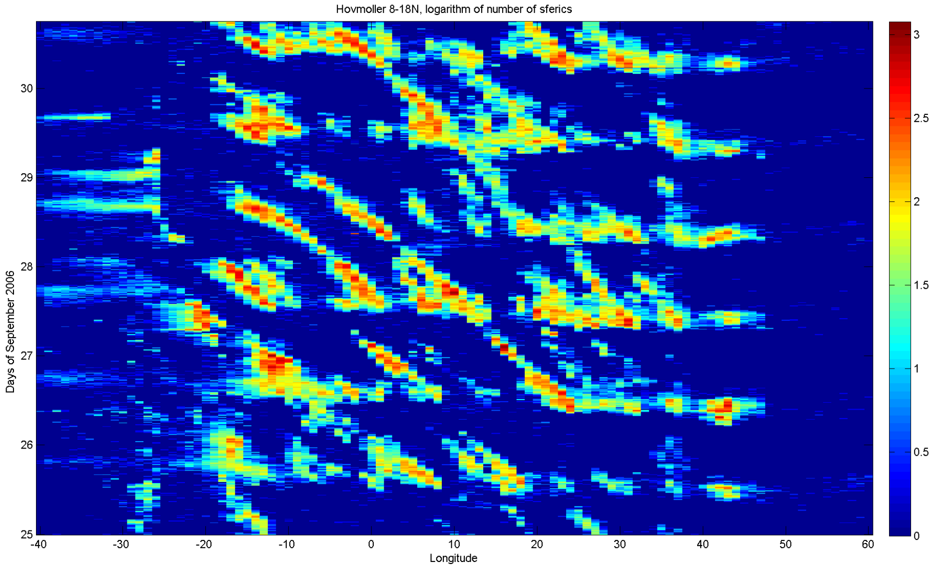

Figure 5-40: Lightning Hovmoller for 25–30 September, showing the daily "sun stripe" and associated solar-assisted convection.

5.7.2 Sun stripes

Janiga et al. (2009) reports a local maximum in convective initiation at 1800 UTC, which is consistent with the report of *Sultan et al.* (2007) of a local maximum at 1800 UTC in the intertropical convergence zone (ITCZ) at 15–20 N. A similar convective maximum is visible, but slightly earlier, in the lightning stripes, in the form of a faint but consistent fast horizontal stripe all across the Hovmoller diagram: this stripe represents daily diurnal convection. See Figure 5-40. If this stripe were directly linked to the movement of the sun, we would expect to see it travel 360 degrees longitude in 24 hours, or 460 m/s at the equator. In practice, the time onset of convection can vary up to an hour before or after the stripe arrives, and the stripes we measure may be as wide as 4–6 hours. On average, however, we see the stripe propagate at a fastest speed of about 60 degrees longitude per 5–6 hr, implying a phase speed of 310–370 m/s. This phenomenon deserves further study.

This sun stripe reaches 0 longitude between 1600–1800 UTC (also 1600–1800 local time) in late September[2]. We can qualitatively gauge the effect of diurnal solar heating

---

[2] The time varies between days because it reflects a manual measurement of when the intensifi-

by following the “sun stripe” across the Hovmoller; for example, on September 26, sun-assisted convection is seen between 10 W and 0 longitude, but the convection is not very strong and it does not last beyond a few hours. (See Figure 5-40.). When the “sun stripe” encounters a long-lived lightning stripe, lightning activity intensities. Solar convection often contributes re-intensification to a lightning stripe, enhancing its convection enough that continuity is visible on a lightning Hovmoller diagram.

---

cation begins, and there is frequently already some convection which is strengthened when the “sun stripe” arrives.

5.7.3 Lightning stripe continuity, with gaps

Remarkably, these lightning stripes show continuity in phase speed even after pauses, with no offset. Lightning-generating convection frequently stops for a few hours, but it picks up again, several degrees longitude along and several hours later, with the same phase as the preceding convection, creating continuity within a stripe. The parts of a stripe between gaps typically do not have offsets – the disturbance proceeds at the same speed, even when it does not generate lightning. Figure 5-41, a lightning Hovmoller for August, shows these trends at the month scale (a Hovmoller for September is presented in Figure 4-4; in practice, we measured stripes more precisely using images that showed only five or six days at a time, for example Figure 5-40.

These stripes' length and duration suggests they are influenced by synoptic-scale systems. The usual contributor to convection in West Africa, the AEW, does show a correlation with lightning activity, but not in the expected way. Figure 5-42 shows that these lightning stripes are faster than the AEW and are unlikely to follow one exactly (see Section 1.4 for references that give typical AEW speeds over many seasons, typically around 8 m/s, sometimes up to 11 m/s) These lightning stripe speeds are almost comparable with the maximum surface wind speeds of the AEJ, modeled at up to 15 m/s in dry conditions or up to 9 m/s in wet conditions (*Hsieh and Cook*, 2005). If there were a preferred place along the jet for convection to develop, it might explain the spike in lightning stripe average speeds, shown in Figure 5-42, at around 15 m/s. 40% of stripe average speeds (10 of 25) are below 15 m/s, and 64% (16 of 25) are below 16 m/s.

Since we have shown (Figure 5-30) that gust fronts have similar speeds to squall line speeds, it is logical to examine whether many of the discontinuities in the lightning stripes can be explained using gust fronts. 16 gust fronts crossed Niamey in August or September 2006, the months where lightning data are available. Of those 16 gust fronts, 10 (63%) show a clear influence of the gust front in mediating continuity in the lightning stripe. We present a few specific, strong cases.

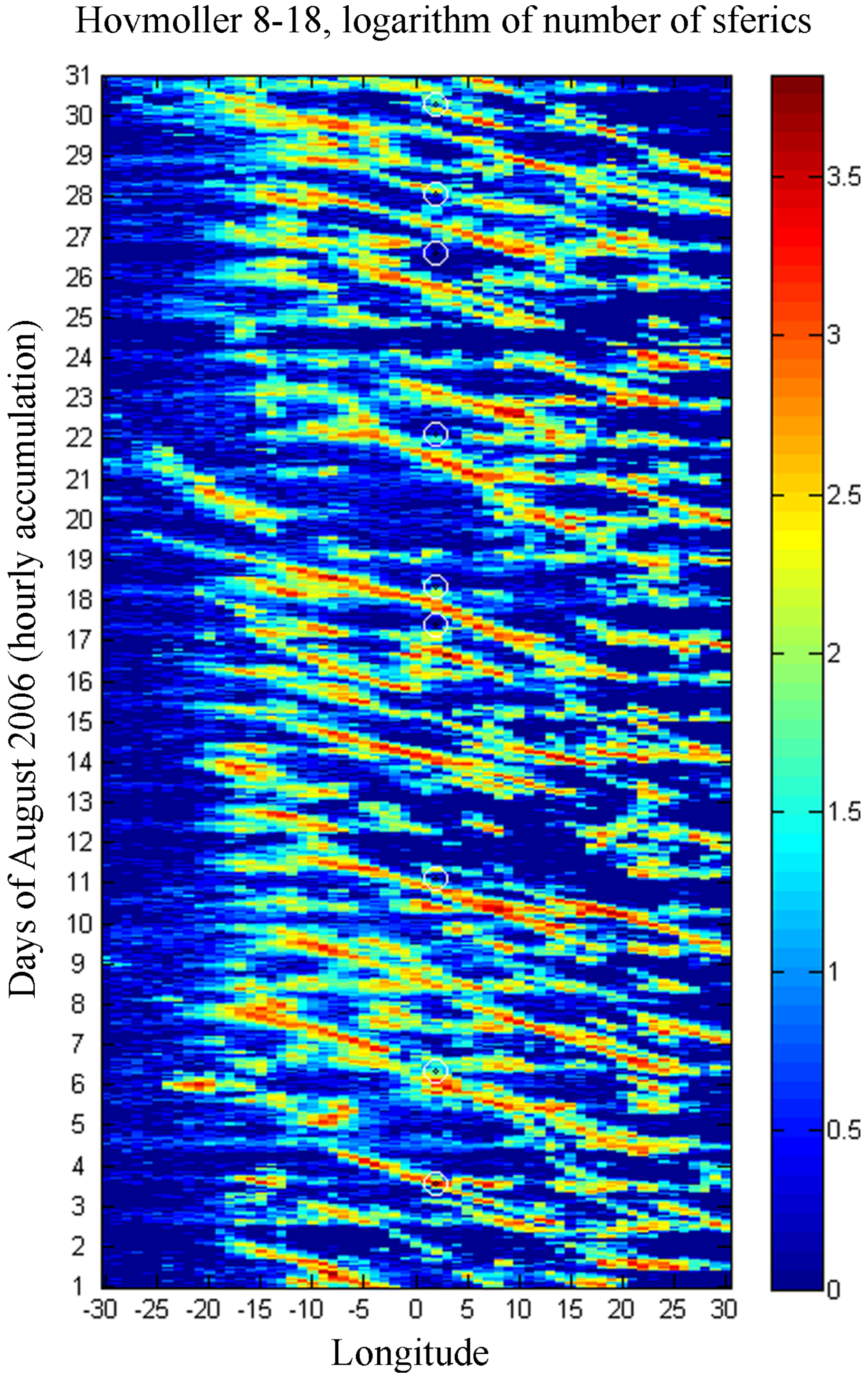

Figure 5-41: This Hovmoller diagram shows lightning strokes for August 2006 integrated from 8-18 N latitude. Each distinct cell in the image has dimensions 1 hour by 1 degree longitude. Circled in white at 2 E longitude are the times when gust fronts were observed to cross the MIT radar at Niamey. A Hovmoller diagram of lightning activity for September is given in Figure 4-4.

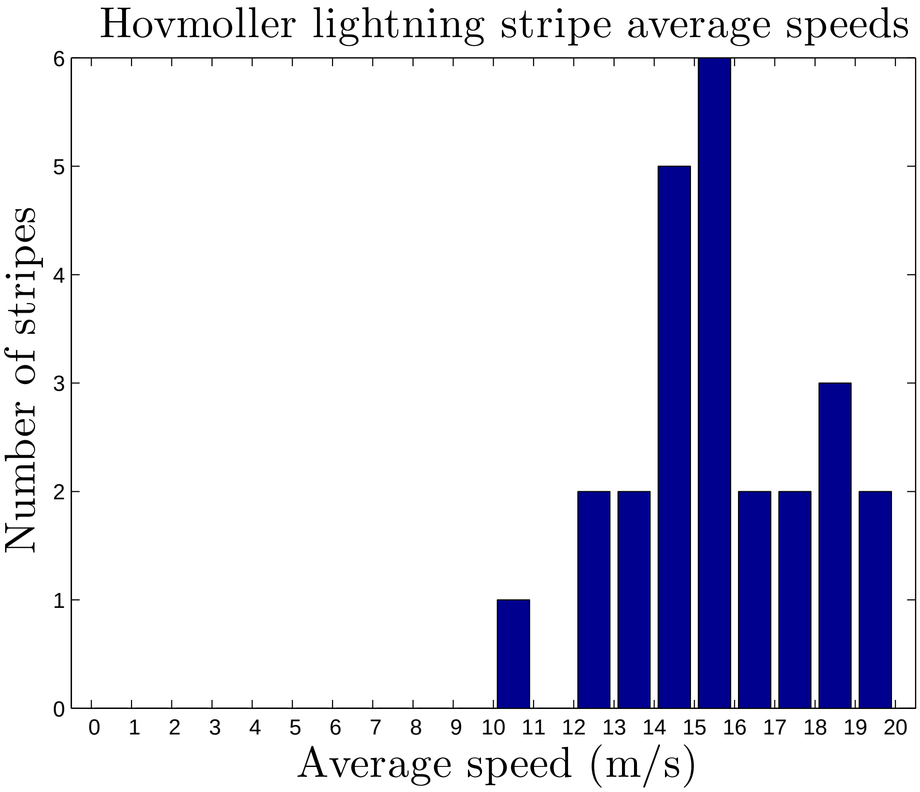

Figure 5-42: Average speeds for lightning in Hovmoller stripes.

On 28 August 2006, a gust front with a 6.5C temperature drop that precedes a squall line full of lightning just before 0300 UTC at Niamey. That gust front was originally launched on 27 August at 14:45 UTC. After the gust front crosses the MIT radar site, the lightning subsides and the trailing anvil cloud has partially dissipated, when several hours later new convection begins again, west of Niamey, along the arc of the gust front. The lightning stripe shows a quiet period surrounded on both sides by a long stripe of lightning activity, with the same phase and speed on both sides, while the gust front continues.

On 12 September, a multiple-cell MCS crosses Niamey, preceded by a gust front crossing just after 15:00 UTC with a temperature drop of 10.3C (the fourth largest drop of any gust front recorded in summer 2006). New convection forms along the gust front after it passes, creating a line of lightning activity that results in lightning stripe continuity.

On 8 September, a gust front crossing Niamey at 05:04 UTC precedes a small MCS which subsides into weak lightning activity and a cloud that continues to move west. New convection forms along the gust front, creating a new, larger, MCS that exhibits lightning stripe continuity.

On 3 September, a gust front forms at 14:45 just north of Niamey, while an MCS propagates southwest of Niamey. The gust front intersects with the boundary of the MCS and new convection forms to the west of Niamey.

But not every lightning stripe shows a gust front or new convection forming along that front. Sometimes the gust front accompanies a single squall line of lightning closely – for example on 24 September, when a gust front travels along with a squall line but there is no evidence of the gust front propagating in the squall line's absence (perhaps because it is obscured by cloud). Other times, the stripe continuity may happen in a series of self-renewing MCSs, for example on 30 August, when the gust front accompanies a complex MCS consisting of several cells, some of which dissipate while others form along the squall line. And the detected gust front may simply fail to create new convection. On 21 August, a gust front propagates out past a lightning-filled squall line 250 km east of Niamey at 1830 UTC; the gust front is about 50 km from the squall line, but its distance increases to about 500 km (with the gust front at 4 W and the squall line at 1 E, both centered at about 15 N) by 0545 UTC on 22 August, and no new convection forms on he gust front, which cannot be detected in SEVIRI dust product images beyond its position at about 10 W at 1645 UTC on 22 August. New convection does form along the squall line, creating lightning continuity, but no new convection forms along the arc of the gust front.

5.8 Synoptic-scale context for MCSs

The conventional view of African Easterly waves is that they are a straitjacket on the development of MCSs: *Payne and McGarry* (1977) and *Reed et al.* (1988) show how storms develop on one end of an AEW (west of the trough) and propagate through it before dissipating at the other end (east of the ridge). It is not immediately apparent that this view is consistent with our findings for summer 2006, which show a large number of long-lived lightning stripes propagating as far as an AEW wavelength and twice as fast as the typical AEW. We present an interpretation of these data in which the large number of stripes make sense: the stripes which propagated for far enough to pass through an AEW only occurred when there was no wave to constrain their motion. That is to say, for several weeks in summer 2006, AEW activity was so weak as to allow these stripes to propagate. These stripes are not unusual outliers — they are typical features of MCSs in August–September 2006.

In Section 1.4, we showed that extensive study of AEW interannual variation of AEJ instability has yielded AEW phase speeds anywhere from 6–12 m/s and wavelengths anywhere from 2000–4000 km, with speeds of 8 m/s and wavelengths of 2000–3000 km representing reasonable bounds on the size of the AEW. The lightning Hovmoller stripes we observed, representing organized convective systems, are about twice as fast as the typical AEW with mean phase speed 16 m/s (see Table 5.4) and their mean propagation distance of about 3500 km is at least the size of the typical AEW wavelength. lightning stripes we have documented. One might think, from these numbers, that systems could be detected moving through an AEW, which would be a surprising result.

Atmospheric lightning provides useful information about squall line movement and MCS propagation, but to what extent are these MCSs affected by synoptic-scale wave activity, in particular the African Easterly Wave? The potential vorticity context of West Africa, available from European Centre for Medium-Range Weather Forecasts (ECMWF) models, gives us some information about how wave activity and MCS development can interact.

We do not see evidence that MCSs propagate through the ridge of an active AEW, a result consistent with the literature (*Fink and Reiner*, 2003). Instead, the remarkable number of long-lived stripes shows that although AEWs are prominent contributors to rainfall in the West African summer, they are not a constant phenomenon and may be suppressed for weeks at a time. The results of this tracking, in Table 5.5, suggest that some of the largest MCSs with large squall line lengths can thrive without substantial interaction with the AEW. This is a very different result than that reported by *Fink and Reiner* (2003), who said that AEW-forced squall lines exhibit no extraordinary characteristics such as lifetime or size compared with other squall lines. In contrast, we show that in summer 2006, squall lines which form outside of the influence of an AEW do show extraordinary characteristics, and that the "ordinary", AEW-suppressed behavior is not typical compared with those squall line systems associated with long lightning stripes.

To create Table 5.5, we examined the synoptic-scale activity associated with several lightning stripes. In 4 of 10 cases, there is strong AEW activity, the stripe begins near the wave's trough and ends before the wave's ridge, and the MCS's longitudinal extent is limited to less than half an AEW wavelength, consistent with the interpretations of *Reed et al.* (1988) and *Payne and McGarry* (1977). In the other 6 cases, there is little wave activity, and the lightning stripes are long (greater than 20 degrees longitude extent).

In summer 2006, strong, well-formed synoptic-scale disturbances consistent with an AEW crossed Niamey on 24 July, 16 August, 24 August (an intense but poorly organized wave), 29 August, 1 September, 10 September (the wave that gave rise to

Date	Notes	Stripe length (degrees)	Ridge / Trough / Max lightning location
11 Aug.	No well-defined AEW	39	
17 Aug.	Lightning maximal west of trough; no clear ridge	11	T=2W, L=10W
18 Aug.	No wave	38	
22–24 Aug.	Huge wave, most strongly non-zonal of season	17	
27 Aug	No clear wave: all wave structure is south of AEJ	27	
6 Sept.	Notably non-zonal	<10	
8 Sept.	Biggest MCS of season, lightning approaches ridge	22	T=10E, L=4E, R=5W
10 Sept.	At 0600 UTC, strongly zonally perturbed	<12	T=3W, L=8W, R=20W
10 Sept.	At 18 UTC, pre-Helene wave activity	<10	T=10W, L=14W, R=20 W
11 Sept.	Strongest wave of season	15	T=10W, conv.=18W

Table 5.5: Synoptic-scale context of selected squall line MCS systems in 2006. The date reflects the time the MCS (as observed via lightning stripe) crosses Niamey.

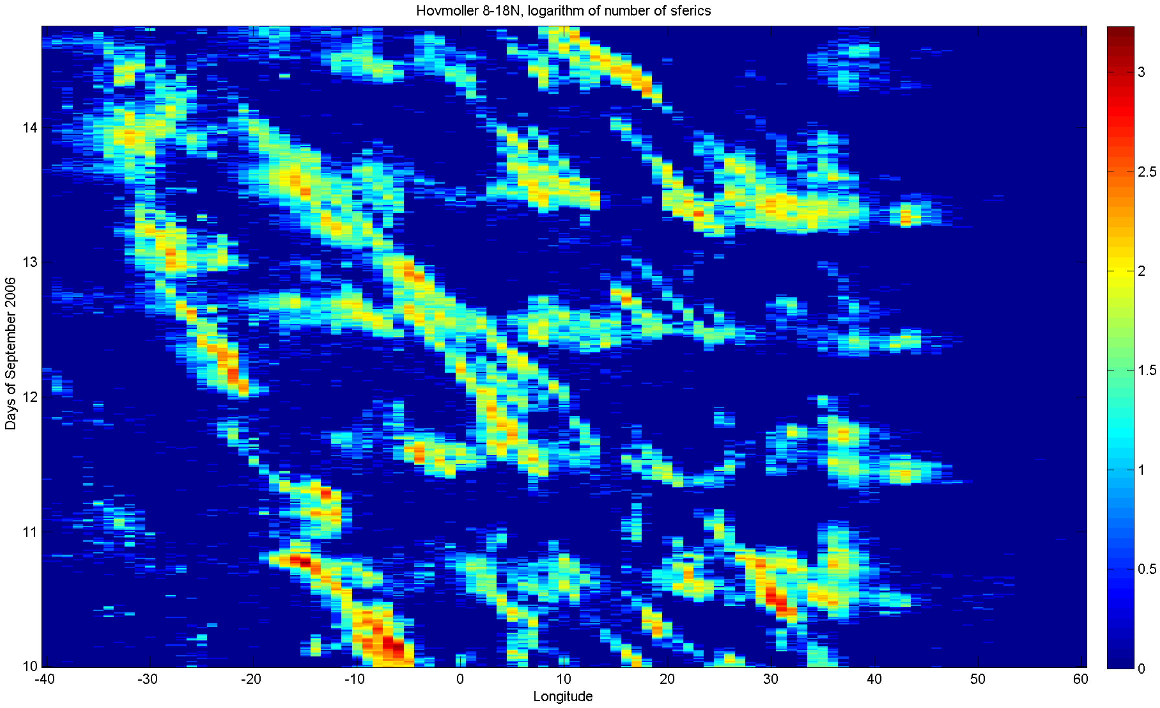

Figure 5-43: This Hovmoller diagram shows lightning activity for 10–14 September 2006, integrated over 8–18 N. Each cell has dimensions 1 degree longitude by 15 minutes. *Thorncroft* (2010) remarks that the AEW which became Hurricane Helene exerted sufficient influence to disrupt the diurnal lightning and drive lightning activity west of the Helene trough, which was located at 3 W at 0600 UTC and at 10 W at 1800 UTC on 10 September and was located at 10 W on 11 September.

Hurricane Helene), 13 September, and 17 September (*Janiga*, 2010).

The Helene event is notable because it was one of two major hurricanes in the 2006 Atlantic hurricane season, in which tropical storm activity was consistent with the 40-year average but weak compared with prior years (*Franklin and Brown*, 2008). The mesoscale environment around the tropical wave that became Helene was deep, cold, and not vertically developed; it reduced convection and arrested gust front activity for days. *Thorncroft* (2010) remarks that the influence of Helene is such that the synoptic scale disrupts diurnal lightning during the pre-Helene period on 10 and 11 September. (See Figure 5-43.)

A short, Helene-influenced lightning stripe begins at 18 W just before midnight on 12 September, off the coast of Africa west of Helene's trough (around 10 W), and continues for a little over a day. It follows the typical pattern of MCSs observed in

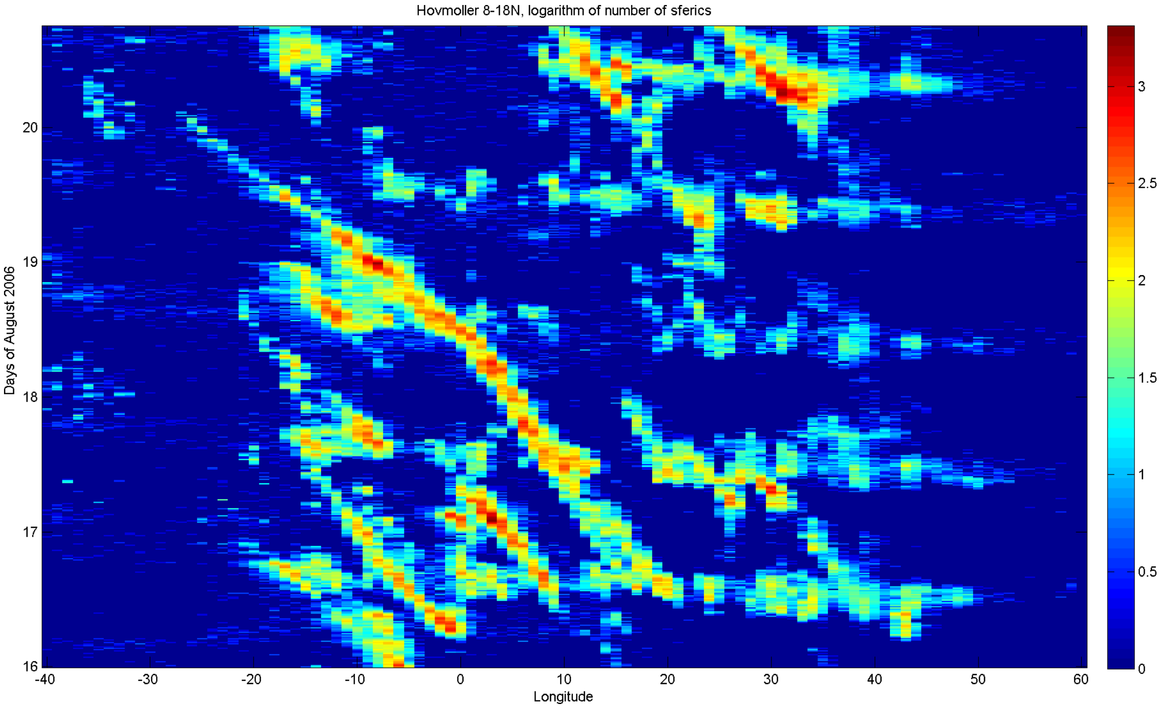

Figure 5-44: This Hovmoller shows lightning activity for 16–20 August 2006, integrated over 8–18 N. Each cell has dimensions 1 degree longitude by 15 minutes. It includes one long-lived lightning stripe which propagates for 38 degrees longitude, beginning just east of 20 E on 16 August and ending close to midnight on 20 August. Throughout the propagation of the MCS, it encountered no significant AEW activity.

the GARP Atlantic Tropical Experiment (*Payne and McGarry*, 1977) and propagates westward only 15 degrees, unable to overcome the damping effect of the AEW.

By way of comparison, in the absence of wave activity, an MCS system that crosses Niamey on 18 August propagates for 38 degrees longitude (about 4200 km) from 16 August until nearly 20 August. The system changes slope slightly midway through 18 August around the time it crosses Niamey (see Figure 5-44, the associated lightning Hovmoller). A plot of the system's motion as observed in combined SEVIRI infrared dust imagery and lightning strokes that shows its propagation across the continent is shown in Figure 5-45.

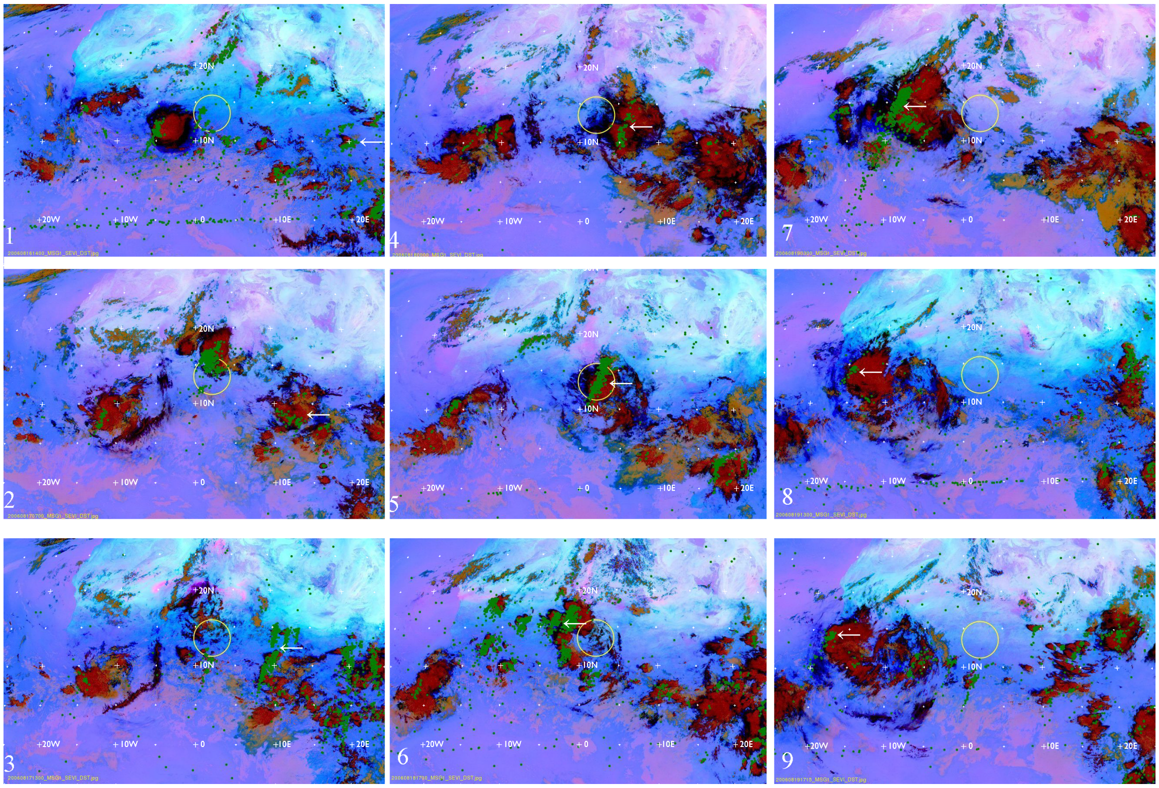

Figure 5-45: Selected image frames show the development of the long-lived MCS system observed as a single continuous 38-degree-longitude lightning stripe in Figure 5-44.
Frame 1, 8/14 1400 UTC: the MCS starts at about 20 E.
Frame 2, 8/17 0700: the MCS, now at 10 E, appears to have mostly subsided.
Frame 3, 8/17 1300: the MCS redevelops at 10 E.
Frame 4, 8/18 0000: the cloudy "front" of the MCS moves far ahead of the squall line, at 6 E.
Frame 5, 8/18 0900: The MCS crosses the radar circle at about 3 E.
Frame 6, 8/18 1700: the MCS interacts at about 3 W with new convection that is generated just ahead of the main squall line.
Frame 7, 8/19 0300: the MCS is a large squall line at 8 W.
Frame 8, 8/19 1330: the MCS at 15 W has very little convective activity compared with earlier times.
Frame 9, 8/19 1715: the MCS at 17 W continues over the ocean, becoming increasingly diffuse, with only a few adjacent lightning strokes at 20 W and 2015 UTC (not shown).

Chapter 6

Conclusions

6.1 Gust fronts

When we first set out to examine the propagation of gust fronts, it seemed that they were delicate features which usually mixed out soon after their creation. Our views on gust front distances were initially biased by radar observations, which were deceiving in their short range. The event documented in Figure 4-1 seemed unusually strong and extensive, propagating for > 1000 km. But a close look at the available satellite evidence shows that, to the contrary, it is common for these mesoscale events to extend to the synoptic scale: satellite imagery shows gust fronts propagating an average 750 km, much further than has been shown before for large numbers of events. The use of the infrared spectrum in particular has let us focus on haboobs, which are often ignored by conventional satellite meteorology because most satellite sensors are apt to detect upper tropospheric cirrus cloud instead of the gust front underneath (*Williams*, 2008).

Our systematic measurements of temperature drop and radar-measured gust front speed are used in Section 5.4.3 to validate the density-current model of gust front propagation, contributing evidence that the real world matches laboratory simulations and theoretical models. This knowledge could be useful in practice at locations with surface meteorology instruments but no radar, as is the case in most of West Africa: an observer with a thermometer who can estimate a haboob's height can predict its propagation speed and therefore when it will arrive at remote locations.

Our findings about diurnal convection frequency and the preferred geographic locations for convection, discussed in Sections 5.1 and 5.3, could be used to improve forecasting of when and where new convection will be generated along the arc of a gust front. Subtle events can be important; see Appendix B for discussion of a barely detectable event on 23 June which was not in our original tabulation, showed only a 1 C temperature drop and a relatively high minimum visibility, but nevertheless generated a large band of new convection.

6.2 Continuity in lightning stripes

The remarkably long-lived continuity of these stripes suggests that they possess some internal organization which maintains their continuity in speed and phase, despite occasional gaps that reflect reflect the decay of an MCS which expresses the stripe. Earlier work on squall line systems (e.g. *Fortune* (1980)) has shown, in agreement with our results, that groups of MCSs can propagate together for the kinds of long distances that are typical of our lightning stripe lengths. We contribute a new essential fact about these squall line systems, that their constituent MCSs have essentially the same speed and direction over many days.

One possible explanation for this continuity is that although convection is suppressed during certain hours of the day, gust front propagation is not. Tying together our study of gust fronts measured in radar and satellite images, and MCS systems studied in satellite and lightning images, this work additionally contributes an understanding of the mesoscale importance of gust fronts' contribution to new convection: in 63% (10 of 16) available cases of long lightning stripes studied in Section 5.7.3, gust fronts contributed to the redevelopment of convection in a squall line system after a pause represented as a gap in an otherwise continuous stripe of lightning Hovmoller activity.

The long continuity we have documented lightning stripes demands an explanation; "mesoscale" events in West Africa that propagate for > 2000–3000 km and >

2–4 days ought to be large enough to interact with synoptic-scale events. We have contributed an explanation of how these events can be common occurrences in the summer despite the conventional view that tropical waves (specifically AEWs) disrupt the westward propagation of squall line MCSs. We show that this view is not wrong: in the presence of an AEW, lightning stripes face a restricted lifespan and propagation distance, and no evidence has appeared in this study that a squall line propagates through the ridge of an AEW. Our work shows how the absence of AEWs for many weeks in August–September 2006 allowed many long-lived and long-line MCSs to propagate unabated.

We contribute two more useful ways of looking at lightning strokes: overlaid on SEVIRI infrared imagery, and counted with an automated Lagrangian method over the area of a squall line. The Lagrangian method is itself an important tool, because measuring lightning activity associated with an AEW may help in the prediction of Atlantic hurricane activity (*Price et al.*, 2007, 2009; *Chronis et al.*, 2007). Combining these two methods, we contribute systematic measurements of the extent of large squall lines (see Table 5.4 and Appendix B.2), demonstrating relationships among squall line length, propagation distance, and convective strength. We confirm that larger storms have stronger lightning activity (Figure 5-23) and that larger storms propagate longer distances (Figure 5-35), but find no particular evidence that larger, deeper storms propagate any faster than smaller storms (Figure 5-36).

6.3 Future work

Our work suggests several fruitful avenues for future research, much of in the form of collecting additional data or using our techniques on other data.

First, we could extend our study to a second season to learn additional information about typical behavior in the West African summer. Many features of weather in West Africa exhibit significant interannual variability (perhaps the most notable is the strength of the Atlantic hurricane season). The MIT radar was operated during summer 2007, and SEVIRI infrared imagery and potential vorticity analyses are also available for that season, so we could readily extend our radar and satellite analysis of gust fronts for an extra year. While ZEUS/STARNET lightning data are not available for 2007, we could potentially substitute data from the World Wide Lightning Location Network (WWLLN), with data available from 2004–2010; this network has fewer African receivers but might generate acceptable results.

Even in 2006, our analysis of AEW interaction with the long-lived MCSs visible in lightning stripes is not complete; we have focused on only about half the available cases. Additional study is needed, both to examine the synoptic-scale activity associated with other lightning stripes, and especially to determine whether there is any evidence that the gust fronts and MCSs we have observed contribute to AEW formation, as in the case study of *Berry and Thorncroft* (2005). The SEVIRI infrared imagery, combined with lightning stroke data, have provided the necessary tools to take a close look at an entire season to see to what extent MCSs contribute to the AEW.

Once aerosol is lofted by gust fronts and enters the atmosphere, it can propagate thousands of kilometers across the Atlantic Ocean and affect weather in North and South America. To better predict these effects, we need to be able to measure the quantity of dust which is lofted in West Africa and understand the processes that drive lofting. Understanding where dusty gust fronts begin and how far they propagate is a start, especially because our work with SEVIRI contributes a way to detect dust in regions partially obscured by upper-level cloud (rendering dust invisible to visible-spectrum satellite sensors). But further work is needed in quantifying the amount of dust lofted by a gust front and the amount that leaves the continent.

While we have given a new, long average propagation distance for gust fronts based on satellite measurements, this measurement is still a lower bound, constrained by the often subtle nature of a gust front's presence in satellite imagery. It is still not known just how far these events can go before they dissipate completely; future work, perhaps based on surface station or radar observations of the same event over > 1000 km, is needed if we are to understand how far a gust front can propagate and at what range it stops being a force capable of assisting new convection. More work is also needed to study the role of the gust front layer thickness in thwarting the mixing process which gradually eliminates the density difference that drives a gust front.

Appendix A

Code

This appendix contains useful code used in the generation of this thesis which was too cumbersome to include inline.

A.1 Lightning Hovmoller diagrams

This Matlab code takes input files in the format of ZEUS lightning stroke data, integrates lightning from 8–18 N latitude into “cells” of size 15 minutes by 1 degree longitude, and produces Hovmoller diagrams showing five days of data at a time (since there are 61 days total, the last file for September shows six days of data instead). The files are formatted so that the mean lightning stripe speed (about 16 m/s) has about a 45 degree angle.

```
%Lightning Hovmoller intersections for August, September
%Matlab generator:
%cd c:\users\mherdeg\documents\MATLAB\zeus\

minlat = 8;
maxlat = 18;
minlong = −40;
maxlong = 60;
files = [’xaa’; ’xab’; ’xac’; ’xad’; ’xae’; ’xaf’;
```

```
        'xag'; 'xah'; 'xai'; 'xaj'; 'xak'; 'xal'];

dayranges = [
 1,31+30, 1,12;
];

hov = [];
for j=1:size(dayranges,1),
 filestoread = files(dayranges(j,3):dayranges(j,4), :);
 numberofdays = dayranges(j,2) - dayranges(j,1) + 1;
 hov = zeros(101, 96*numberofdays); % 4 pixels per hour
 minday = dayranges(j,1);
 maxday = dayranges(j,2);
 for i = 1:size(filestoread,1),
  xae = dlmread(filestoread(i,:));
  days = (xae(:,1) - 8) * 31 + xae(:,2);
  longs = xae(find( days >= minday & days <= maxday &
   minlat < xae(:,4) & xae(:,4) < maxlat &
   xae(:,5) > minlong & xae(:,5) < maxlong),5);
  times = xae(find( days >= minday & days <= maxday &
   minlat < xae(:,4) & xae(:,4) < maxlat &
   xae(:,5) > minlong & xae(:,5) < maxlong),1:3);
  for K=1:size(longs, 1),
   x = round(longs(K)) - minlong + 1;
   add = 0;
   add = times(K,1) - 8;
   y = add*96*31 + (times(K,2)-minday)*96
    + floor(times(K,3)*1/15)+1;
   if y<0,
    y=y+2976;
```

```
    end
    hov(x,y) = hov(x,y) + 1;
   end
  pack
  end
  dlmwrite(sprintf('%d-hov.txt', j), hov);
end

numbers = [];
for i=1:31,
  numbers(i,:) = sprintf('%.2d', i);
end
for i=1:31,
  numbers(i+31,:) = sprintf('%.2d', i);
end

numbers = char(numbers);

newranges = [
  1,5;
  6,10;
  11,15;
  16,20;
  21,25;
  26,30;
  31,35;
  36,40;
  41,45;
  46,50;
  51,55;
```

```
 56,61];

for j=1:size(newranges, 1)
 numberofdays = newranges(j,2) - newranges(j,1) + 1;
 minday = newranges(j,1);
 maxday = newranges(j,2);
 minpix = (minday-1)*96+1;
 maxpix = maxday*96;

 hov = dlmread(sprintf('%d-hov.txt', 1));
 imagesc(minlong:maxlong, 96*numberofdays:-24:1,
  log(hov(:,minpix:maxpix)')/log(10));
 colorbar;
 set(gca, 'YTick', [0:96:96*numberofdays]);
 set(gca, 'XTick', minlong:10:maxlong);
 set(gca, 'YTickLabel', flipud(numbers(minday:maxday+1, :)))
 temp = sprintf('%d-%d', minlat, maxlat);
 title(['Hovmoller ',temp,'N, logarithm of number of sferics']);
 xlabel('Longitude');
 ylabel('Days of August 2006 (hourly accumulation)');
 if j == 7,
  ylabel('Days of August and September 2006 (hourly accumulation)');
 end
 if j > 7,
  ylabel('Days of September 2006 (hourly accumulation)');
 end
 hold on
 set(gcf, 'PaperPositionMode', 'auto');
 saveas(gcf, sprintf('hov-%d.png', j));
 set(gcf, 'PaperPositionMode', 'Manual');
```

```
 set(gcf, 'PaperSize', [12 20]);
 frame=getframe(gcf);
 [X,map]=frame2im(frame);
 imwrite(X, sprintf('hov45-%d.png', j));
 hold off
end
```

A.2 SEVIRI dust product projection

A.2.1 Coordinates to pixels

This Matlab code converts latitude, longitude coordinates into pixels on a SEVIRI dust product image using the EUMETSAT geostationary satellite projection. It is useful when mapping lightning strokes onto the SEVIRI dust product.

```
function [x,y] = sevirify(LAT,LON)
% sevirify(LAT,LON) Produces cropped SEVIRI dust product image
%                   pixels from an input latitude and longitude,
%                   using the "geostationary satellite at 0
%                   longitude" projection for the Meteosat
%                   MSG satellite.


% The math for this algorithm comes from "Coordination Group for
% Meteorological Satellites // LRIT/HRIT Global Specification"
% page 24, to produce intermediate x,y values for a given lat/long.

sublon = 0;
clat = atand(0.993243 * tand(LAT));
rl = 6356.5838 / sqrt(1 - .00675701*cosd(clat)*cosd(clat));
r1 = 42164 - rl * cosd(clat) * cosd(LON - sublon);
```

```
r2 = −rl*cosd(clat)*sind(LON−sublon);
r3 = rl*sind(clat);
rn = sqrt(r1*r1 + r2*r2 + r3*r3);
unscaledx = atand(−r2/r1);
unscaledy = asind(−r3/rn);

% y axis:::
%30 (0 px) => -4.9457
%-5 (607 px) => 0.8834
%
%0 image => -4.9457 unscaled
%607 image => 0.8834 unscaled
%sample value:
%unscaledy = 0.8834

%x axis:::
%-25 (0 px) => -4.2371
%25 (883 px) => 4.2371
%sample value:
%unscaledx = -4.2371
x = round((unscaledx + 4.2371) * 883/(2*4.2371));
y = round((unscaledy + 4.9457) * 607/(4.9457+.8834));
```

A.2.2 Pixels to coordinates

This Matlab code converts pixels from a SEVIRI dust product image to latitude, longitude coordinates using the EUMETSAT geostationary satellite projection. It is useful when measuring the “true” latitude or longitude represented by a location on the SEVIRI dust product (although the difference between this and an equirectangular projection is negligible for latitudes below about 20 N).

```
function [lat,lon] = reverse_sevirify(x,y)
% Converts SEVIRI image pixels into latitude & longitude values.

% scale from SEVIRI px into raw intermediate px.
% source:
% y axis:::
%30 (0 px) => -4.9457
%-5 (607 px) => 0.8834
%0 image => -4.9457 unscaled
%607 image => 0.8834 unscaled
%x axis:::
%-25 (0 px) => -4.2371
%25 (883 px) => 4.2371
%x = round((unscaledx + 4.2371) * 883/(2*4.2371));
%y = round((unscaledy + 4.9457) * 607/(4.9457+.8834));

x = 0.0095970554926387315968289920724802*x − 4.2371;
y = 0.0096031301482701812191103789126853*y − 4.9457;

sd = sqrt( (42164*cosd(x)*cosd(y))^2 −
           1737121856*(cosd(y)^2 + 1.006803*sind(y)^2) );
sn = (42164*cosd(x)*cosd(y)−sd) /
     (cosd(y)*cosd(y)+1.006803*sind(y)*sind(y));
s1 = 42164 − sn*cosd(x)*cosd(y);
s2 = sn*sind(x)*cosd(y);
s3 = −sn*sind(y);
sxy = sqrt(s1*s1+s2*s2);
sub_lon = 0;
lon = atand(s2/s1) + sub_lon;
lat = atand(1.006803*s3/sxy);
```

A.3 Lagrangian analysis of MCS lightning strokes

This Matlab code converts lightning stroke data in the ZEUS/STARNET format, along with information about MCS start and end times and gust front launch times, into images showing the Lagrangian lightning counts during the lifespan of each MCS and Matlab figures containing the resulting data.

```
base = 'lightning-augsept\';
startvecs = [
[2006 08 02 15 15 00];[2006 08 05 11 30 00];[2006 08 09 12 45 00];
[2006 08 16 11 00 00];[2006 08 17 10 30 00];[2006 08 21 13 15 00];
[2006 08 25 14 30 00];[2006 08 27 07 30 00];[2006 08 27 07 15 00];
[2006 09 03 03 15 00];[2006 09 04 10 30 00];[2006 09 07 14 30 00];
[2006 09 12 02 30 00];[2006 09 13 14 15 00];[2006 09 18 14 00 00];
[2006 09 23 14 15 00];
];

approxlengths = [48;36;75;36;63;54;48;55;107;29;51;43;55;35;46;36;];
launchoffsets = [9;38;109;7;21;16;78;29;231;46;19;7;19;39;15;14;];
niameyoffsets = [90.3332;82;154.4;91.8;88.7333;56.3333;96.6;75.9332;
                 289.267;45.8668;91.4667;60.6667;50.4668;69.2;47.6;51.7333;];
longhigh = [10;15;10;17;13;10;13;13;25;7;15;12;12;13;7;10;];
longlow = [-3;-10;-8;-15;-20;-10;-12;-15;-20;
           -10;-15;-13;-20;-5;-12;-10;];
lathigh = [20;20;20;20;20;17;17;18;17;20;22;20;22;22;20;22;];
latlow = [12;10;10;10;10;12;7;7;7;12;17;13;10;15;10;15;];
fifteenvec = [0 0 0 0 15 0];
counts = [];
for j=1:16,
 startvec = startvecs(j,:);
 for i=1:4*approxlengths(j),
```

```
 right = datenum(startvec);
 foldername = datestr(right, 29);
 filename = datestr(right, 'yyyy-mm-dd_HHMM');
 openme = strcat(base, foldername, '\', filename, '.dat');
 rightfile = dlmread(openme);
 chosenleft = [];
 chosenright = rightfile(find(rightfile(:,8) > latlow(j)
              & rightfile(:,8) < lathigh(j) & rightfile(:,9) < longhigh(j)
              & rightfile(:,9) > longlow(j)), 8:9);
 lat = [chosenright(:,1)];
 long = [chosenright(:,2)];
 counts(j,i) = size(lat, 1);
 startvec = startvec + fifteenvec;
end
xes = [0:4*approxlengths(j)-1]/4 + startvecs(j,4);
launchoffset = launchoffsets(j)/4 + startvecs(j,4);
niameyoffset = niameyoffsets(j)/4 + startvecs(j,4);
plot(xes,counts(j,1:4*approxlengths(j)))
set(gca, 'XTick', 0:4:4*approxlengths(j));
xlabel(['UTC hours beginning at ', datestr(datenum(startvecs(j,:)))]);
vline(launchoffset, 'r');
vline(niameyoffset, 'b');
ylabel('Number of flashes per 15 minutes');
ticks = 0:4:4*approxlengths(j) + startvecs(j,4);
xlabels = [];
for i=1:size(ticks,2);
 s = sprintf('%02.f', round(mod(ticks(i), 24)));
 xlabels = strvcat(xlabels, s);
end
set(gca, 'XTickLabel', xlabels);
```

```
 saveas(gca,sprintf('%d.png', j));
 saveas(gca,sprintf('%d.fig', j));
end
```

Appendix B

Additional data

This chapter presents supplementary information on the events we have documented.

B.1 Gust front measurements

Table B.1 presents measurements of the gust fronts observed crossing the Niamey site. In addition to presenting the information from Table 5.1, it adds two quantities measured by the ARM Mobile Facility: horizontal visibility (measured in km), whose distribution is discussed in Section 5.2, and maximum surface wind speed. (The Niamey ARM Mobile Facility was at altitude 205 m, with the wind monitor mounted 3 m above the ground at the facility.)

This table includes a 23 June event not recorded in our original tabulation of gust fronts. This event is discussed further in Section 5.4.

Date of GF radar site crossing (2006, UTC)	Temp drop (C)	Radar: 10-minute speed (m/s)	SEVIRI: observed duration (hr)	SEVIRI: observed distance (km)	SEVIRI: average speed (m/s)	Min 1-min vis (km)	Max wind speed (m/s)
1 June 16:58	3.3	-	23	730	8.8	479	5.9
2 June 17:16	11.6	-	13	340	7.2	142	17
4 June 17:37	3.7	-	-	-	-	531	7.6
7 June 20:04	10.8	-	13	240	5.1	755	14
15 June 02:12	3.9	-	17	420	10.2	265	8.9
17 June 22:15	12.2	-	12	700	11.8	29	24
21 June 20:43	4.8	-	16	590	15.8	630	11
23 June 09:55	1.2	-	42	1300	8.7	8000	4.5
27 June 19:10	5.2	-	-	-	-	1276	6.6
2 July 00:06	5	14.3	15	660	10.7	512	15
5 July 00:22	2.5	12.1	21	1180	12	430	5
6 July 23:13	4.4	12.6	15	930	13.3	1947	4.7
9 July 00:07	4.4	11.4	-	-	-	515	9.2
10 July 16:40	6.4	-	16	600	15.8	2376	8.1
11 July 18:45	3.2	11.6	7.6	160	19.1	1299	13
12 July 18:43	3.6	-	12	240	21.7	765	4.7
14 July 05:12	7.1	21.3	18	760	12.8	366	13
15 July 04:04	2.9	-	23	1120	14.8	8148	7.4
17 July 06:42	6.7	9.38	24	1360	13.7	1306	11
19 July 05:13	3.9	19.4	12	840	22.4	969	11
20 July 18:38	3.6	-	-	-	-	3970	3.2
22 July 09:43	5.7	18	4.3	320	19.6	911	12
25 July 07:02	2.6	12.6	-	-	-	5114	6.1
31 July 09:24	3.2	14.2	8.5	670	16.8	1848	6.7
3 Aug. 13:49	6.5	20.2	20	920	9.5	693	9.5
6 Aug. 08:00	2.2	12.4	-	-	-	2300	6.7
11 Aug. 03:21	2.3	16.6	-	-	-	2616	6.6
17 Aug. 09:56	2.6	-	17	920	14.8	11546	4.9
18 Aug. 08:40	5.8	15.4	17	820	14.1	1478	7.7
22 Aug. 03:19	3.2	-	24	1920	15.7	1233	14
26 Aug. 14:39	8	12.7	21	1470	14.9	4347	7.9
28 Aug. 02:28	6.5	16.6	24	1450	15.1	3279	13
30 Aug. 07:34	3.2	15.2	8.4	290	7	5635	8.2
3 Sept. 14:43	5.1	16.4	24	1280	17	11493	5
5 Sept. 09:22	6.1	13.3	22	1090	17.2	1553	7
8 Sept. 05:40	3.6	8.11	24	1350	6	1426	9
12 Sept. 15:70	10.3	-	-	-	-	1025	11
14 Sept. 07:32	4.3	-	16	860	5.6	1809	12
19 Sept. 01:53	6.8	-	20	1060	20.5	2041	8
24 Sept. 03:10	6.3	21.4	-	-	-	1285	14
30 Sept. 08:28	2.9	-	-	-	-	7204	5.8

Table B.1: Gust front characteristics measured during summer 2006. See description in Appendix B.1.

Niamey crossing date	Time of maximum length (UTC)	Length (km)
11 Aug.	1745	1330
14 Aug.	1530	1040
18 Aug.	1530 (17 Aug.)	1170
22 Aug.	0930	1040
28 Aug.	2045 (27 Aug.)	1010
30 Aug.	0930	1430
31 Aug.	2015	660
3 Aug.	2115	770
6 Aug.	0815	530
10 Sept.	1700	320
12 Sept.	0100 (13 Sept.)	1330
14 Sept.	0115	560
19 Sept.	0245	720
24 Sept.	2130 (23 Sept.)	1250
5 Sept.	1700	1250
8 Sept.	0500	820

Table B.2: Maximum length in km for all squall lines that crossed the MIT radar in Niamey in August–September 2006, as measured by frame-by-frame analysis of ZEUS/STARNET lightning data overlaid on SEVIRI infrared dust imagery for all times from the MCS initiation until the MCS demise (end of all lightning). The time of maximum length is on the same day the front crossed Niamey unless otherwise specified.

B.2 Squall line maximum lengths

Table B.2 gives the maximum length (in km) of squall lines which cross the MIT radar, as measured by frame-by-frame analysis of ZEUS/STARNET lightning data overlaid on SEVIRI infrared dust imagery for all times from the MCS initiation until the MCS demise (end of all lightning). The date indicates when the squall line crossed the MIT radar.

Squall lines which persist for more than 24 hours are generally documented based on the lightning stripes they generate in Table 5.4.

B.3 Lightning stripe Hovmoller diagrams

The figures in this section are high-resolution lightning Hovmoller diagrams for August and September 2006, showing five or six days at a time with cell size 15 minutes by 1 degree longitude. The diagrams were sized so that a 45 degree angle on these plots represents a phase speed of approximately 16 m/s, the mean speed of lightning stripes whose speed distribution is in Figure 5-30. For more information on the generation of these figures, see Section 4.4.1.

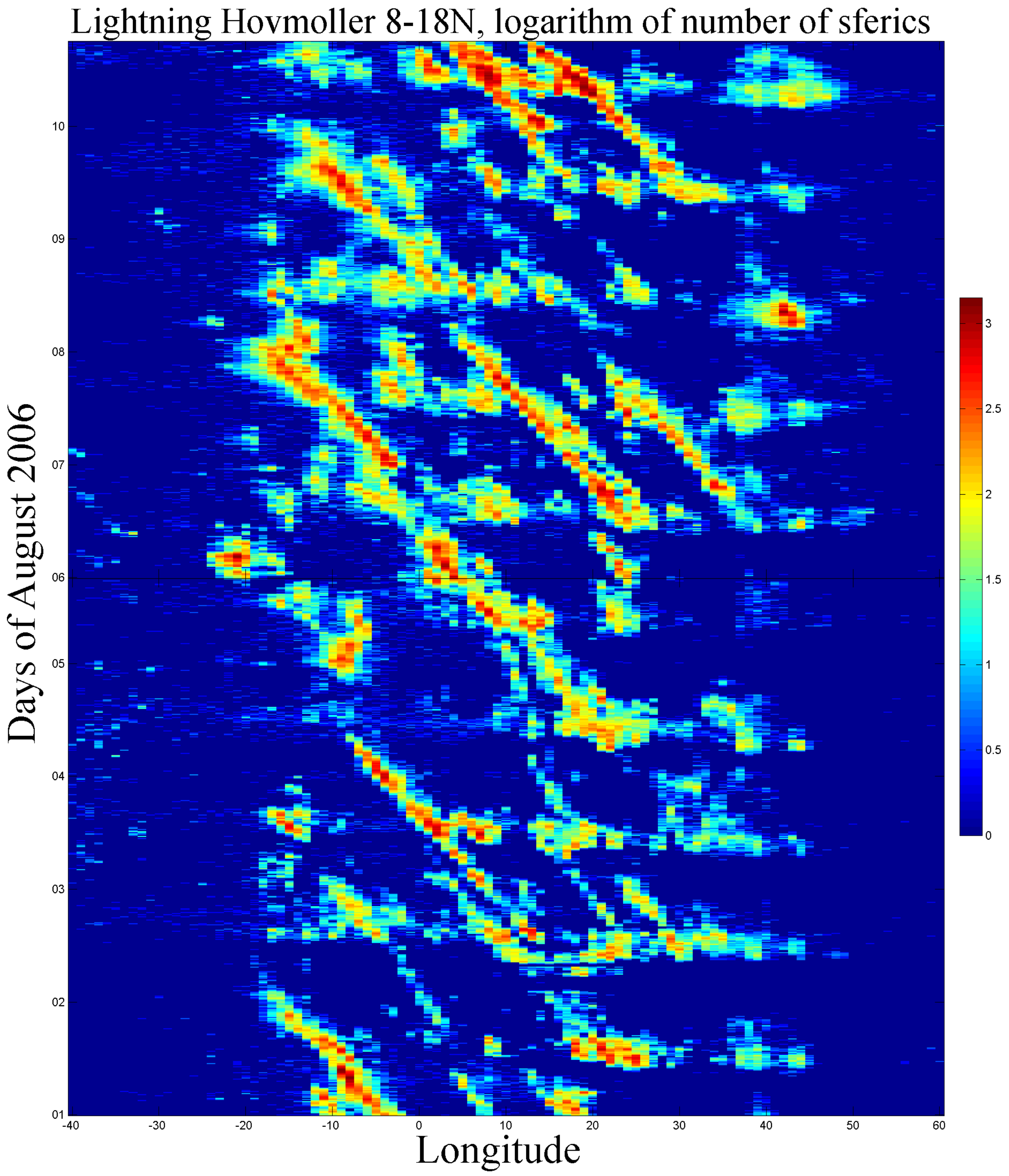
Lightning Hovmoller 8-18N, logarithm of number of sferics
Days of August 2006
10
09
08
07
06
05
04
03
02
01
-40
-30
-20
-10
0
10
20
30
40
50
60
Longitude
3
2.5
2
1.5
1
0.5
0

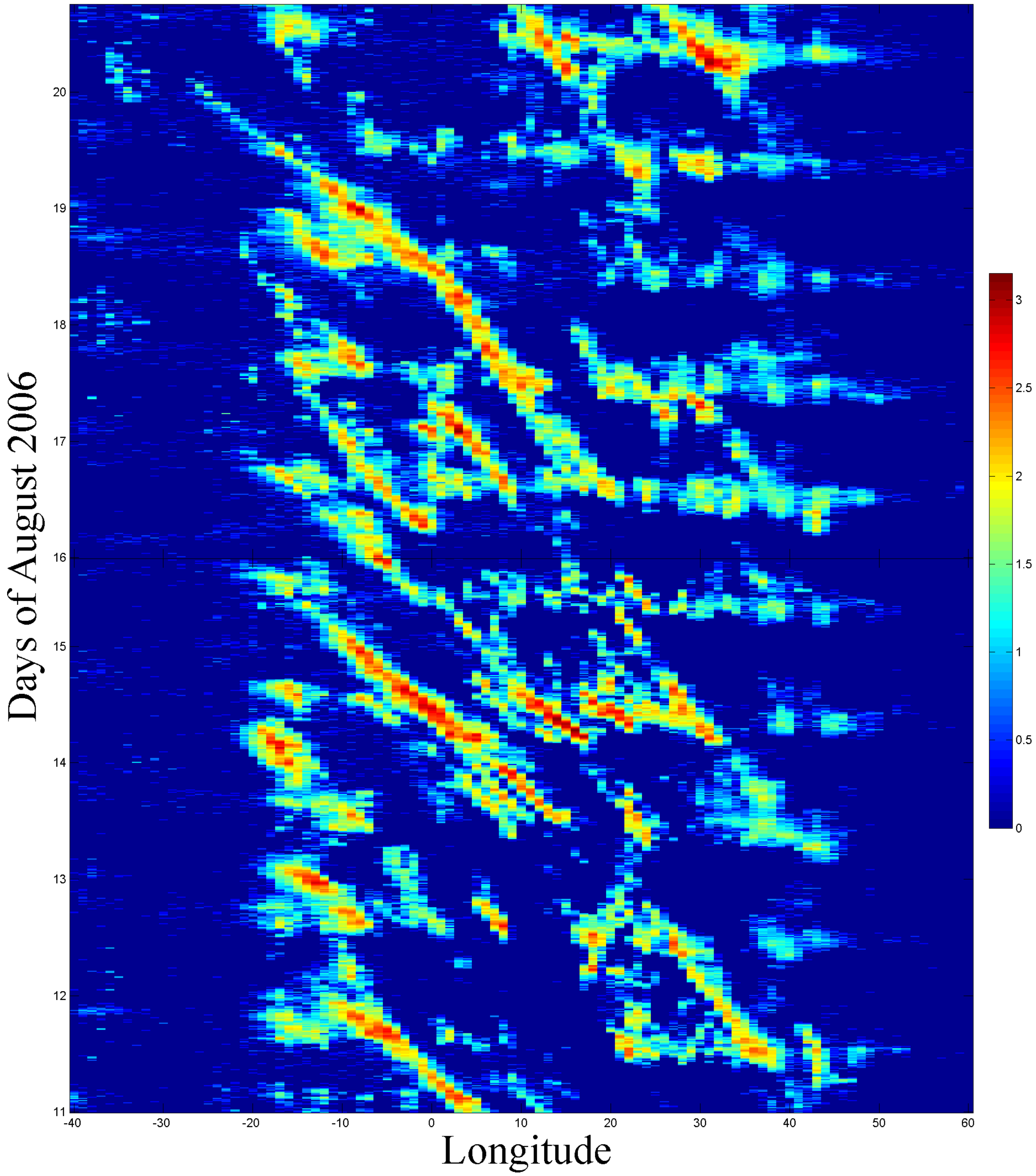

Lightning Hovmoller 8-18N, logarithm of number of sferics

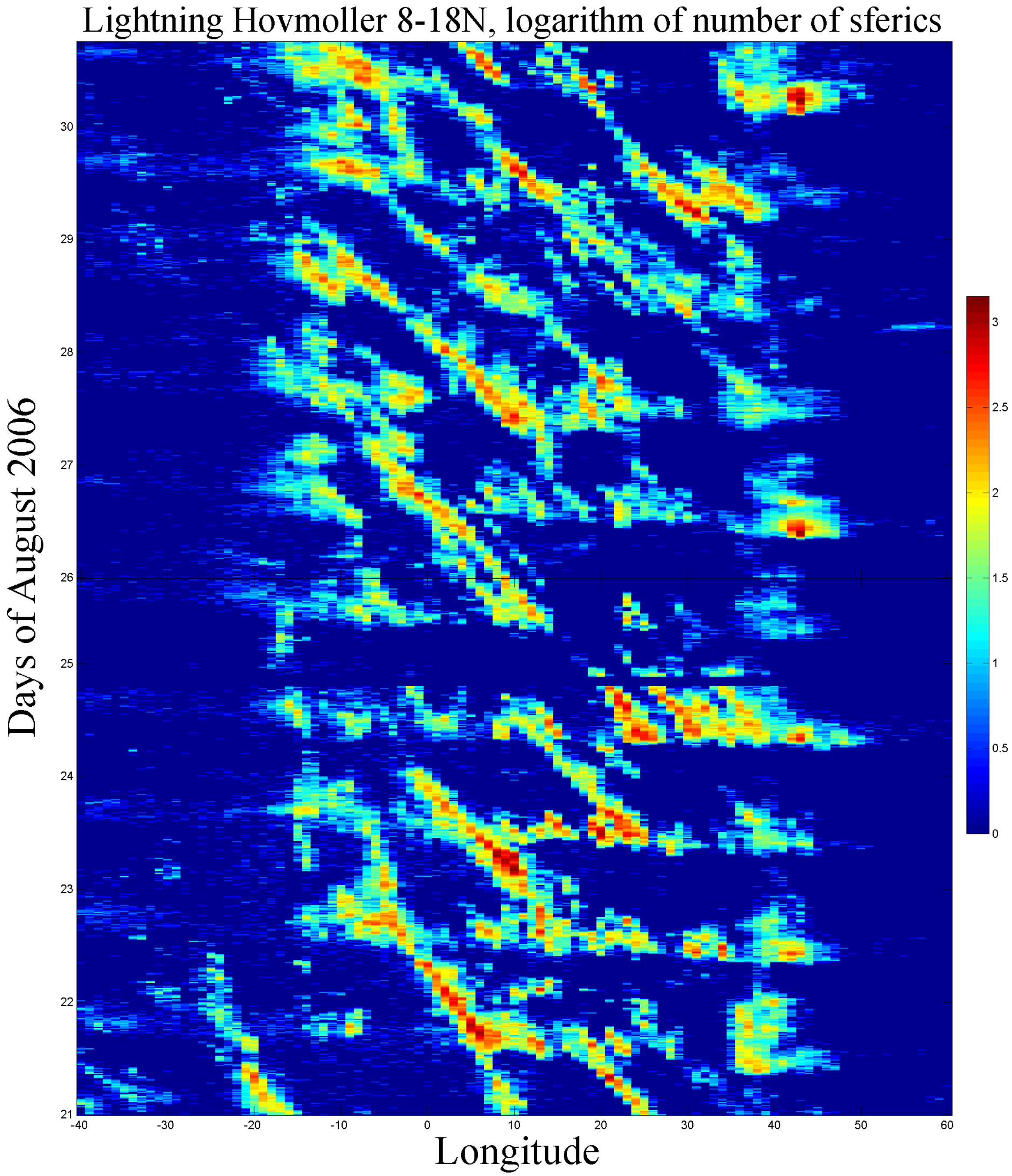
Lightning Hovmoller 8-18N, logarithm of number of sferics
Days of August 2006
30
29
28
27
26
25
24
23
22
21
Longitude
-40
-30
-20
-10
0
10
20
30
40
50
60
3
2.5
2
1.5
1
0.5
0

Lightning Hovmoller 8-18N, logarithm of number of sferics

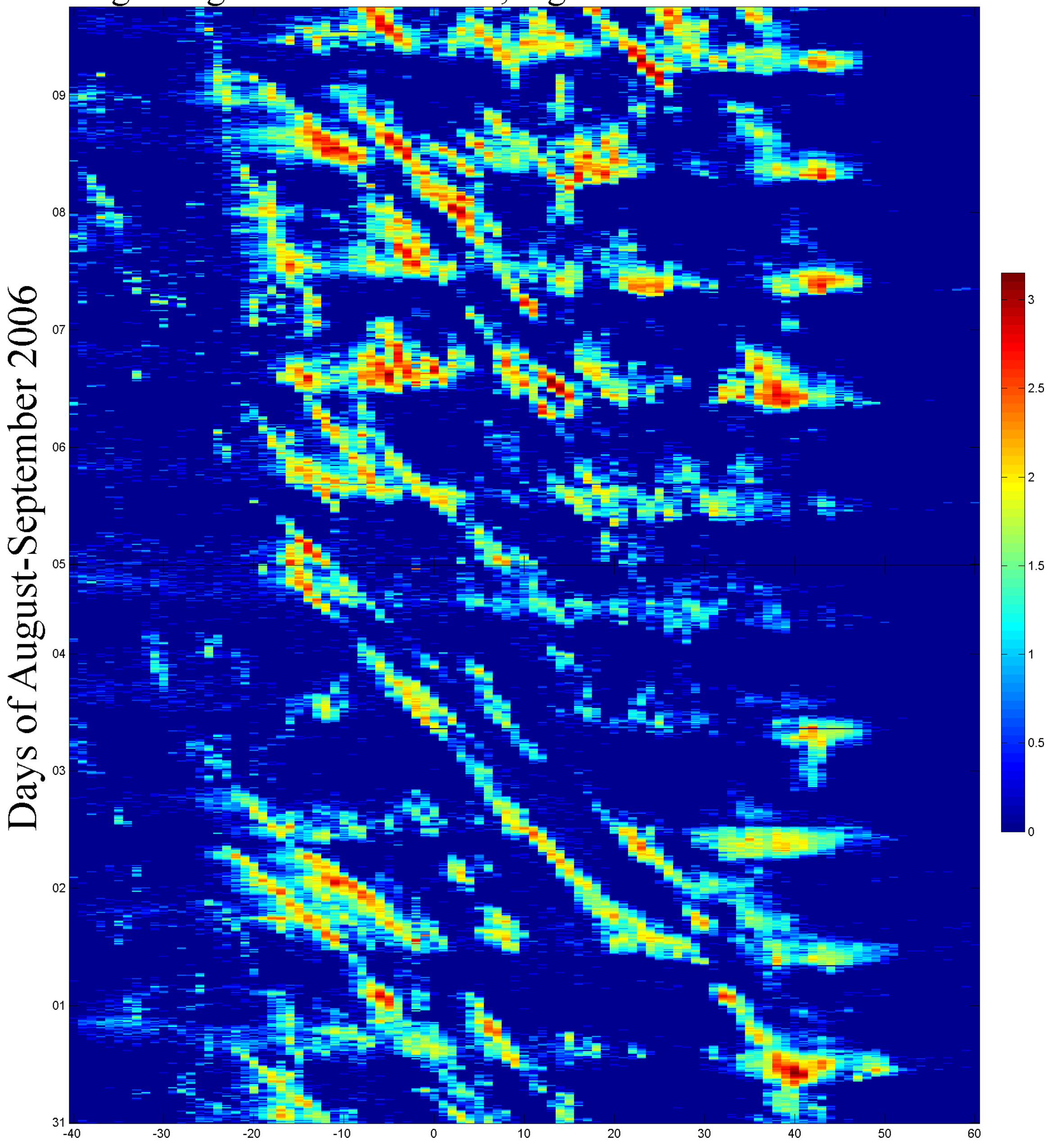

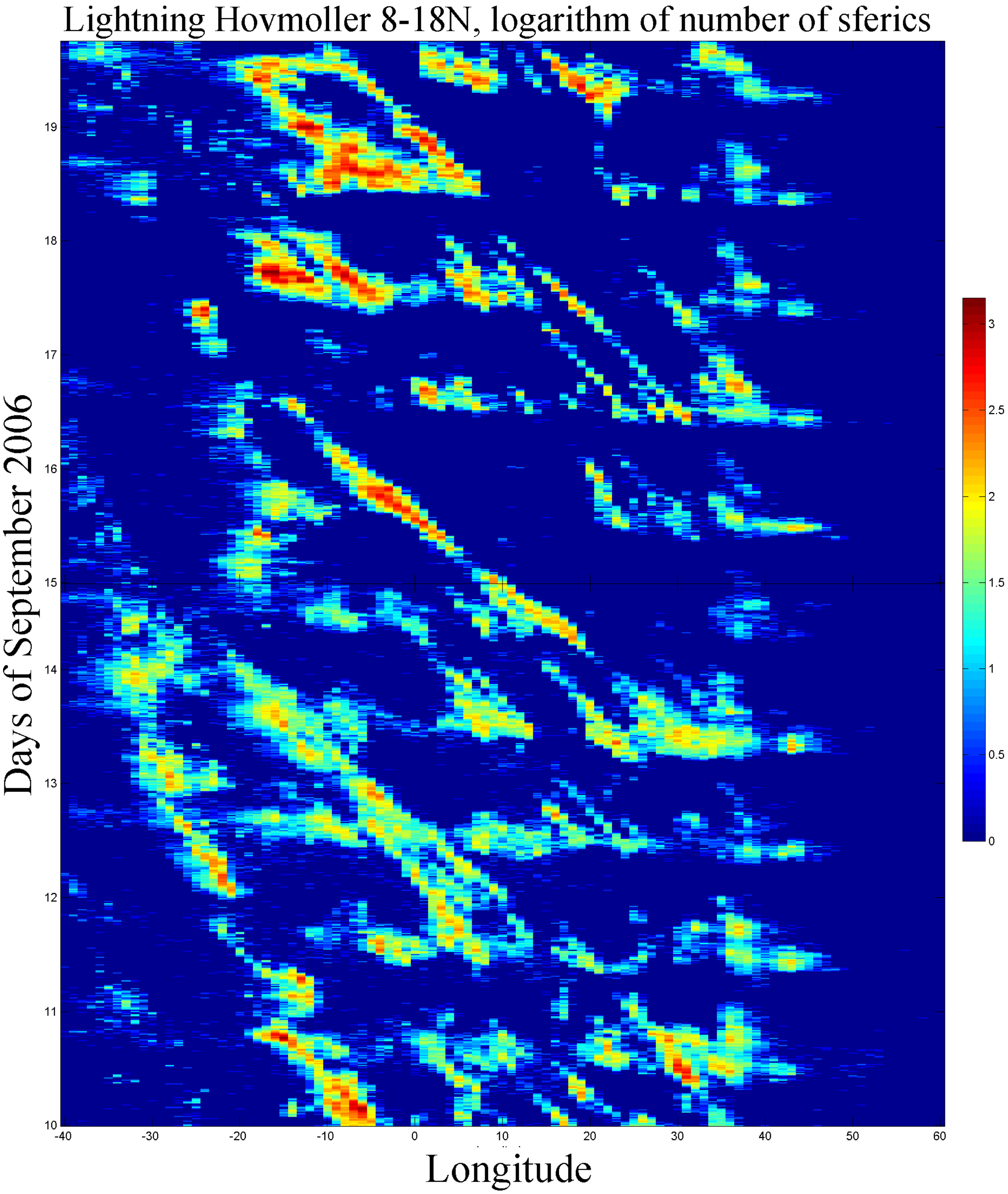

Lightning Hovmoller 8-18N, logarithm of number of sferics

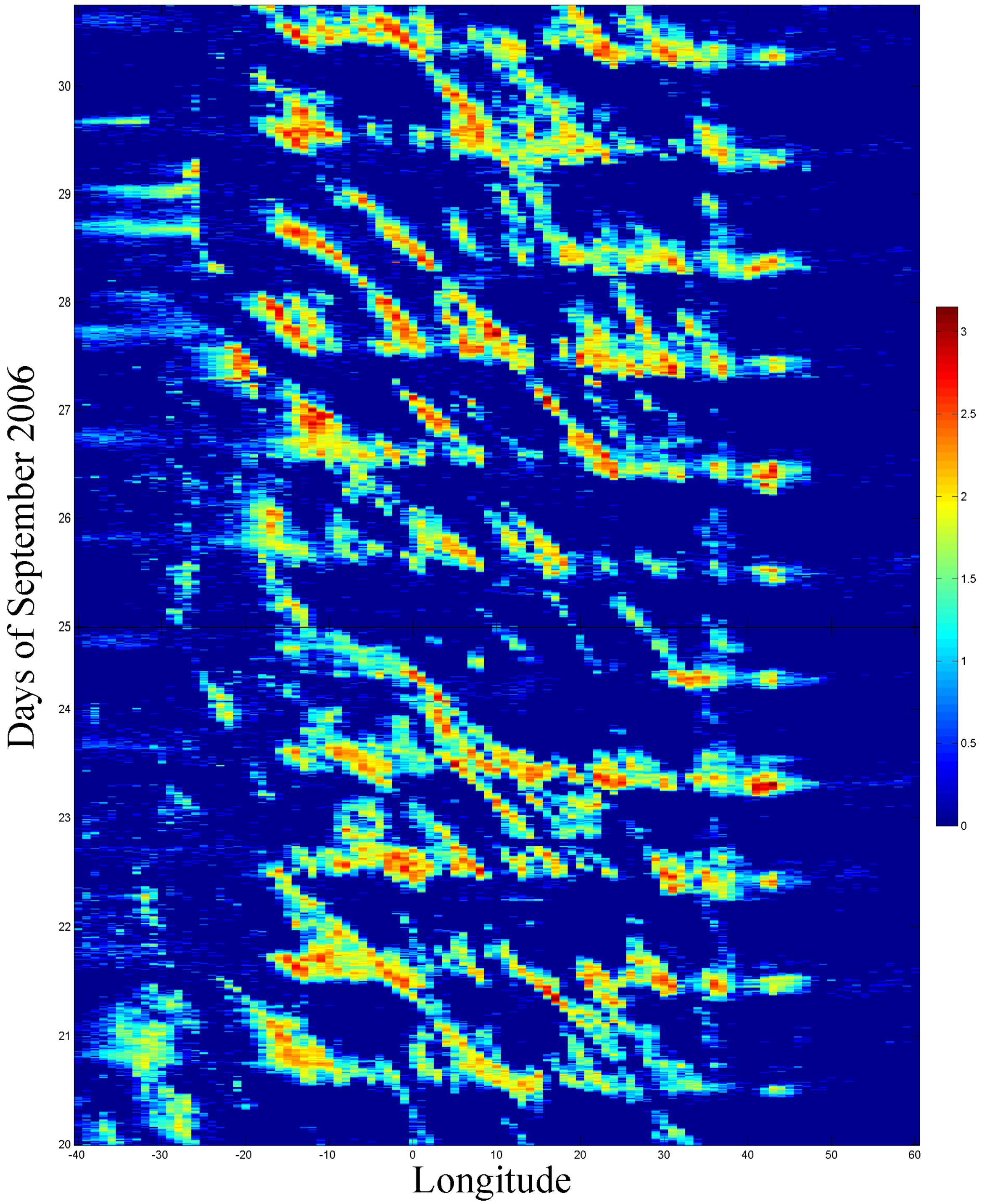

Lightning Hovmoller 8-18N, logarithm of number of sferics

Bibliography

Ackerman, T., and G. Stokes (2003), The atmospheric radiation measurement program, *Physics Today*, *56*(1), 38–44.

Anuforom, A. (2007), Spatial distribution and temporal variability of Harmattan dust haze in sub-Sahel West Africa, *Atmospheric Environment*, *41*(39), 9079–9090.

Benjamin, T. (1968), Gravity curent and related phenomena, *J. Fluid Mechanics*, *31*, 209–248.

Berry, G., and C. Thorncroft (2005), Case study of an intense African easterly wave, *Monthly Weather Review*, *133*(4), 752–766.

Bou Karam, D., C. Flamant, P. Tulet, M. Todd, J. Pelon, and E. Williams (2009), Dry cyclogenesis and dust mobilization in the Inter Tropical Discontinuity of the West African Monsoon: A case study, *J. Geophys. Res*, *114*.

Bou Karam, D., E. Williams, M. McGraw-Herdeg, M. Janiga, J. Cuesta, C. Flamant, J. Pelon, and C. Thorncroft (2010), Dusty gust fronts at synoptic scale, initiated and maintained by moist convection over the Sahara desert, in *2nd Symposium on Aerosol-Cloud-Climate Interactions*, Madison, WI.

Byers, H., and R. Braham (1949), *The Thunderstorm Project, 287 pp*, 287 pp., U.S. Weather Bureau.

Byers, H. R. (1949), Structure and dynamics of the thunderstorm, *Science*, *110*(2856), 291–294.

Cakmur, R., R. Miller, and O. Torres (2004), Incorporating the effect of small-scale circulations upon dust emission in an atmospheric general circulation model, *Journal of Geophysical Research*, *109*(D7), D07,201.

Charba, J. (1974), Application of gravity current model to analysis of squall-line gust front, *Monthly Weather Review*, *102*, 140.

Chong, M. (2009), The 11 August 2006 squall-line system as observed from MIT Doppler radar during the AMMA SOP, *Quarterly Journal of the Royal Meteorological Society*, *136*(S1), 209–226.

Chong, M., P. Amayenc, G. Scialom, and J. Testud (1987), A tropical squall line observed during the COPT 81 experiment in West Africa. Part I: Kinematic structure inferred from dual-Doppler radar data, *Mon. Wea. Rev*, *115*, 670–694.

Chronis, T., and E. Anagnostou (2003), Error analysis for a long-range lightning monitoring network of ground-based receivers in Europe, *J. Geophys. Res*, *108*(D24), 4779.

Chronis, T., E. Anagnostou, and T. Dinku (2004), High-frequency estimation of rainfall from thunderstorms via satellite infrared and a long-range lightning network in Europe, *Quarterly Journal of the Royal Meteorological Society*, *130*(599), 1555–1574.

Chronis, T., E. Williams, E. Anagnostou, and W. Petersen (2007), African lightning: indicator of tropical Atlantic cyclone formation, *EOS Transactions*, *88*, 397–398.

Cornforth, R., B. Hoskins, and C. Thorncroft (2009), The impact of moist processes on the African easterly jet-African easterly wave system, *Quarterly Journal of the Royal Meteorological Society*, *135*(641), 894–913.

Crook, N. A., R. E. Carbone, M. W. Moncrieff, and J. W. Conway (1990), The generation and propagation of a nocturnal squall line. part ii: Numerical simulations, *Monthly Weather Review*, *118*(1), 50–66.

Diaz, J., F. Expósito, C. Torres, F. Herrera, J. Prospero, and M. Romero (2001), Radiative properties of aerosols in Saharan dust outbreaks using ground-based and satellite data- Applications to radiative forcing, *Journal of geophysical research*, *106*(D16), 18,304–18,416.

Didden, N., and T. Maxworthy (1982), The viscous spreading of plane and axisymmetric gravity currents, *Journal of Fluid Mechanics*, *121*, 27–42.

Diedhiou, A., S. Janicot, A. Viltard, P. De Felice, and H. Laurent (1999), Easterly wave regimes and associated convection over West Africa and tropical Atlantic: results from the NCEP/NCAR and ECMWF reanalyses, *Climate Dynamics*, *15*(11), 795–822.

Donovan, M., E. Williams, C. Kessinger, G. Blackburn, P. Herzegh, R. Bankert, S. Miller, and F. Mosher (2008), The identification and verification of hazardous convective cells over oceans using visible and infrared satellite observations, *Journal of Applied Meteorology*, *47*(1), 164–184.

Droegemeier, K., and R. Wilhelmson (1987), Numerical simulation of thunderstorm outflow dynamics. Part I: Outflow sensitivity experiments and turbulence dynamics, *J. Atmos. Sci*, *44*(8), 1180–1210.

Engholm, C., E. Williams, and R. Dole (1990), Meteorological and Electrical Conditions Associated with Positive Cloud-to-Ground Lightning, *Monthly Weather Review*, *118*, 470.

Ette, A. (1971), The effect of the harmattan dust on atmospheric electric parameters, *Journal of Atmospheric and Terrestrial Physics*, *33*(2), 295–300.

Fan, J., R. Zhang, G. Li, and W. Tao (2007), Effects of aerosols and relative humidity on cumulus clouds, *Journal of Geophysical Research-Atmospheres*, *112*(D14), D14,204.

Fink, A., and A. Reiner (2003), Spatio-temporal variability of the relation between African Easterly Waves and West African Squall Lines in 1998 and 1999, *J. Geophys. Res*, *108*(D11), 4332.

Flamant, C., J. Chaboureau, D. Parker, C. Taylor, J. Cammas, O. Bock, F. Timouk, and J. Pelon (2007), Airborne observations of the impact of a convective system on the planetary boundary layer thermodynamics and aerosol distribution in the inter-tropical discontinuity region of the West African Monsoon, *Quarterly Journal of the Royal Meteorological Society*, *133*(626), 1175–1190.

Flamant, C., P. Knippertz, D. Parker, J. Chaboureau, C. Lavaysse, A. Agusti-Panareda, and L. Kergoat (2009), The impact of a mesoscale convective system cold pool on the northward propagation of the intertropical discontinuity over West Africa, *QJR Meteorol. Soc*, *135*, 139–159.

Fortune, M. (1980), Properties of African squall lines inferred from time-lapse satellite imagery, *Monthly Weather Review*, *108*(2), 153–168.

Franklin, J., and D. Brown (2008), Atlantic hurricane season of 2006, *Monthly Weather Review*, *136*(3), 1174–1200.

Fujita, T. (1986), *DFW Microburst in August 2, 1985, 154 pp*, University of Chicago Press.

Fujita, T., et al. (1990), Downbursts: meteorological features and wind field characteristics, *Journal of Wind Engineering and Industrial Aerodynamics*, *36*, 75–86.

Geotis, S. (1978), Comparison of Reflectivity Measurements by Radar and by Disdrometer, *Journal of Applied Meteorology*, *17*(9).

Houze Jr, R., S. Geotis, F. Marks Jr, and A. West (1981), Winter monsoon convection in the vicinity of North Borneo. Part I: Structure and time variation of the clouds and precipitation, *Mon. Wea. Rev*, *109*, 1595–1614.

Hsieh, J., and K. Cook (2005), Generation of African easterly wave disturbances: Relationship to the African easterly jet, *Monthly Weather Review*, *133*(5), 1311–1327.

Huppert, H. (1982), The propagation of two-dimensional and axisymmetric viscous gravity currents over a rigid horizontal surface, *Journal of Fluid Mechanics*, *121*, 43–58.

Janiga, M. (2010), personal communication.

Janiga, M., C. Thorncroft, and E. Williams (2009), The environment and characteristics of convective events over Niamey, Niger: AMMA SOP2 observations and climatological context, in *3rd AMMA Conference*, Ouagadougou, Burkina Faso.

Khain, A., and A. Pokrovsky (2004), Simulation of effects of atmospheric aerosols on deep turbulent convective clouds using a spectral microphysics mixed-phase cumulus cloud model. Part II: Sensitivity study, *Journal of the Atmospheric Sciences*, *61*(24), 2983–3001.

Kiladis, G., C. Thorncroft, and N. Hall (2006), Three-dimensional structure and dynamics of African easterly waves. Part I: Observations, *Journal of the Atmospheric Sciences*, *63*(9), 2212–2230.

Knippertz, P., J. Trentmann, and A. Seifert (2009), High-resolution simulations of convective cold pools over the northwestern Sahara, *Journal of Geophysical Research*, *114*(D8), D08,110.

Laing, A., R. Carbone, V. Levizzani, and J. Tuttle (2008), The propagation and diurnal cycles of deep convection in northern tropical Africa, *Quarterly Journal of the Royal Meteorological Society*, *134*(630), 93–110.

Lensky, I., and D. Rosenfeld (2008), Clouds-Aerosols-Precipitation Satellite Analysis Tool (CAPSAT), *Atmos. Chem. Phys*, *8*, 6739–6753.

Lothon, M., B. Campistron, M. Chong, F. Couvreux, G. F., C. Rio, and E. Williams (2010), Life cycle of a mesoscale circular gust front observed by a C-band Doppler radar in West Africa, submitted to Mon. Wea. Rev.

Machado, L., W. Rossow, R. Guedes, and A. Walker (1998), Life cycle variations of mesoscale convective systems over the Americas, *Monthly Weather Review*, *126*(6), 1630–1654.

Mahoney, W. (1988), Gust front characteristics and the kinematics associated with interacting thunderstorm outflows, *Monthly Weather Review*, *116*(7).

Mathon, V., and H. Laurent (2001), Life cycle of Sahelian mesoscale convective cloud systems, *Quarterly Journal of the Royal Meteorological Society*, *127*(572), 377–406.

McGill, M., M. Vaughan, C. Trepte, W. Hart, D. Hlavka, D. Winker, and R. Kuehn (2007), Airborne validation of spatial properties measured by the CALIPSO lidar, *J. Geophys. Res*, *112*.

Mekonnen, A., C. Thorncroft, and A. Aiyyer (2006), Analysis of convection and its association with African easterly waves, *Journal of Climate*, *19*(20), 5405–5421.

Miller, M., and A. Slingo (2007), The ARM Mobile Facility and Its First International Deployment Measuring Radiative Flux Divergence in West Africa, *Bulletin of the American Meteorological Society*, *88*(8), 1229–1244.

Mohr, K., and C. Thorncroft (2006), Intense convective systems in West Africa and their relationship to the African easterly jet, *Quarterly Journal of the Royal Meteorological Society*, *132*(614), 163–176.

Morales, C. (2010), personal communication.

Morales, C., and E. Anagnostou (2003), Extending the capabilities of high-frequency rainfall estimation from geostationary-based satellite infrared via a network of long-range lightning observations, *Journal of Hydrometeorology*, *4*(2).

Payne, S., and M. McGarry (1977), The relationship of satellite inferred convective activity to easterly waves over West Africa and the adjacent ocean during phase III of GATE, *Monthly Weather Review*, *105*(4).

Peters, M., and G. Tetzlaff (1988), The structure of West African squall lines and their environmental moisture budget, *Meteorology and Atmospheric Physics*, *39*(2), 74–84.

Price, C., Y. Yair, and M. Asfur (2007), East African lightning as a precursor of Atlantic hurricane activity, *Geophysical Research Letters*, *34*(9), 9805.

Price, C., M. Asfur, and Y. Yair (2009), Maximum hurricane intensity preceded by increase in lightning frequency, *Nature Geoscience*.

Redelsperger, J., C. Thorncroft, A. Diedhiou, T. Lebel, D. Parker, and J. Polcher (2006), African Monsoon Multidisciplinary Analysis: An international research project and field campaign, *Bulletin of the American Meteorological Society*, *87*(12), 1739–1746.

Reed, R., D. Norquist, and E. Recker (1977), The structure and properties of African wave disturbances as observed during Phase III of GATE, *Mon. Wea. Rev*, *105*(3), 317–323.

Reed, R., E. Klinker, and A. Hollingsworth (1988), The structure and characteristics of African easterly wave disturbances as determined from the ECMWF operational analysis/forecast system, *Meteorology and Atmospheric Physics*, *38*(1), 22–33.

Rickenbach, T., and S. Rutledge (1998), Convection in TOGA COARE: Horizontal scale, morphology, and rainfall production, *Journal of the Atmospheric Sciences*, *55*(17), 2715–2729.

Rickenbach, T., R. Nieto Ferreira, N. Guy, and E. Williams (2009), Radar-observed squall line propagation and the diurnal cycle of convection in Niamey, Niger during the 2006 African Monsoon and Multidisciplinary Analyses Intensive Observing Period, *J. Geophys. Res*, *114*, D03,107.

Rosenfeld, D. (1999), TRMM observed first direct evidence of smoke from forest fires inhibiting rainfall, *Geophysical Research Letters*, *26*(20), 3105–3108.

Rotunno, R., J. Klemp, and M. Weisman (1988), A theory for strong, long-lived squall lines, *Journal of the Atmospheric Sciences*, *45*(3), 463–4.

Rowell, D., and J. Milford (1993), On the generation of African squall lines, *Journal of Climate*, *6*(6), 1181–1193.

Russell, B., et al. (2010), Radar/rain-gauge comparisons on squall lines in Niamey, Niger for the AMMA, *Quarterly Journal of the Royal Meteorological Society*, *136*(S1), 289–303.

Rutledge, S., E. Williams, and T. Keenan (1992), The Down Upper Doppler and Electricity Experiment (DUNDEE): Overview and Preliminary Results., *Bulletin of the American Meteorological Society*, *73*(1).

Schmetz, J., P. Pili, S. Tjemkes, D. Just, J. Kerkmann, S. Rota, and A. Ratier (2002), An introduction to Meteosat second generation (MSG), *Bulletin of the American Meteorological Society*, *83*(7), 977–992.

Schrage, J., A. Fink, V. Ermert, and E. Ahlonsou (2006), Three MCS cases occurring in different synoptic environments in the sub-Sahelian wet zone during the 2002 West African monsoon, *Journal of the Atmospheric Sciences*, *63*(9), 2369–2382.

Shen, H., et al. (2006), Automated tracking of gene expression in individual cells and cell compartments, *Journal of the Royal Society Interface*, *3*(11), 787.

Simpson, J. (1969), A comparison between laboratory and atmospheric density currents, *Quart. J. Roy. Meteor. Soc*, *95*, 758–765.

Simpson, J. (1982), Gravity currents in the laboratory, atmosphere, and ocean, *Annual Review of Fluid Mechanics*, *14*(1), 213–234.

Simpson, J. (1987), *Gravity Currents in the Environment and the Laboratory, 244 pp*, Ellis Horwood Limited.

Slingo, A., et al. (2006), Observations of the impact of a major Saharan dust storm on the atmospheric radiation balance, *Geophys. Res. Lett*, *33*, L24,817.

Sultan, B., S. Janicot, and P. Drobinski (2007), Characterization of the diurnal cycle of the West African monsoon around the monsoon onset, *Journal of climate*, *20*(15), 4014–4032.

Sutton, L. (1925), Haboobs, *Q. J. R. Meteorol. Soc.*, *51*, 25–30.

Sutton, L. (1931), Haboobs, *Q. J. R. Meteorol. Soc.*, *57*, 143–161.

Thorncroft, C. (2010), personal communication.

Thorncroft, C., and K. Hodges (2001), African easterly wave variability and its relationship to Atlantic tropical cyclone activity, *Journal of Climate*, *14*(6), 1166–1179.

Thorncroft, C., N. Hall, and G. Kiladis (2008), Three-dimensional structure and dynamics of African easterly waves. Part III: Genesis, *J. Atmos. Sci*, *65*, 3596–3607.

Wakimoto, R. (1982), The life cycle of thunderstorm gust fronts as viewed with Doppler radar and rawinsonde data, *Monthly Weather Review*, *110*(8).

Wilkerson, W. (1991), Dust and sand forecasting in Iraq and adjoining countries, *Tech. Rep. AWS/TN–91/001*, Air Weather Service, Scott AFB.

Williams, E. (2008), Comment on "Atmospheric controls on the annual cycle of North African dust" by S. Engelstaedter and R. Washington, *J. Geophys. Res*, *113*.

Williams, E., and N. Renno (1993), An analysis of the conditional instability of the tropical atmosphere, *Mon. Wea. Rev.*, *121*, 21–21.

Williams, E., M. Weber, and R. Orville (1989), The Relationship Between Lightning Type and Convective State of Thunderclouds, *Journal of Geophysical Research*, *94*(D11), 13,213.

Williams, E., N. Nathou, E. Hicks, C. Pontikis, B. Russell, M. Miller, and M. Bartholomew (2009), The electrification of dust-lofting gust fronts ([] haboobs') in the Sahel, *Atmospheric Research*, *91*(2-4), 292–298.

Wilson, J., and W. Schreiber (1986), Initiation of convective storms at radar-observed boundary-layer convergence lines, *Mon. Wea. Rev.*, *114*, 2516–2536.

Winker, D., W. Hunt, M. McGill, et al. (2007), Initial performance assessment of CALIOP, *Geophys. Res. Lett*, *34*(L19803).

Wolf, R., and D. Just (1999), LRIT/HRIT global specification, *Coordination Group for Meteorological Satellites.*

Yuter, S., and R. Houze (2000), The 1997 Pan American Climate Studies Tropical Eastern Pacific Process Study. Part I: ITCZ region, *Bulletin of the American Meteorological Society*, *81*(3), 451–482.